UNIVERSITÉ DE SHERBROOKE
Faculté de génie
Département de génie mécanique

Modèles numériques détaillés pour la simulation de régénérateurs magnétiques actifs

Detailed numerical models for the simulation of Active Magnetic Regenerators.

Thèse de doctorat
Specialité: génie mécanique

Ibai MUGICA

Sherbrooke (Québec) Canada

Janvier 2019

JURY MEMBERS

Sébastien Poncet
Supervisor

Jonathan Bouchard
Co-supervisor

Mohamed Balli
Examiner

Kurt Engelbrecht
Examiner

Stéphane Moreau
Examiner

Hakim Nesreddine
Examiner

RÉSUMÉ

Les recherches sur les réfrigérateurs magnétiques ont jusqu'à présent été limitées par le coût élevé des prototypes, les difficultés liées aux mesures non intrusives et la résolution limitée des modèles numériques publiés. Cette thèse se concentre sur le développement de modèles numériques plus détaillés qui élucident le fonctionnement interne des régénérateurs magnétocaloriques actifs (AMR).

Cet objectif a au début été abordé en reproduisant un modèle numérique 1D, avec la résolution ajoutée du circuit magnétique impliqué. Le circuit magnétique a été jugé nécessaire pour obtenir une solution proche des données expérimentales. Ensuite, l'introduction de couches isolantes intermédiaires sur la longueur du régénérateur a été étudiée. Un nombre limité de couches isolantes a permis d'accroître les performances des régénérateurs étudiés en réduisant les pertes par conduction dans le domaine solide.

Ensuite, le développement du solveur numérique AMR 3D le plus détaillé à ce jour est présenté. Plus important encore, la validation de la résolution numérique directe 3D de tous les phénomènes a été effectuée. Le code a été développé sous la librairie OpenFOAM, ce qui rend le code source accessible, transparent et ouvert aux modifications de l'utilisateur. De plus, le poids du couplage physique des différents phénomènes a été analysé. La conclusion était que les champs thermique et fluide, et les champs thermique et magnétique ne sont pas fortement couplés et le solveur de cycle 3D AMR peut être simplifié en conséquence.

Enfin, le code simulant des cycles 3D AMR a été utilisé pour étudier des géométries de régénérateurs formés de bâtonnets. Chacun des phénomènes physiques a été étudié séparément (champs magnétique, hydrodynamique et thermique), puis le cycle AMR complet d'un groupe de géométries sélectionnées a été simulé. En outre, l'influence d'un paramètre géométrique, caractéristique de les milieux poreux, a été étudiée : la tortuosité. Globalement, l'augmentation de la tortuosité s'est révélée être une bonne stratégie pour augmenter les performances des réfrigérateurs magnétiques.

Mots-clés : Réfrigération magnétique, 3D, solveur, numérique, AMR, tortuosité

ABSTRACT

Research on magnetic refrigerators has so far been bounded by the high capital cost of prototypes, the difficulties of non-intrusive measurements, and the limited resolution of the published numerical models. The latters have shown the macroscopic behavior of such machines, as a function of characteristic geometrical parameters, like porosity. This thesis concentrates on the development of more detailed numerical models that elucidate the inner working mechanisms of Active Magnetocaloric Regenerators (AMRs).

Such objective was first approached by reproducing a 1D numerical model, with the added resolution of the magnetic circuit involved. The magnetic circuit was deemed necessary to get a solution that was closer to the experimental data. Then, the introduction of intermediate insulator layers along the length of the regenerator was investigated. A limited number of insulator layers proved to increase the performance of the regenerators by reducing the conduction losses in the solid domain.

Followingly, the development of the most detailed AMR numerical solver yet is presented. Most importantly, the validation of the 3D direct numerical resolution of all the solved phenomena is demonstrated. The code has been developed within the OpenFOAM framework, which makes the source code accessible, transparent and open to user's modifications. Moreover, the strength of the physical coupling of the intervening phenomena was analyzed. The conclusion was that the thermal and fluid, and thermal and magnetic fields are not strongly coupled and the 3D AMR cycle solver can be simplified to a certain extent.

Finally, the 3D AMR cycle solver was employed to investigate pin regenerator geometries. Each of the physical phenomena was studied separately (magnetic, fluid, and thermal fields) and then the full AMR cycle of a selected group of geometries was simulated. Also, the influence of a characteristic parameter of porous geometries was investigated: the tortuosity of the fluid surges. All in all, the increased tortuosity demonstrated to possibly be a better strategy to increase the performance of magnetic refrigerators.

Keywords: Magnetic refrigeration, 3D, solver, numerical, AMR, tortuosity

To Cady, my north star.

ACKNOWLEDGEMENTS

I would like to thank Prof. Sébastien Poncet for making sure my scientific productions are of the highest quality they can be. His knowledge on the scientific discourse has helped me to formalize my ideas into a structure that might be useful to other scientists.

I would also like to thank Dr. Jonathan Bouchard for sharing with me the deep insights he acquired on magnetic refrigeration. His way to conceptualize the design of magnetocaloric regenerators has been the bed rock of my research.

I would also like to thank all the jury members for having accepted to evaluate my work and for their valuable comments during my PhD thesis.

Lastly I would like to thank all the colleagues that pushed me to take a break once in a while. Even though annoying, for some reason I cannot comprehend, the mind needs to dive into a new environment to be creative again.

TABLE OF CONTENTS

LIST OF FIGURES

LIST OF TABLES

Nomenclature

A	Area	$[m^2]$
B	Magnetic field flux	$[T]$
c	Specific heat capacity	$[J \cdot m^{-3} \cdot K^{-1}]$
D	Demagnetization factor	$[-]$
D_h	Hydraulic diameter	$[m]$
F	Force	$[N]$
f	Frequency	$[Hz]$
$\mathfrak{F}$	Magnetomotive force	$[A]$
g	Gravity	$[m \cdot s^{-2}]$
Gd	Gadolinium	
h	Heat transfer coefficient	$[W \cdot m^{-2} \cdot K^{-1}]$
H	Magnetic field	$[A \cdot m^{-1}]$
$\dot{m}$	Mass flow	$[kg \cdot s^{-1}]$
M	Magnetization	$[A \cdot m^{-1}]$
$\mathbf{n}$	Normal vector	$[-]$
N	Demagnetization factor	$[-]$
Nu	Nusselt number	$[-]$
p	Pressure	$[Pa]$
Pr	Prandtl number	$[-]$
Q	Heat power	$[W]$
Re	Reynolds number	$[-]$
Ri	Richardson number	$[-]$
$\mathfrak{R}$	Reluctance	$[A^2 \cdot J^{-1}]$
S	Specific entropy	$[J \cdot m^{-3} K^{-1}]$
t	Time	$[s]$
T	Temperature	$[K]$
$\mathbf{u}$	Velocity field	$[m \cdot s^{-1}]$
V	Volume	$[m^3]$
W	Work power	$[W]$

Greek symbols

β	Thermal expansion	$[K^{-1}]$
ε	Porosity	$[-]$
φ	Utilization ratio	$[-]$
Φ	Magnetic flux	$[J \cdot A^{-1}]$
λ	Thermal conductivity	$[W \cdot m^{-1}K^{-1}]$
μ_f	Fluid viscosity	$[Pa \cdot s]$
μ_r	Relative magnetic permeability	$[-]$
ν	Kinematic viscosity	$[m^2 \cdot s^{-1}]$
ρ	Density	$[kg \cdot m^{-3}]$
τ	Tortuosity	$[-]$

Subscripts

0	Vacuum
ad	Adiabatic
app	Applied
B	Boundary
C	Curie
$cond$	Conduction
$cool$	Cooling
dip	Dipolar
eff	Effective
f	Fluid
H	Constant magnetic field
int	Internal
m	Mean value
mag	Magnetic
p	Particle
reg	Regenerator
rem	Remanent
r	Relative
rej	Rejected
s	Solid
T	Constant temperature

Acronyms

AMR	Active Magnetocaloric Regenerator
BC	Boundary Condition
BFS	Backward-Facing Step
CFC	Chloro Fluoro Carbons
CHT	Conjugate Heat Transfer
COP	Coefficient Of Performance
CPU	Central Processing Unit
DNS	Direct Numerical Simulation
FVM	Finite Volume Method
GSA	Grid Sensitivity Analysis
HE	Heat Exchanger
HCFC	Hydro Chloro Fluoro Carbons
HFC	Hydro Fluoro Carbons
HTF	Heat Transfer Fluid
MCE	Magneto Caloric Effect
MCM	Magneto Caloric Material
MFT	Mean Field Theory
MR	Magnetic Regenerator
NTU	Number of Transfer Units
PET	PolyEthylene Terephthalate
RAM	Random Access Memory
SIMPLE	Semi-Implicit Method for Pressure Linked Equations

CHAPTER 1

INTRODUCTION

Magnetic refrigeration is a relatively novel technology that has the potential to overcome some of the drawbacks of current vapor-compression cycles. Indeed, 17% of the worldwide electricity consumption is dedicated to refrigerator machines [20]. This means that a relatively small improvement of the refrigeration technologies has a big impact on the global energy consumption. The main potential advantages of magnetic refrigeration are:

1. The use of a solid refrigerant which avoids spilling pollutants to the environment, like the halocarbon fluids of vapor-compressor machines. These chlorine containing gases have been identified as the direct cause of the ozone depletion observed in earth's atmosphere. Furthermore, 20% of the global-warming produced by refrigerator machines is associated to the use of fluorocarbons [20].

2. The reduced noise during the operation of the refrigerator machine, due to the absence of compression and expansion stages.

3. The potential of an increased efficiency. This could come from the more isentropic phase change of the solid refrigerant, and the absence of inefficient processes like the compression and expansion stages of a vapor-compressor machines.

The first practical use of magnetic refrigeration was related to hydrogen liquefaction in the mid-70s (see [34]). Then, research extended to refrigerators that worked at room temperature. In the mid-90s the US department of Energy funded an AMR laboratory to extend the knowledge to industrial room temperature refrigeration. Some of the publications yielded by that project boosted the research on magnetocaloric room temperature refrigerators. Among those are the discovery of a "giant" Magneto Caloric Effect (MCE) by Gschneidner and Pecharsky [69], and a prototype that ran for 5000h over an 18 month period [109]. Since then, prototypes with increasingly higher cooling power and efficiency have been reported. Yu et al. [107] reviewed many of the prototypes developed in the last decade. In their review a clear tendency towards the use of permanent magnets and rotatory prototypes was shown.

Despite the recent developments, magnetic refrigeration still needs to face some challenges before becoming commercially viable:

1. Price of the raw materials to produce these refrigerators is still elevated. This is because of the relatively high amount of rare earths the prototypes have (i.e. kilograms of Gadolinium (Gd), Neodymium (Nd)).
2. The physical phase transition of the solid refrigerant needs of a relatively strong magnetic field (around 1-2T). This is usually costly to produce, so the magnetized airgap tends to be relatively small (in the 10s of mm).
3. During the regular operation of a mangetic regenerator, multiple physical phenomena coexist in a porous medium. Fluid flow, heat transfer, and magnetic field define the performance of the machine and are difficult to measure without being intrusive.

Some efforts have been made to lower the cost of raw materials by searching for more earth abundant Magneto Caloric Materials (MCMs, see [86]). Other scientists have work optimizing the design of the necessary permanent magnet [87]. Also, some articles have been published on the inner temperature measurement of Active Magnetic Regenerators (AMR) [19].

The central piece of magnetic refrigeration is the magnetic phase change of MCMs. Similar to the latent heat of a fluid, the solid refrigerant suddenly experiences an atomic structural change, which modifies the entropy balance of the MCM. The total entropy of a MCM is often expressed by Equation (1.1):

$$s_{total}(H,T) = s_{magnetic}(H,T) + s_{thermal}(T) \tag{1.1}$$

So, by (de)magntetizing externally the sample $s_{magnetic}$ is modified and the temperature of the sample changes (if the environment is adiabatic). Some simplified mathematical models have been developed to calculate the entropy change (see [84]). However, due to the introduced hypotheses not all MCMs follow the results predicted by the most popular model (Mean Field Theory). Generally, the specific entropy change of the available MCMs is relatively low. Thus, to attain a practical temperature span between the cold source and hot sink, several MCM cycles are linked one after the other. Because all cycles need to be magnetized, and the production of a high magnetic field is costly, the ensemble of cycles is compressed in a regenerator. In a more regeneral term, a regenerator is an intermediary device that connects thermodynamic cycles. In this specfic case the regenerator is made of MCM, a solid substance that exerts thermodynamic work into the cycle. Therefore, the device is called an Active Magnetic Regenerator (AMR). The volume of the regenerator is filled of two phases: a solid MCM that is stationary, and the Heat Transfer Flow (HTF). So in an steady state operation the HTF surges from the cold source to the hot sink linking

thermodynamically all the intermediate cycles. The cycles are usually conceptualized macroscopically in a continuous way along the full temperature span of the regenerator. So, the microscopic geometry of the regenerator defines how the applied magnetic field funnels into the MCM, how the heat is transferred by convection in and out the MCM, and what are the viscous losses of the fluid flow. The published prototypes to this date try to mimic a Brayton cycle for each of the differential points along the temperature span of the AMR:

1. Fast (quasi)adiabatic magnetization
2. HTF surge towards the hot sink
3. Fast (quasi)adiabatic demagnetization
4. HTF surge towards the cold source

By trying to approach a Brayton cycle the convective heat transfer can be as fast as possible, which increases the frequency at which the AMR can operate. This increases the cooling power, and makes up for the limited specific heat the MCM can pump. Considering the system described above, the main research question of the present doctoral thesis could be summarized by: *"What is the regenerator geometry that maximizes the performance of AMRs?"*

There are many ways to tackle that question, in this project, the main objective was to produce a reliable numerical code. If this solver is proven to give accurate physical results, many different numerical experiments could be performed. Numerical experiments can be a rich source of information due to the flexibility of their set up and the historically shrinking cost of computation.

The intermediate objectives made to address the research question are organized in the chapters of this document. First of all, a 1D thermal and magnetic numerical model was developed, following the state of the art of published numerical AMR cycle solvers. This kind of solvers employ experimentally determined correlations to model the average behavior of microscopic phenomena that happen within porous media (i.e. Nusselt number, demagnetization factor, friction correlations). Their accuracy and envelope of application is limited by the validity of the mentioned correlations. This limits the research results to the macroscopic behavior of the AMR. Nonetheless, in chapter 2 a validated 1D solver is employed to determine the benefits of introducing insulator stages along the length of a plate AMR. Secondly, to overcome the shortcomings of the 1D solver, a full 3D AMR cycle solver was developed and validated. This solver directly computes the fluid, magnetic and thermal fields of an AMR cycle. Additionally, the coupling mechanisms between the

mentioned physical phenomena were studied. Finally, the 3D AMR cycle solver is employed to study regenerators made of pins. The different properties of such regenerators are carefully simulated, along with a characteristic parameter of porous geometries: the tortuosity of the fluid flow.

CHAPTER 2

Entropy generation in a parallel-plate active magnetic regenerator with insulator layers

2.1 Avant-propos

Auteurs et affiliations:

1. Ibai Mugica: étudiant au doctorat*
2. Sébastien Poncet: professeur*
3. Jonathan Bouchard: chercheur**

*Université de Sherbrooke, Faculté de génie, Département de génie mécanique.
**Laboratoire des Technologies de l'Énergie, Hydro-Québec, Shawinigan.

Date d'acceptation: 24 Janvier 2017

État de l'acceptation: version finale publiée

Revue: Journal of Applied Physics

Titre français: Génération d'entropie dans un régénérateur magnétique actif à plaques parallèles avec des couches isolantes

Contribution au document: Cet article contribue à la thèse en introduisant la validation d'un solveur AMR 1D avec un modèle de champ magnétique détaillé et en explorant l'influence de couches isolantes.

Résumé français: Cet article propose une solution réalisable pour réduire les pertes de conduction dans les régénérateurs magnétiques actifs. Les performances plus élevées de ces machines sont liées à une conductivité thermique inférieure à celle du matériau magnéto-calorique (MCM) dans le sens du courant. Le concept présenté ici implique l'insertion de couches isolantes sur la longueur d'un régénérateur magnétique à plaques parallèles afin de réduire la conduction thermique dans le MCM. Cette idée est étudiée à l'aide d'un modèle numérique 1D. Ce modèle résout non seulement les équations d'énergie pour les domaines fluide et solide, mais également le circuit magnétique conforme au montage expérimental de référence. En conclusion, l'ajout de couches isolantes dans le MCM augmente la plage de température, la charge de refroidissement et le coefficient de performance en combinant des pertes de

conduction thermique plus faibles et une augmentation de l'effet magnéto-calorique global. L'entropie générée par conduction solide, convection dans le fluide, conduction et pertes visqueuses est calculée pour aider à comprendre les implications de l'introduction de couches isolantes dans les régénérateurs magnétiques. Enfin, le nombre optimal de couches isolantes est étudié.

2.2 Entropy generation in a parallel-plate active magnetic regenerator with insulator layers

The following paper proposes a feasible solution to diminish conduction losses in Active Magnetic Regenerators. Higher performances of these machines are linked to a lower thermal conductivity of the Magneto-Caloric Material (MCM) in the streamwise direction. The concept presented here involves the insertion of insulator layers along the length of a parallel-plate magnetic regenerator in order to reduce the heat conduction within the MCM. This idea is investigated by means of a 1D numerical model. This model solves not only the energy equations for the fluid and solid domains, but also the magnetic circuit that conforms the experimental set-up of reference. In conclusion, the addition of insulator layers within the MCM increases the temperature span, cooling load and COP by a combination of lower heat conduction losses and an increment of the global Magneto-Caloric Effect (MCE). The generated entropy by solid conduction, fluid convection and conduction, and viscous losses are calculated to help understand the implications of introducing insulator layers in magnetic regenerators. Finally the optimal number of insulator layers is studied.

2.2.1 Introduction

Since the discovery of the so called “Giant" Magneto-Caloric Effect, the interest in magnetic refrigeration has increased exponentially and it has been appointed as a possible substitute of vapor-compression cycles ([33]). Magnetic refrigeration uses a solid refrigerant, which means that no CFC or HFC gases can be released by the use of this technology. The principle of such promising technology is founded on the Magneto-Caloric Effect (MCE), discovered by Weiss and Piccard [105]. The MCE is a physical phenomenon for which Magneto-Caloric Materials (MCM) change their temperature when they are subjected to a varying magnetic field. The MCE is highest around the Curie temperature (T_C). At this temperature, the MCM undergoes a magnetic phase transition. Below T_C, the material is in a ferromagnetic state and the magnetic momentums of the atoms are

aligned to some extent (Figure 2.1).

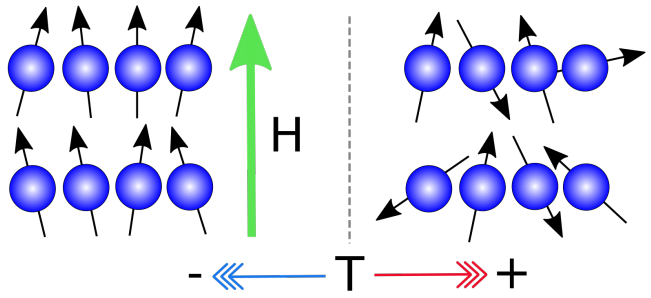

Figure 2.1 Atomic magnetic moments under the influence of an applied magnetic field, or a change in temperature.

Because of this alignment, the material has a net magnetic field that is called Magnetization (M). If the temperature is increased past the T_C, the material is brought to a higher energy state, and it becomes paramagnetic. In the paramagnetic sate, the magnetic momentums of atoms show a more random direction, and thus magnetization disappears. For an MCM in the paramagnetic state, if the magnetic alignment (ferromagnetic state) is induced by an applied magnetic field, the substance is brought back to a lower level of magnetic entropy, meaning that if the environment is adiabatic, the excess entropy takes the form of a temperature increase (thermal entropy). Thereby, one could think of the thermodynamic state variables of an MCM as H, M and T, as opposed to P, V and T for a fluid refrigerant. The reader can refer to [39] for more details on the thermodynamics of MCMs.

The most popular refrigeration cycle using MCE is the Active Magnetic Regeneration (AMR). In the AMR cycle, magnetization and demagnetization processes are induced between oscillating fluid surges (Figure 2.2). The oscillating flow transports the heat created during magnetization to a hot sink (Cold surge), and it takes heat from the cold source to warm up the regenerator again, after a demagnetization step (Hot surge). During its operation, the magnetic regenerator develops a temperature gradient that starts at the cold source and finishes at the hot sink. This temperature gradient has its origin in the oscillating flow. Similar to a heat exchanger, the Heat Transfer Fluid (HTF) loses or gains temperature as it travels through the regenerator, leaving the MCM with a similar temperature distribution. Therefore, each point of the regenerator undergoes its own thermodynamic cycle, slightly offset to its own neighbor points (see Figure 2.2).

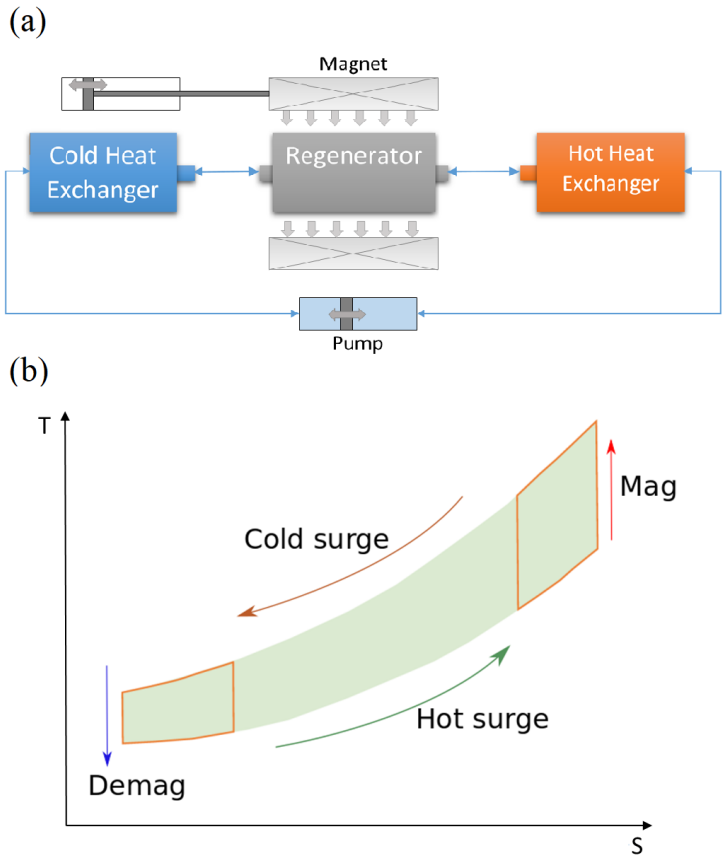

Figure 2.2 (a) Generic set up of an AMR cycle. (b) T-S cycle diagram of a generic AMR cycle. The highlighted cycles represent the end points of the regenerator, and the shaded area would be the collection of all the T-S diagrams.

The work of this thermodynamic cycle is employed to transport heat from the cold side to the hot side of the regenerator. At the same time, the heat conduction within the MCM acts to re-establish the thermodynamic equilibrium. This loss mechanism was already pointed out by Bahnke and Howard [7] for passive regenerators. Das and Sahoo [24] concluded that the optimal operational point of a passive regenerator highly depends on considering heat conduction in the solid domain or not. These authors established a trend on optimizing the regenerator variables by looking at the total generated entropy (S_{gen}). Before, attention was centred in designing a passive regenerator that had the highest heat storage capacity. But what is truly of interest is the maximum exergy a regenerator can store, as this expresses the potential work that can be extracted from a certain quantity of heat energy. Then, posterior publications used this methodology to optimize active magneto-caloric regenerators. [46] and [45] published a detailed mapping of the Coefficient of Performance (COP) and S_{gen} of an AMR as a function of frequency and mass flow rate for several geometric parameters. While [46] concentrated on packed bed regenerators, [45] investigated 5 different geometries: packed bed, parallel plates, square and cylindrical micro-channels, and screens. Parallel plate and microchannel geometries show better overall efficiencies because the passage of the flow is not hindered. The ability to manufacture these geometries is limited by the brittleness of the MCMs and the tight tolerances required. As [59] showed, flow maldistribution caused by deviations from the original geometry, substantially damages the overall heat transfer of plate regenerators.

[58] further investigated the effects of solid heat conduction losses on the maximum cooling power of a plate regenerator. In order to do that, they numerically solved the heat transfer and fluid momentum equations in a 2D computational domain. They proposed that the ideal MCM should be highly anisotropic, having a high thermal conductivity towards the HTF, but a low one in the direction of the flow. Earlier, [57] divided a passive wire regenerator to introduce contact thermal resistance between the segments and reduce heat conduction. A regenerator with 7 segments showed a lower effective axial conduction, and higher friction losses. Then, an effective thermal conductivity extracted from the experiments was introduced in a 1D numerical model to calculate the generated entropy. This way, the optimum values of mass flow, frequency, aspect ratio, and phase between (de)magnetization and fluid surges of the geometry could be found. From [45] and [57], it can be concluded that the ideal regenerator geometry would have a large heat transfer surface (like porous beds), without hindering the passage of the HTF (like parallel plates or wire regenerators). The downside of the later would be the higher heat conduction losses compared to porous beds or screens. If segmentation (like in [57]) is taken further,

the geometry of the regenerator would start to look more and more like a porous bed. At the same time, for every segmentation, flow resistance is introduced, as the segments can hardly be kept aligned. Joining regenerator segments by insulator layers provides structural integrity to the regenerator geometry, by making sure the flow passage is not hindered by the next MCM segment. Moreover, if the insertion of insulators is proven to be beneficial, segmentation could be taken far by gluing together relatively small sections of MCM. This configuration could be regarded as the highly anisotropic material that was proposed by [58].

This paper numerically models the insertion of such insulator layers in a plate AMR. In fact, the effects of segmentation and the possible detrimental effects of the insulator layers in the AMR cycle are yet uncertain. Thus, the following hypotheses are going to be studied in the subsequent sections: I. Inserting insulator layers in the AMR regenerator helps to reduce the conduction losses in the MCM during steady state operation. Therefore, the maximum temperature span, cooling power and COP will increase. II. As a result of reducing the conduction heat transfer in the MCM, the total generation of entropy will decrease.

2.2.2 Numerical model

Thermal model

Like all the AMR mathematical models present in the literature, the behaviour of the magnetic plate regenerator will be described by the energy conservation principle in the fluid and solid domains (see [41]).

$$\rho_s \frac{\partial (c_s T_s)}{\partial t} = \lambda_s \frac{\partial^2 T_s}{\partial x^2} + \dot{Q}_{transfer} + \dot{Q}_{MCE} \tag{2.1}$$

$$\rho_f c_f \left(\frac{\partial T_f}{\partial t} + u \frac{\partial T_f}{\partial x} \right) = \lambda_f \frac{\partial^2 T_f}{\partial x^2} + \dot{Q}_{transfer} \tag{2.2}$$

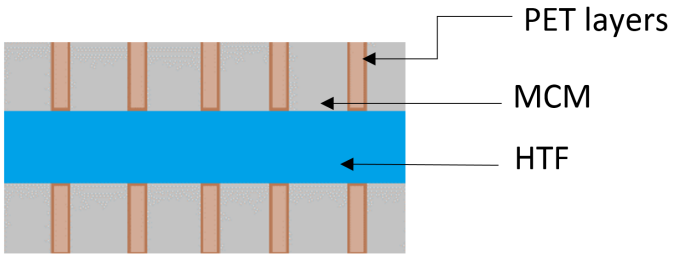

Figure 2.3 Disposition of the insulator layers within the regenerator

Fluid properties of ρ_f,c_f and λ_f were extracted from the CoolProp library (see 2.1) and kept constant during the simulation. These equations (2.1) and (2.2) will be solved at all times: during (de)magnetization, cold and hot surges, and at idle time frames. Each of these domains will have its appropriate energy source ($\dot{Q}_{transfer}$ or/and $\dot{Q}_{MCE}$) during the different processes. Thereby, (de)magnetization processes will use the following expression to include the MCE:

$$\dot{Q}_{MCE} = -\mu_0 T \left.\frac{\partial M(H,T)}{\partial T}\right|_H \frac{\partial H}{\partial t} \tag{2.3}$$

The derivation of equation (2.3) is thoroughly explained in [41]. In order to calculate $\dot{Q}_{MCE}$ at each time step, information about the magnetization of the material $\left.\frac{\partial M(H,T)}{\partial T}\right|_H$ is necessary. Most of the models published so far, use the Mean Field Theory (MFT) of ferromagnets to characterize the behaviour of the MCM (see [54]). The MCM used in this investigation is Gadolinium and unfortunately, as it is shown in Figure 2.4, MFT does not predict entirely well its adiabatic temperature change ($\Delta T_{ad} = -\frac{T}{c_s(H,T)} \left.\frac{\partial M(H,T)}{\partial T}\right|_H \frac{\partial H}{\partial t}$). In order to overcome this difficulty, magnetization data was fitted using the function proposed by [15]:

$$M(H,T) = M_{sat}(T)\left[\frac{a(T)}{H^{1/2}} + \frac{b(T)}{H} + \frac{c(T)}{H^{3/2}} + \frac{d(T)}{H^2}\right] + e(T)H \tag{2.4}$$

As commented by [54] this function seems to fit well the experimental magnetization data of many substances, but the origins of each term in equation (2.4) are not clear. The fitting was done using the data from [44] (see Appendix B for the full expression of the fitted function). The ratio between the variance of the experimental data and the fitted function was $R^2 = 0.9981$. In Figure 2.4, the adiabatic temperature change of the MFT, the fitted function, and experimental magnetization data from [23] are compared.

The MFT misses most of the data points from [23], whereas the fitted function is within the uncertainty limits for most of them. The great thing about having the magnetization $H - T$ surface is that it can always be used to calculate the MCE for other cases with different specimen shapes and other parasitic reluctances (see next section 2.2.2). Data for $c_s(H,T)$ (necessary to solve equation (2.1)) was interpolated from [76]. The other heat source $\dot{Q}_{transfer}$, represents the heat transfer between the solid and fluid domains. $\dot{Q}_{transfer}$ takes two different values: either the HTF is at rest or a surge is happening. When the fluid is at rest, the heat transfer happens by conduction and the fluid alone is taken to be representative of this heat transfer due to a much lower thermal diffusivity (see Table B.1 in section B). In this case $\dot{Q}_{transfer}$ has the form of:

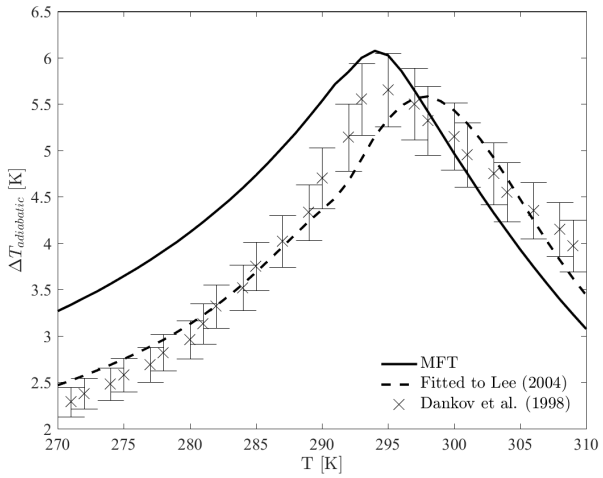

Figure 2.4 Comparison of ΔT_{ad} under $H_{app} = 2T$ provided by MFT, the fitted equation (2.4), and data from [23].

$$\dot{Q}_{transfer} = \frac{\lambda_f A_{HT}(T_s - T_f)}{Ve_f/2} \tag{2.5}$$

When fluid surges are induced, the heat transfer will be modeled according to the plate regenerator presented in section 2.2.2. In order to do so, convection heat transfer correlations are employed. The heat transfer coefficient (h) is calculated using the Nusselt number for constant laminar flow in rectangular ducts ([78]):

$$Nu = 8.235(1 - 2.0421r + 3.0853r^2 - 2.4765r^3 + 1.0578r^4 - 0.1861r^5) \tag{2.6}$$

$$h = \frac{\lambda_f Nu}{D_h} \tag{2.7}$$

$$\dot{Q}_{transfer} = \frac{hA_{HT}(T_s - T_f)}{V} \tag{2.8}$$

The boundary conditions are the usual ones for 1D AMR mathematical models: adiabatic boundary conditions, and, in the cold side inlet, perfect mixing temperature from the last surge:

$$T_{inlet} = \int_t^{t+t_{surge}} T_f(x = 0, t)dt \tag{2.9}$$

As explained in section 2.2.2, the hot side inlet will be maintained at a constant temperature. Between MCM and insulator layers, the continuity of heat conduction through the interface is imposed:

$$\dot{Q}^{MCM}_{inteface} = \dot{Q}^{PET}_{inteface} \tag{2.10}$$

Assuming a linear temperature profile between the last node and the interface, the interface temperatures are easily obtained, and thus the boundary conditions of each segment of MCM and PET as well.

Magnetic model

In order to calculate accurately the MCE it is important to know what is the magnetic field that the MCM experiences. This is going to be referred as the effective magnetic field (H_{eff}). There are two aspects to be taken into account: the demagnetization field and the parasitic reluctances. The demagnetization field is caused by the magnetic poles that appear on the surface of a magnetized material. A thorough explanation of this phenomenon can be found in [54]. The result is a demagnetizing field opposite to the applied magnetic field. The demagnetizing field is proportional to M for ellipsoids, and for other cases an equivalent demagnetizing factor D is usually employed:

$$H_{eff} = H_{app} - DM \tag{2.11}$$

For rectangular prisms, [1] offers theoretically derived averaged values of D. The magnetic flux (Φ) that goes from one pole of the magnet to the other one, crosses materials that are not the MCM like the air, the casing of the regenerator, and the HTF. They constitute the parasitic reluctances of the system, and they lower the effective magnetic field H_{eff}. The calculus of the reluctances is done by equation (2.12), where $\mathfrak{R}$ is the reluctance value, μ the magnetic permeability, $\mathfrak{F}$ the magnetomotive force, L L is the length of the reluctance in the direction of the magnetic field, and A_{cross} the cross section of the reluctance in the direction of H_{app}. The resolution of the effective magnetic field can be set up as an analogy to the electric circuit, like [103] did (see Figure 2.5).

$$\mathfrak{R} = \frac{\mathfrak{F}}{\Phi} = \frac{\int Hdl}{\int Bds} = \frac{L}{\mu_0 \mu_r A_{cross}} \tag{2.12}$$

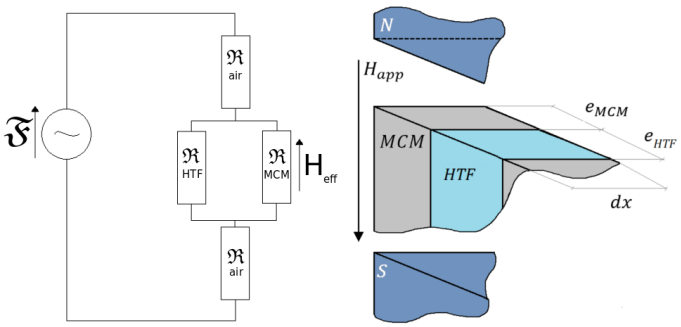

Figure 2.5 Sketch of the magnetic circuit.

The reluctance of the MCM depends on its magnetization, thus $\mathfrak{R}_{MCM}$ depends on the final effective field.

$$\mu_r(H_{eff}, T) = 1 + (1 - D)\frac{M(H_{eff}, T)}{H_{eff}} \tag{2.13}$$

$$H_{eff} = \frac{H_{app} L_{air}}{\mathfrak{R}_{Total}(H_{eff}, T) L_{palte}} \cdot \frac{\mathfrak{R}_{MCM}(H_{eff}, T)\mathfrak{R}_{HTF}}{\mathfrak{R}_{MCM}(H_{eff}, T) + \mathfrak{R}_{HTF}} \tag{2.14}$$

Then, the nonlinear equation (2.14) is solved at every time step, in order to get the effective magnetic field of the MCM.

Numerical methods

The energy equations (2.1) and (2.2) are discretized by finite differences, using the Crank Nicholson second order implicit scheme. This gives rise to a Tridiagonal matrix that is solved by the Thomas algorithm. The resolution of the PDEs was verified by the Method of Manufactured Solutions. The non linear magnetic circuit is solved by the Newton-Raphson method.

Baseline case

The numerical simulations are based on the regenerator "A" published by [97] (see Table 2.1). In their experiment, the plates of regenerator “A" are parallel to the applied magnetic field, yielding a very low demagnetization effect (D=0.0403 according to [1]). The cold source is adiabatically insulated in order to control the cooling load, and the Hot sink is maintained at a constant temperature of 300K. The specified idle time (0.9s) is shared in the code between the regular processes of an AMR. Thus, at a given frequency (f), the cycle develops as follows: 1.Magnetization, 2.Idle time, 3.Cold blow, 4.Idle time 5.Demagnetization 6.Idle time 7. Hot blow 8.Idle time. The casing of the regenerator is made of a ertalyte plastic, so it is taken to have a similar magnetic permeability as air and the HTF ($\mu_r \approx 1$). When adding the insulator layers to the baseline case, the amount of MCM mass will be kept constant and the total length of the regenerator will be increased by the length of the insulators. The insulator layers will be evenly distributed in the regenerator, to make MCM segments of the same length.

2.2.3 Grid sensitivity and validation

As for all numerical investigations, the independence of the solution to the grid size has to be carefully checked. This is done here for the first cycle of the AMR in Figure 2.6.

Different discretizations show the numerical solution to be in the asymptotic region

Plate thickness	$0.25\,mm$
Channel thickness	$0.1\,mm$
Porosity	0.2564
Length	$80\,mm$
Cross-Section	$10 \times 39\,mm^2$
Mass of Gd	$0.1763\,kg$
H_{app}	$1.15\,T$

Table 2.1 Properties of regenerator "A", after [97].

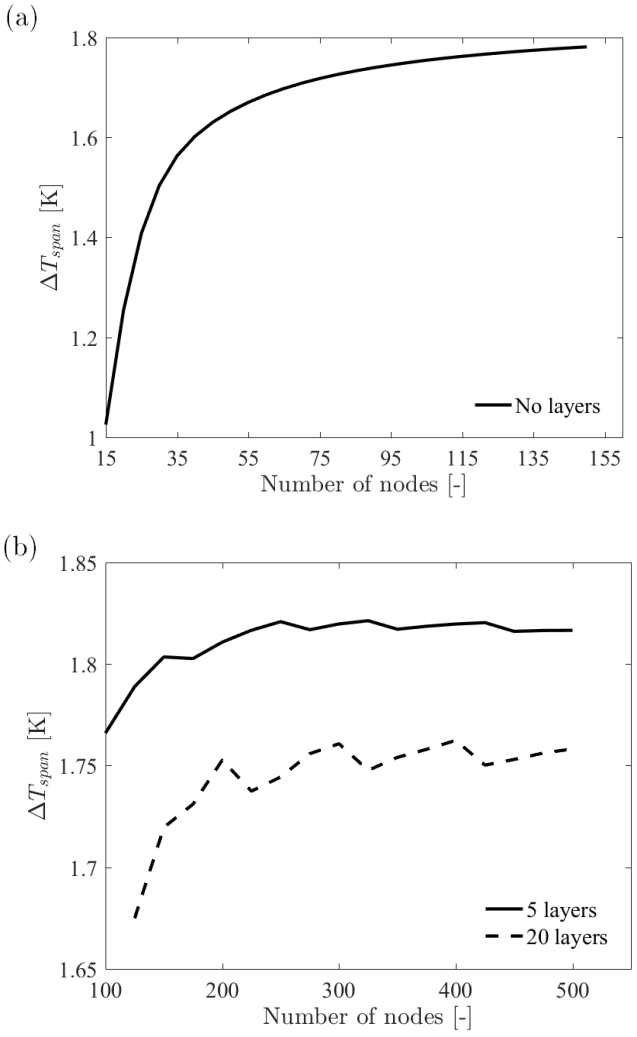

Figure 2.6 Temperature span in the regenerator as a function of the number of spatial nodes after the first cycle (working at $f = 0.3\,Hz$ and $\varphi = 0.3$). (a) regenerator with no insulator layers, (b) regenerator with 5 and 20 layers.

around 125 nodes for the regenerator without layers, and 500 nodes for the regenerators with 5 and 20 layers. In Figure 2.7, the temperature span of regenerator "A" ([97]) is plotted against the utilization rate. The utilization rate expresses the ratio between the thermal energy that the HTF and the MCM are able to exchange, and is regulated by the flow rate ($\dot{m}_{HTF}$) of the surges:

$$\varphi = \frac{\dot{m}_{HTF} c_{HTF} t_{surge}}{m_{MCM} \bar{c}_{MCM}} \tag{2.15}$$

The predicted temperature span of the present numerical model (VI in Figure 2.7) is close to the experimental values of [97] (VII). [27] also used the experimental set-up of [97] to evaluate the results of their numerical model. In addition to demagnetization losses, they studied the effect of heat losses and flow maldistribution. In Figure 2.7, the results of the numerical model of [27] are also compared, and the differences of applying or not the loss mechanisms is presented.

The numerical models without any losses (I and IV) have a similar shape but differ substantially in the ΔT_{span} values. This is thought to be caused by different Nu values used to model heat convection. Obtaining a reliable value of Nu is indeed crucial to simulate correctly the operation of an AMR. For that purpose, 2D or 3D simulations of the real regenerator geometry would be more appropriate, as the convective heat transfer could be solved along the geometry of the regenerator rather than modelled. [27] concluded that different loss mechanisms can substantially modify the regenerator response, and that they should be considered when modeling an AMR. From a numerical perspective, it is hard to assess the real weight of each of these contributions. Measuring these losses experimentally could shed some light into which are the most important loss mechanisms to take into consideration. In this study, including demagnetization losses and the parasitic reluctances seems to fit the behaviour of the present AMR for the Nu employed.

2.2.4 Results

Figure 2.8 shows how the number of insulator layers increases the maximum temperature span at lower utilization ratios. At higher utilization rates though, the temperature span for any number of 1 mm layers approaches the case with no layers. Indeed, as the utilization rate is incremented by increasing $\dot{m}_{HTF}$, heat transfer by convection takes over. As a consequence, conduction is reduced and the insulator spacers are no longer useful. Figure 2.8 supports the first hypothesis, and it confirms how the continuous heat exchange that normally undergo all the points of the regenerator is detrimental to the system. In Figure

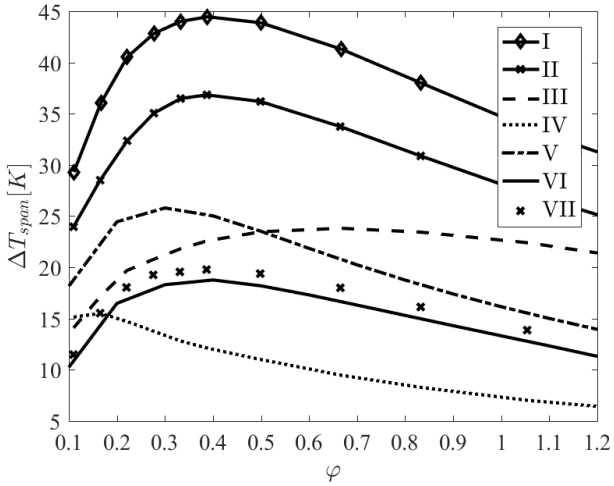

Figure 2.7 Zero cooling load temperature span for an operation frequency of $f = 0.3Hz$. I. Model from [27] without losses, II. Model from [27] with demagnetization losses, III. Model from [27] with demagnetization and heat losses, IV. Model from [27] with maldistribution losses, V. Present numerical model with no losses, VI. Present numerical model with demagnetization and parasitic reluctance losses, VII. Regenerator "A" published by [97]

2.9, the maximum temperature span is still visibly incremented by the additional insulator layer length at higher utilization rates. This is thought to come from the role of the insulator layers as passive regenerators. The evolution of the maximum temperature span is more clearly expressed in Figure 2.10.

The influence of the insulator layers in the cooling load (Q_{cool}) and COP was also checked in Figures 2.11 and 2.12. The COP was calculated as:

$$COP = \frac{Q_{cool}}{Q_{rej} - Q_{cool} + W_{visc}} \tag{2.16}$$

Both Q_{cool} and COP present an improvement as the number of layers is increased. The improvement seems to be slightly higher in the case of $\varphi = 0.2$, which makes sense, as heat conduction has a higher influence on the solution.

To understand the impact of insulator layers in the efficiency of the AMR, the evolution of the generated entropy is investigated for the case of $1\,mm$ spacers. Using the same strategy as [88], the total generated entropy of equation (2.17) will be integrated in time for a steady state cycle.

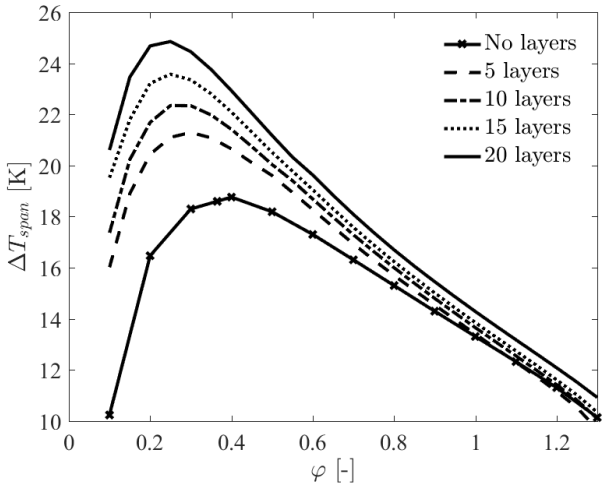

Figure 2.8 Influence of the utilization ratio (φ) on the maximum temperature span (zero cooling load) for different number of evenly distributed $1\,mm$ layers at a frequency of $f = 0.3\,Hz$.

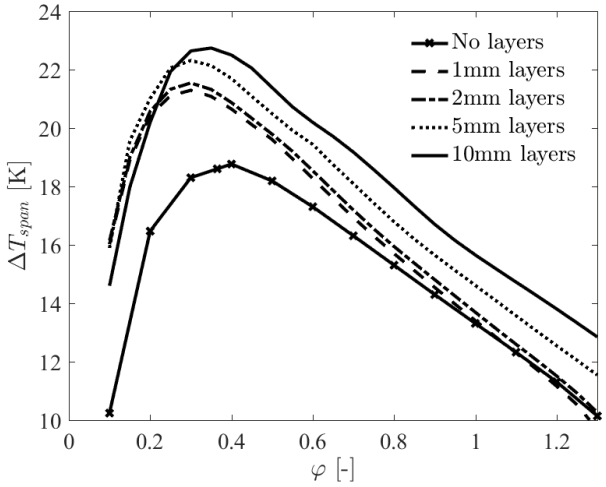

Figure 2.9 Influence of the utilization ratio (φ) on the maximum temperature span for 5 layers with different thickness working at $0.3\,Hz$.

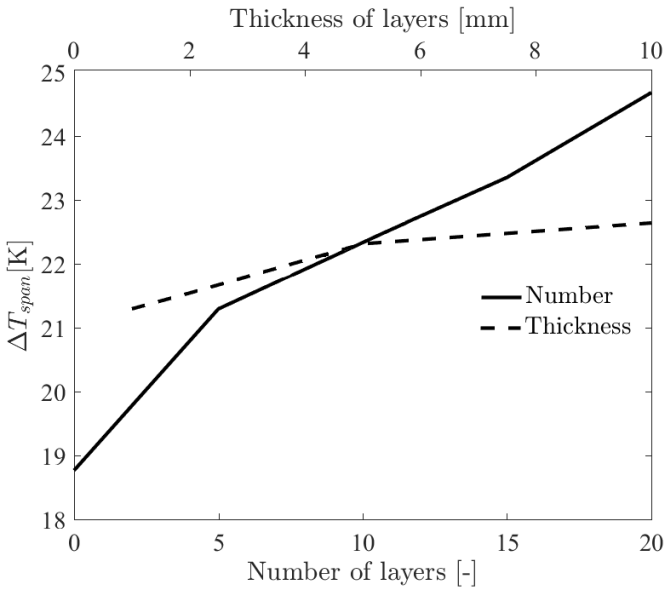

Figure 2.10 Evolution of the maximum temperature span (zero cooling load) varying the number and thickness of the insulator layers at a frequency of $f = 0.3\,Hz$.

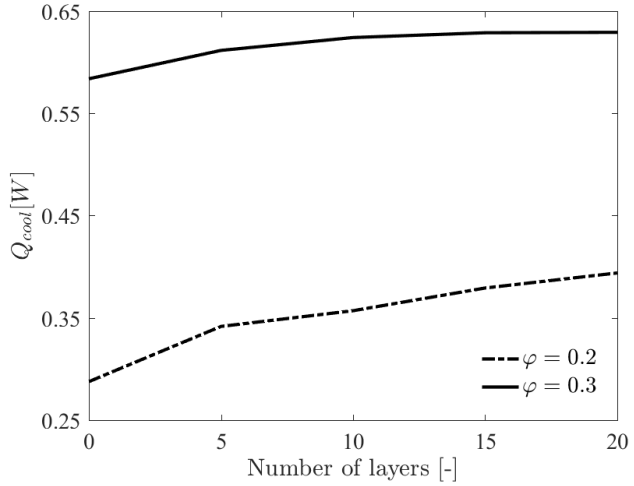

Figure 2.11 Influence of the number of $1\,mm$ insulator layers on the cooling power at $f = 0.3\,Hz$ and $\Delta T_{span} = 15\,K$.

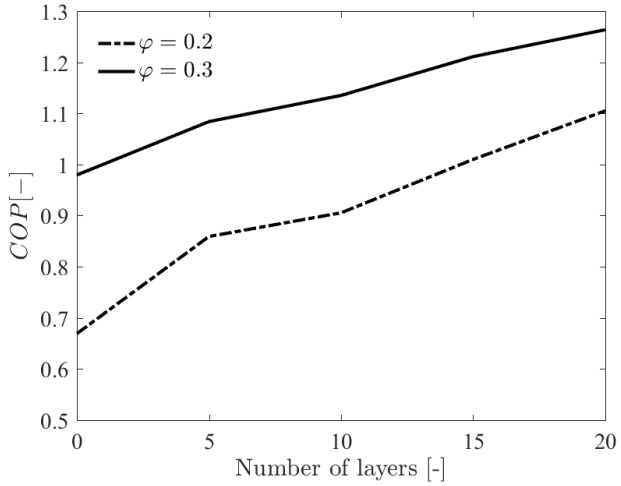

Figure 2.12 Influence of the number of $1\,mm$ insulator layers on the COP at $f = 0.3\,Hz$ and $\Delta T_{span} = 15\,K$.

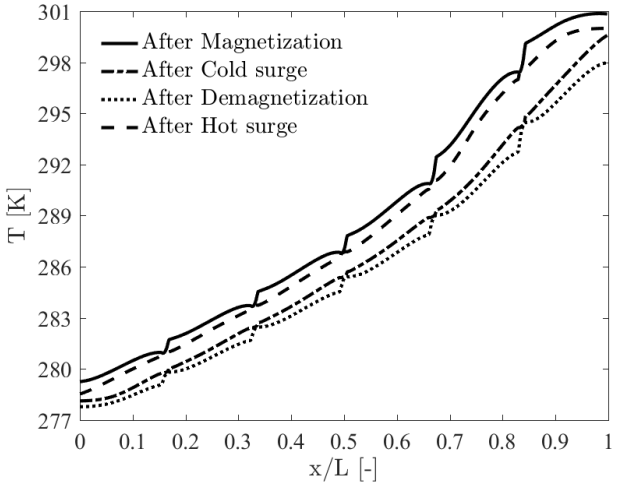

Figure 2.13 Steady state temperature distribution of the tested regenerator with 5 layers of 1mm at $f = 0.3\,Hz$ and $\varphi = 0.3$.

$$\dot{S}_{gen} = \dot{S}_{Scond} + \dot{S}_{Fcond} + \dot{S}_{conv} + \dot{S}_{visc} = \\ = \frac{\lambda_s}{T_s^2}\left(\frac{\partial T_s}{\partial x}\right)^2 + \frac{\lambda_f}{T_f^2}\left(\frac{\partial T_f}{\partial x}\right)^2 + \frac{hA_{HT}(T_s - T_f)^2}{T_s T_f V} + \frac{1}{T_f}\left|u\frac{\partial P}{\partial x}\right| \tag{2.17}$$

Each of the contributions in equation (2.17) will be analyzed separately. First of all, Figure 2.14 shows an appreciable reduction of the generated entropy by conduction within the solid (S_{Scond}) in the vicinities of the insulators. As Figure 2.13 shows, the insulator layers concentrate in them portions of the temperature jump between the cold and hot sides of the regenerator. And even though the total temperature span increases when insulators are introduced, the integral value of S_{Scond} decreases (see Figure 2.18). Large temperature gradients in the PET layers do not contribute considerably to S_{Scond} because they have a much lower thermal conductivity compared to the MCM ($\lambda_{PET} << \lambda_{MCM}$ see Table B.1 in section B).

Because of a higher ∇T in the insulator spacers, the generated entropy by conduction within the fluid domain (S_{Fcond}) increases when adding more spacers (Figure 2.18). This means that some of the conduction heat bypasses the insulator layers and goes through the HTF, causing the peaks of S_{Fcond} in Figure 2.15.

A first look on Figure 2.16 shows some high peaks of the generated entropy by convection (S_{conv}) at the limits of the insulator layers. S_{conv} increases with the square of the temperature difference between the fluid and solid domains. So for each flow surge, the HTF encounters in its path the abrupt temperature jumps of the solid domain (see Figure 2.13) and thus, S_{conv} increases considerably there. The high peaks of Figure 2.16 do not contribute significantly to the generated entropy. This is because they are very localized and the lack of MCE in the insulators reduces S_{conv} in the spacers, balancing out the high peaks. The increase of S_{conv} with the number of insulator spacers (see Figure 2.18) comes from the reduction of the temperature gradient in the MCM segments. As a side effect, a segment of MCM working with a lower temperature gradient has more points working near T_C. Therefore, S_{conv} augments because the global MCE increases, producing higher temperature changes at some points of the regenerator that were farther from T_C. So, a higher temperature difference in the (de)magnetization processes contributes to increase S_{conv}. This is revealed in Figure 2.16 where the relative maximum of S_{conv} between $x/L = [0.7, 0.8]$ is working near T_C in Figure 2.13 ($T_C = 293K$ for Gd). Finally, the generated entropy by viscous dissipation (S_{visc}) does not experience a large change

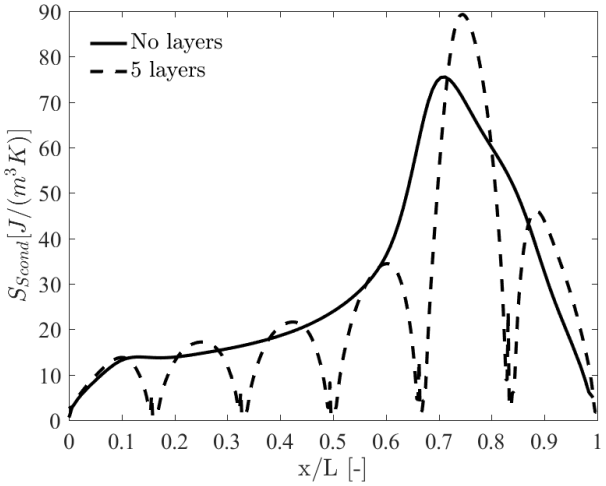

Figure 2.14 Longitudinal distribution of the generated entropy by conduction in the solid domain, for a steady state cycle working at $f = 0.3\,Hz$ and $\varphi = 0.3$.

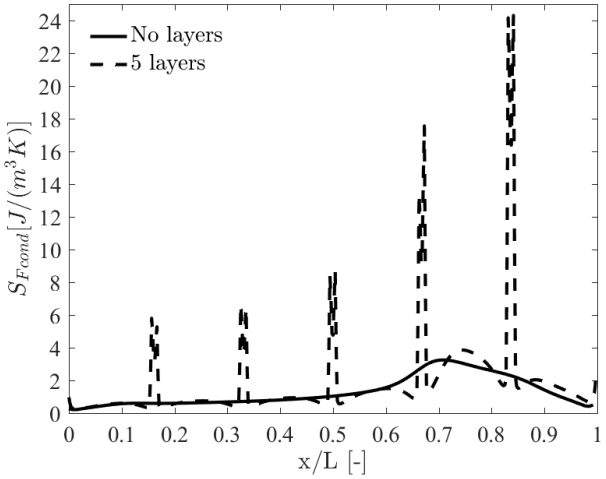

Figure 2.15 Longitudinal distribution of the generated entropy by conduction in the fluid domain, for a steady state cycle working at $f = 0.3\,Hz$ and $\varphi = 0.3$.

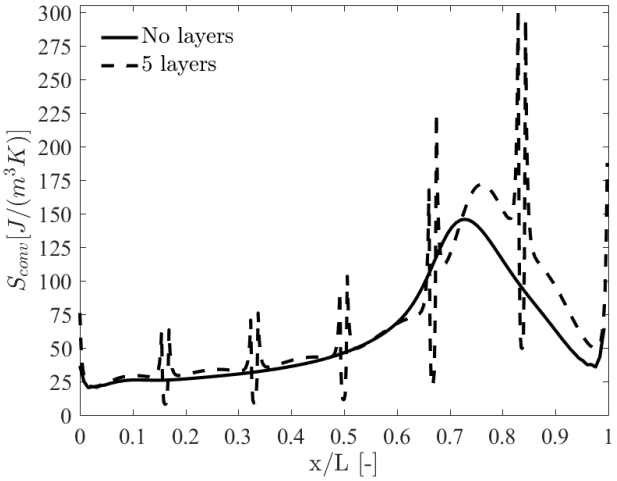

Figure 2.16 Longitudinal distribution of the generated entropy by convection, for a steady state cycle working at $f = 0.3Hz$ and $\varphi = 0.3$.

when adding the insulator layers. In fact, the hot sink is always maintained at 300K, so when the total temperature span augments, the regenerator works at lower temperatures, and as a consequence S_{visc} slightly increases.

Figure 2.18 shows the evolution of the total generated entropy. S_{Scond} and S_{conv} are the contributions that most affect S_{gen}. And even though the second hypothesis proves false, the insertion of insulator layers is considered to positively affect the system. This is because the increment of S_{conv} comes from an increment of the MCE, which is the mechanism that enables to turn magnetocaloric work into cooling power. Thereby the temperature increase seen in Figure 2.8 is due to the combination of a reduction of the solid conduction and an increase of the magnetocaloric work.

From the designer perspective, the number of layers in the regenerator could be optimized. Further simulations showed that increasing the length of the insulator layers did not reduce heat conduction substantially. For a regenerator with $1\,mm$, $0.5\,mm$ and $0.2\,mm$ thick layers S_{Scond} was 0.8132, 0.8608,and 0.8820 $\frac{J}{m^2K}$ respectively, as opposed to $2.3509\frac{J}{m^2K}$ for the case with no layers. Hence, the additional thickness would mainly increase regeneration in the AMR, as seen on Figure 2.9. For that reason, only the number of insulator layers will be optimized. The thickness of the insulators will be $0.2\,mm$, as this is considered thin enough not to increase substantially the magnetized volume.

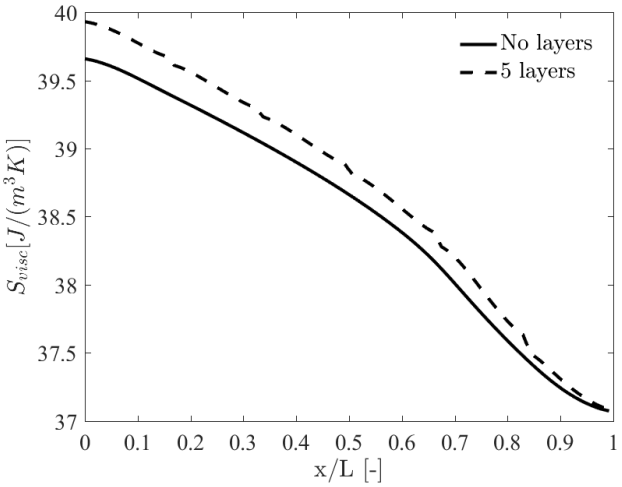

Figure 2.17 Longitudinal distribution of the generated entropy by viscous means, for a steady state cycle working at $f = 0.3\,Hz$ and $\varphi = 0.3$.

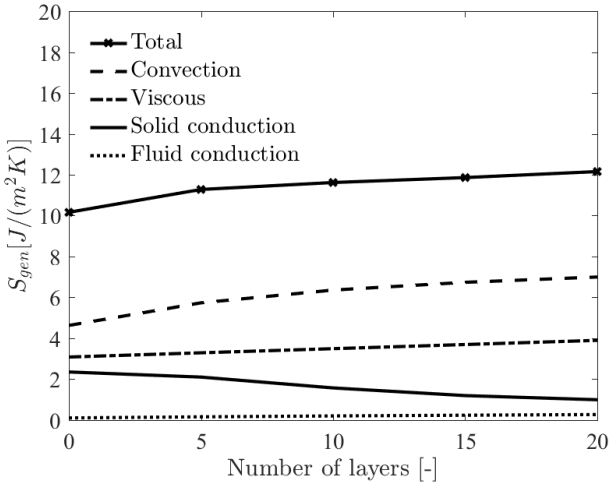

Figure 2.18 Evolution of the generated entropy according to the number of $1\,mm$ insulator spacers at $f = 0.3\,Hz$ and $\varphi = 0.3$. The values presented here are the integration along x of $S_{Scond}, S_{Fcond}, S_{Svisc}$, and S_{gen}.

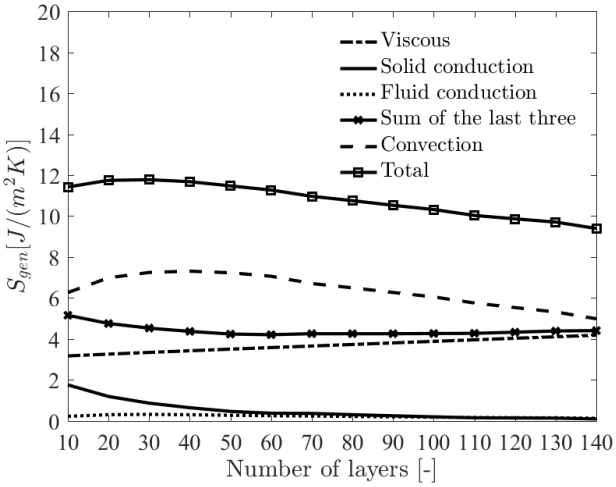

Figure 2.19 Evolution of the generated entropy according to the number of $0.2\,mm$ insulator spacers at $f = 0.3\,Hz$ and $\varphi = 0.3$. The values presented here are the integration along x of $S_{Scond}, S_{Fcond}, S_{Svisc}$, and S_{gen}.

Figure 2.19 extends the results of Figure 2.17 for the case of $0.2\,mm$ thick layers. It shows that for the cases with more than 40 layers S_{conv} starts to decrease. This means, that the gain in magnetocaloric work seen under 40 layers is now reduced. In fact, the insulator layers have been further introduced around the area working at T_C. So the points that were working around T_C have been taken further apart by the jumps in temperature of the insulator layers. The MCM is now divided into segments that work approximately at a constant temperature, and thus there is little heat conduction (see Figure 2.19). It would be ideal if in each of these temperature steps there was an MCM with a T_C tuned to the temperature of the segment. That way the highest MCE could be attained with very small values of S_{Scond}.

Minimizing the rest of the contributions to the generated entropy could be another optimization goal. So, the optimal number of layers is searched for the minimum generated entropy by solid and fluid conduction, and viscous losses. As S_{Scond} is reduced, S_{visc} increases with the length of the regenerator. Also, as more insulators are intercalated in the regenerator, there is more PET material to absorb or release heat at the (de)magnetization and idle time frames. Consequently, the average temperatures of the insulators are closer to the adjacent MCM segments at the end of (de)magnetization processes (in contrast to the case of Figure 2.13). This lessens the initial increment of S_{Fcond}, as the ∇T in the insulators diminishes, and so does the bypassed heat conduction though the HTF. In Figure 2.19 the minimum generated entropy for the sum of these three contributions appears to be around 60 layers. That means an additional length of $12\,mm$ for the magnetic

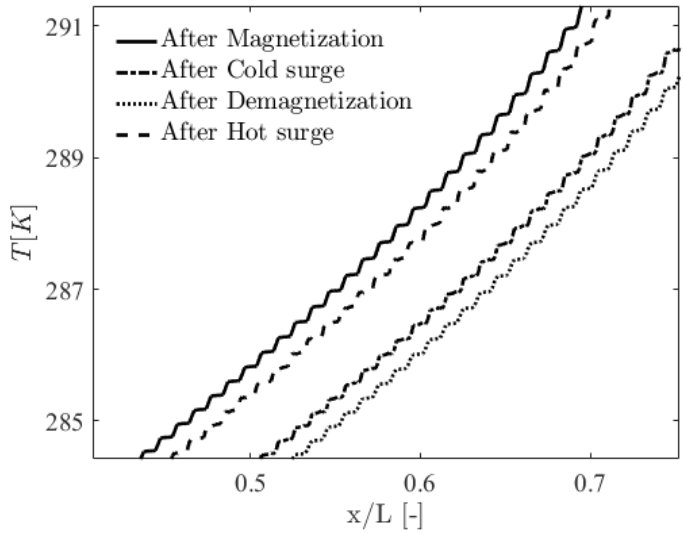

Figure 2.20 Steady state temperature distribution of the tested regenerator with 100 layers of $0.2\,mm$ at $f = 0.3\,Hz$ and $\varphi = 0.3$.

regenerator (a total regenerator length of $92\,mm$). With that information, the designer could evaluate if the lower S_{gen} is worthy of increasing the magnetized volume.

2.2.5 Conclusion

This study constitutes an attempt to reduce the conduction losses in magnetic regenerators by a solution that is easy to manufacture. This consists in reducing the longitudinal thermal conduction within the MCM, by the insertion of insulator layers. Results show higher temperature spans at zero cooling power, higher Q_{cool}, and higher COP with the same amount of MCM and same H_{app}.

There are two other aspects associated with the insertion of insulator spacers that could be detrimental to the system. First one would be the way in which the regenerator is magnetized. If the magnet moves parallel to the HTF (Figure 2.21), the force required to move the magnet will increase. This happens because the insulators have no net magnetization and thus the magnetic forces that appear because of a change in the magnetic field ($dF = (M \cdot \nabla)HdV$) become unbalanced along the length of the insulators. The second aspect would be an increased area to magnetize due to a longer regenerator. That would mean a bigger magnet, and thus a more expensive system.

Therefore, if insulators are introduced in the regenerator, they should be as thin as possible to limit the size of the magnet and the force to move it. As commented in the earlier

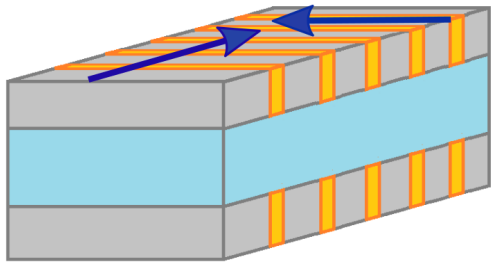

Figure 2.21 Different directions in which the permanent magnet can magnetize the regenerator.

section, there is little interest in increasing the thickness of the layers, as it does not reduce substantially S_{Scond}. If the designer would want more regeneration in the system, instead of increasing the thickness of the insulator layers, it would be more adequate to introduce a passive regenerator outside the magnetized volume to avoid increasing the force to move the magnet, and the magnetized volume.

Also, the origin of having a considerable S_{conv} lays on the characteristics of the Brayton cycle. If the geometry of the regenerator is fixed, the increase of S_{conv} can be lowered by a hybrid Brayton-Ericsson cycle as seen in [71]. On one hand, the adiabatic (de)magnetization process of the Brayton cycle produces a higher temperature difference between the MCM and the HTF. This enables a fast heat transfer and thus a higher cooling power by making more cycles per second. On the other hand, the isothermal processes of the Ericsson cycle lower S_{conv} by having a small temperature difference between MCM and HTF and thus, this leads to higher COPs. Thereby, the Hybrid Brayton-Ericsson cycle could be tuned to get the most out of the benefits of introducing the insulator layers in a magnetic regenerator.

Simulations in this study have shown that there is a compromise between reducing S_{Scond} and incrementing the magnetocaloric work by introducing insulator layers. Results suggest that the areas working around T_C should not be excessively divided, in order to have as much points working around T_C as possible. That is why the technique of inserting insulators would work best in multi-material regenerators, in which each segment of MCM would have a levelled temperature profile, working around the designated T_C.

2.2.6 Acknowledgments

This work is part of the NSERC chair on industrial energy efficiency established at Université de Sherbrooke in 2014 with the support of Hydro-Québec, Ressources Naturelles Canada (Canmet ÉNERGIE-Varennes) and Rio Tinto Alcan that are gratefully acknowledged for their financial support. We would like to thank also Professor Engelbrecht (DTU) for the fruitful discussions we had.

2.2.7 Nomenclature

A	Area	$[m^2]$
c	Heat capacity	$[J \cdot kg^{-1} \cdot K^{-1}]$
D	Demagnetization factor	$[-]$
D_h	Hydraulic diameter	$[m]$
F	Force	$[N]$
$\mathfrak{F}$	Magnetomotive force	$[A]$
h	Heat transfer coefficient	$[W \cdot m^{-2} \cdot K^{-1}]$
H	Magnetic field	$[A \cdot m^{-1}]$
$\dot{m}$	Mass flow	$[kg \cdot s^{-1}]$
M	Magnetization	$[A \cdot m^{-1}]$
Nu	Nusselt number	$[-]$
$\dot{Q}$	Heat per volume	$[W \cdot m^{-3}]$
r	Aspect ratio	$[-]$
$\mathfrak{R}$	Reluctance	$[A^2 \cdot J^{-1}]$
$\dot{S}$	Generated entropy	$[W \cdot m^{-3} \cdot K^{-1}]$
T_C	Curie temperature	$[K]$
V	Volume	$[m^3]$

Greek symbols

Φ	Magnetic flux	$[J \cdot A^{-1}]$
φ	Utilization factor	$[-]$
λ	Thermal conductivity	$[W \cdot m^{-1} K^{-1}]$
μ	Magnetic permeability	$[N \cdot m^{-2}]$
ρ	Density	$[kg \cdot m^{-3}]$

Subscripts

0	Vacuum
app	Applied
cool	Cooling
eff	Effective
f	Fluid
r	Relative
rej	Rejected
s	Solid

Acronyms

HTF	Heat Transfer Fluid
MCE	Magneto Caloric Effect
MCM	Magneto Caloric Material
MFT	Mean Field Theory
PET	PolyEthylene Terephthalate

CHAPTER 3

An Open Source DNS solver for the simulation of Active Magnetocaloric Regenerative cycles

3.1 Avant-propos

Auteurs et affiliations:

1. Ibai Mugica: étudiant au doctorat*
2. Sébastien Poncet: professeur*
3. Jonathan Bouchard: chercheur**

*Université de Sherbrooke, Faculté de génie, Département de génie mécanique.
**Laboratoire des Technologies de l'Énergie, Hydro-Québec, Shawinigan.

Date d'acceptation: 3 Juin 2018

État de l'acceptation: version finale publiée

Revue: Applied Thermal Engineering

Titre français: Un solveur DNS Open Source pour la simulation de cycles de régénération magnétocalorique active

Contribution au document: Cet article contribue à la thèse en présentant une validation détaillée d'un nouveau solveur de cycle 3D AMR et en déterminant l'influence des phénomènes physiques couplés.

Résumé français: Cet article décrit le développement d'un nouveau solveur multiphysique polyvalent, dont l'objectif final est de caractériser les cycles de régénération magnétocalorique active (AMR). La description est suivie d'une validation approfondie divisée en deux parties. Tout d'abord, les simulations des phénomènes physiques pris séparément sont validées (génération de la géométrie poreuse, écoulement de fluide, transfert de chaleur conjugué et champ magnétique). Ensuite, l'ensemble du code AMR est comparé à un prototype expérimental. Les résultats sont dans tous les cas proches des données numériques ou expérimentales publiées. Deux mécanismes de couplage sont également étudiés: la dépendance de la viscosité

du fluide caloporteur en fonction de la température et l'influence de la perméabilité magnétique sur le champ magnétique interne du gadolinium. Les deux effets s'avèrent négligeables pour calculer le champ de température d'un régénérateur magnétique (MR). De plus, en négligeant ces effets, les champs magnétiques et de flux du MR peuvent être calculés à l'avance, ce qui réduit considérablement la charge de calcul au moment de l'exécution. Enfin, la parallélisation du solveur multiphysique est évaluée.

Connection with previous chapter: As it has been made clear by Figure 2.7, the solution computed with 1D solvers can vary substantially depending on the models and hypothesis we choose for them. In an effort to produce a solver that is as reliable as possible, the current chapter explores the direct numerical resolution of the physical phenomena involved in the regenerator. In fact the sections of this chapter concentrate heavily on the validation of a 3D solver, to demonstrate that it produces a trustworthy solution of the AMR.

3.2 An Open Source DNS solver for the simulation of Active Magnetocaloric Regenerative cycles

This paper describes the development of a new versatile multiphysics solver, whose final objective is to characterize Active Magnetocaloric Regenerative (AMR) cycles. The description is followed by a thorough validation divided in two parts. First, the separate simulations of the constituent physics are validated (porous geometry generation, fluid flow, Conjugate Heat Transfer and magnetic field). Then, the whole AMR code is compared to a measured prototype. The results are in all cases close to published numerical or experimental data. Also, two coupling mechanisms are studied, the temperature dependency of the viscosity of the Heat Transfer Fluid (HTF), and the influence of the magnetic permeability on the internal magnetic field of Gadolinium metal. Both effects prove to be negligible to compute the temperature field of a Magnetic Regenerator (MR). Moreover, by neglecting these effects the magnetic and flow fields of the MR can be computed beforehand, which reduces substantially the computational load at run time. Finally, the speed-up of the parallel multiphysics solver is evaluated.

3.2.1 Introduction

Part of the general research on refrigeration technology is focused on the development of alternative refrigeration cycles to the well established vapor-compression technology.

The objective of this research domain is to minimize the drawbacks of vapor-compression cycles, which include: ozone depletion potential, toxicity of refrigerants, noise, and energy consumption. Several alternative technologies have been ranked by [33] attending to their potential to substitute vapor-compression cycles. The likeliness for substitution was weighted by the criteria of energy savings and development status. The first five technologies in the ranking include: Elastocaloric (or Thermoelastic), Evaporative desiccant, Membrane Absorption, and Magnetocaloric cycles. It is yet unclear which could be the next mass marketed technology, as they all require further research.

This publication focuses on Active Magnetocaloric Regenerative (AMR) cycles, where the working refrigerant is a solid with magnetocaloric properties. [41] recently published a book that covers most of the engineering aspects surrounding this technology. Similar to vapor-compression, AMR cycles use a phase transition to create a thermodynamic cycle based on Magneto-Caloric Materials (MCM). This magnetic phase transition happens around the Curie temperature of the material (T_C), where relatively small variations of temperature or magnetic field cause a transition between para- and ferromagnetic states. This magnetic phase transition abruptly changes the entropy state of an MCM. As a consequence other thermodynamic properties, such as heat capacity, experience an abrupt change too. This effect modifies the thermal equilibrium of the MCM with its environment, causing the Magneto-Caloric Effect (MCE). Predominantly, when the internal magnetic field of an MCM increases, its temperature increases too and vice versa (although there are some MCMs with an inverse effect, see [43]).

The temperature increase (or decrease) produced by the MCE is generally too small to be used in conventional refrigeration cycles . [4] estimate that most refrigeration systems need at least a 50K temperature span to operate. E.g. Gadolinium (Gd) at its T_C (around 295K) undergoes a maximum adiabatic temperature increase of approximately 5.5K, when the internal magnetic field goes from 0 to $2T$ ([23]). Thus, to produce a reasonable temperature difference in a refrigerator, several thermodynamic cycles need to be consecutively connected. This goal has been attained most effectively by the use of active regenerators. Generally, regenerators are devices that allow to store heat that is released into another thermodynamic cycle. Instead, in AMR cycles, the Heat Transfer Fluid (HTF) directly connects the thermodynamic cycles in question, and the heat capacity of the MCM is used as a regenerator to absorb (or release) the heat from a neighboring cycle. Therefore the working solid becomes the regenerator itself, and thus the adjective “active”. The thermodynamics and properties of the cycles that Magnetic Regenerators (MR) can undergo, have been studied in detail by [39].

AMR cycles have lead to various prototype configurations, but there are 5 items that are always present: the active regenerator, the HTF and its pumping system, the magnet, and the heat exchangers at the heat sink and source. AMR systems are usually operated following a Brayton cycle. Fast (de)magnetization increases (or reduces) adiabatically the temperature of the regenerator, and then pumping the HTF links thermally the neighboring cycles and the heat sink and source. Active regenerators tend to be quite packed with MCM (solid porosity, $\varepsilon_s = \frac{V_{MCM}}{V_{Total}} \approx 0.3$, see [41]), because the magnetized volume drastically increases the prize of the necessary permanent magnet. This means that, for an MR to pump heat at a relevant rate, the consecutively connected AMR cycles are close together in the magnetized volume. This gives rise to conduction heat losses due to the proximity of the MCM working at different temperatures between the heat sink and source.

Three main regenerator geometries have been successfully implemented in an AMR cycle so far: packed beds, plates and wire stacks. However there are some exceptions like the pins considered by [92]. [107] and [37] have gathered many publications that describe chronologically the evolution of MRs. Packed beds have shown the biggest cooling powers so far, therefore, the closest refrigerators to have a practical application are made of randomly stacked MCM particles. [36] developed a refrigerator capable of delivering a maximum of 3kW of cooling power, and [35] one of 100W. There is an exception to these, a plate regenerator developed by Cooltech ([98]) which provides at least 200W. One of the advantages of plate regenerators is the reduced pumping work. Many other prototypes have employed plate regenerators, but their lower cooling power relegates their usage to research purposes. A wire regenerator has been recently presented by [42]. It combines the tight packing of packed beds and the unobstructed flow of plate regenerators. However the difficulty of extruding the brittle MCM into thin wires, makes the price of this type of regenerators not very competitive at moment. Recently, efforts have been made to further develop rotatory prototypes due to their higher efficiency (see [50], [4], and [29]).

When it comes to the regenerator itself, the main design goals are to pack as much magnetocaloric work as possible in the magnetized volume, while still having low shape demagnetization, excellent heat transfer towards the HTF, low conduction losses, and minimum pumping work of the HTF.

Naturally, it is quite a challenge to optimize such a multiobjective system. Nevertheless, numerical models of AMR cycles reduce the uncertainty of the performance of next generation prototypes. [5], [22], and [28] constitute examples in which numerical models are used to predict the performance of MRs when small variations are introduced. [62] and [37]

compiled a good number of published numerical models. To understand the constraints of these models, it is useful to classify them by the degree to which the underlying physical phenomena are solved or modeled. Table 3.1 compiles some of the most relevant numerical solvers published in the last decade.

The production of this 3D DNS AMR cycle solver was motivated by the difficulties involved in the development of MRs. These include, high capital cost of MCMs and permanent magnets, the inexperience of manufacturing fine geometrical structures with brittle MCMs, and the few measurements available after the construction of prototypes, due to the inaccessibility of the MRs during operation. Some advancements have been done recently regarding these areas (see [86], [87], [93], and [19] respectively). However, the ability to reliably simulate MRs reduces the number of prototypes needed to develop high performance magnetic refrigerators. Moreover, if the software necessary to run the simulations is Open Source, research groups would not be obstructed by license costs, and they could potentially use the full capacity of their computational clusters.

As explained, plenty of numerical solvers have been developed in the past. Nonetheless, they have been widely populated by estimations and hypotheses that reduce the scope of the design process to already studied geometries.

To the best of the authors knowledge, this solver yields the most detailed data on MRs so far. In essence, it solves directly the spatial and temporal variations of the hydrodynamic, thermal and magnetic fields during the thermodynamic cycle that MRs undergo during their operation. Also, it could be easily modified to solve other cycles where the working substance is a solid, such as: thermoelastic, electrocaloric or barocaloric cycles.

Accurate numerical models should in principle provide a realistic prediction of all these four phenomena shown in Table 3.1 (MCE and thermal, fluid, and magnetic fields). This is somewhat challenging, because it is yet unclear how deep are these phenomena coupled to each other. For example, Figure 3.1 shows the relative magnetic permeability (μ_r, see Equation (3.1)) of Gd, calculated form the magnetization measurements of [44].

$$\mu_r = 1 + \frac{H}{M} \tag{3.1}$$

There, it can be seen how for temperatures below T_C, μ_r substantially varies from 0 to 2 T. Figure 3.2 expresses what is the influence of constant shape demagnetization for a given μ_r (Equation (3.2)). To do so, one defines the parameter η as:

Reference	*MCE*	*Thermal Field*	*Flow Field*	*Magnetic Field*	*Coupling*
[70]	MFT	2D CHT	2D DNS	Uniform internal field	Energy and MCE
[13]	MFT	3D CHT	3D DNS	3D Magneto-Static	All Coupled
[66]	Measurements	2D CHT	2D Analytical	Uniform internal field	Energy and MCE
[17]	Measurements	2D CHT	2D DNS	Uniform internal field	Energy and MCE
[103]	Measurements	1D	Uniform	1D model	Energy, MCE and Magnetic field
[77]	Measurements	1D	Uniform	3D Magneto-Static	Energy, MCE and Magnetic field
[64]	Measurements	1D	Uniform	Uniform internal field	Energy, MCE and Magnetic field
[16]	Measurements	1D Semi-Analytic	Uniform	Demagnetization approx.	Energy, MCE and Magnetic field
[89]	MFT	1D	Uniform	Demagnetization approx.	Energy, MCE and Magnetic field
[49]	Measurements	2D CHT	2D DNS	Demagnetization approx.	Energy and MCE
[2]	Measurements	2D CHT	2D DNS	Uniform internal field	Energy and MCE
[37]	MFT	3D CHT	3D DNS	Uniform internal field	Energy and MCE
[65]	MFT	1D	Uniform	Demagnetization approx.	Energy, MCE and Magnetic field
[82]	MFT	1D	Uniform	Uniform internal fieldl	Energy and MCE
[55]	Measurements	1D	Uniform	1D model	Energy, MCE and Magnetic field

Table 3.1 Summary of the latest AMR cycle solvers. CHT stands for Conjugated Heat Transfer, DNS for Direct Numerical Simulation, and MFT for Mean Field Theory.

$$\eta = \frac{H_{int}}{H_{app}} = \frac{1}{1 + D(\mu_r - 1)} \tag{3.2}$$

The expression of Equation (3.2) is constrained to uniformly applied magnetic fields (H_{app}), and bodies with constant magnetization (ellipsoids). Nevertheless, from Figures 3.1 and 3.2 it can be inferred that for the temperatures below T_C of Gd, the interior magnetic field (H_{int}) could vary substantially from the applied magnetic field (H_{app}) due to a non uniform temperature distribution, even for low demagnetization geometries.

So, during this study, the following coupling mechanisms will be investigated:

1. The viscosity of the HTF could vary substantially in the temperature range of the Magnetocaloric Regenerator (MR). For example, in the case of water, ν ranges between 1.785 and $0.8 \cdot 10^{-6} m^2 \cdot s^{-1}$ in the range of 0-30°C ([21]), which means the local Reynolds number (Re) could double from one place to another in a MR. Differences in Re could give rise to variations of the local velocity profile, potentially changing the properties of heat transfer by convection.
2. As explained before, the internal magnetic field of the MCM is subject to geometry (D) and magnetization properties (μ_r). In addition, [79] and [11] have shown how groups of certain geometrical shapes (plates, cylinders, spheres) under a uniform external magnetic field, have higher demagnetization in groups than when they stand alone. The magnetization of an MCM depends on its internal magnetic field and temperature, which makes the resolution of the magnetic field a nonlinear problem.
3. The MCE varies substantially with the internal magnetic field and temperature. Indeed, the origin of the MCE can be traced back mathematically to changes in magnetization ($dT = \frac{\mu_0}{c_H} \frac{\partial M}{\partial T}\big|_H T dH$, [39]), which as explained before, is a nonlinear problem.
4. The temperature field connects all the other physical phenomena in a thermodynamic cycle that should reach a steady state equilibrium. This requires the transient solution of the energy equation, and therefore, the transient solution of the phenomena that are closely coupled to the temperature field too.

On top of the copious coupled physical phenomena, the need for a fast heat transfer towards the HTF from a relatively small temperature difference, has led engineers to build prototypes with large heat transfer surfaces (e.g. packed bed regenerators). This means that the fine spatial resolution needed to numerically model the physical phenomena is often prohibitive in terms of computational resources.

Taking the aforementioned points into account, the aim of this study is twofold:

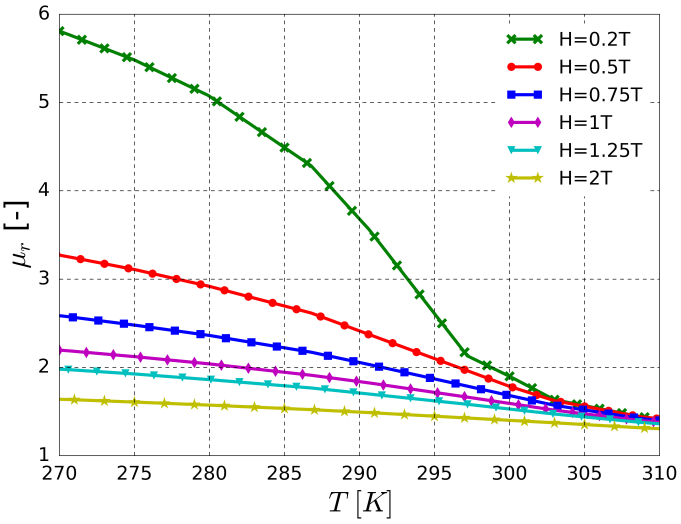

Figure 3.1 Magnetic permeability of Gd metal, calculated from magnetization measurements ([44]) and Equation (3.1).

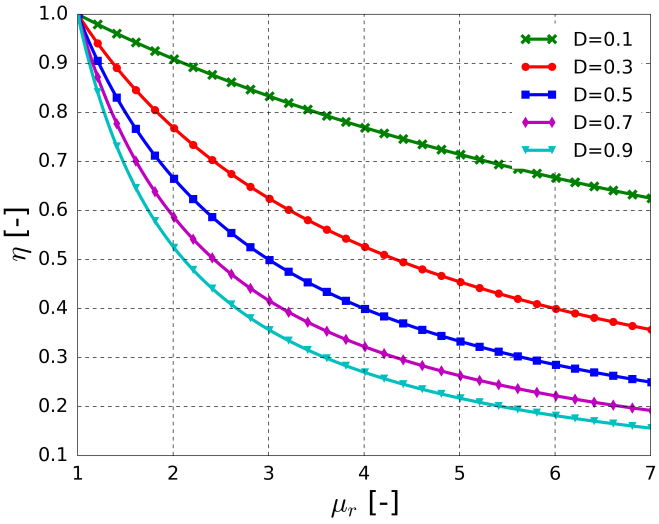

Figure 3.2 Evolution of the ratio between the internal and applied magnetic field $\eta = \frac{H_{int}}{H_{app}}$ as a function of the magnetic permeability, for uniformly magnetized ellipsoids (see Equation (3.2)).

1. To study the coupling of the underlying physical phenomena in AMR cycles, in order to assess whether it is reasonable or not to decouple phenomena and reduce the computational load.

2. To provide a validated solver that will permit to accurately compute both existing, and radically new Magnetocaloric Regenerators. Solutions could be used to study a certain regenerator in detail, or to extract data for a 1D AMR numerical solver (like the Nusselt number (Nu) or the average internal magnetic field).

This paper is organized in the following way. First, the method to generate the geometry of randomly packed beds is explained and validated in section 3.2.2. Then the details of the numerical solver are presented in depth in Section 3.2.3. A separate validation of all the constituent phenomena follows in Section 3.2.4. At the end, the performance of the whole solver is benchmarked to an experimental set up. Finally, the parallelization properties of the solver are presented in Section 3.2.5 before some conclusions in Section 3.2.6.

3.2.2 Geometry generation

Magnetocaloric Regenerators (MR), as already explained, tend to be made of MCM packed beds. This increases the heat transfer surface, while permitting a tight packing of the MCM in a reduced volume. That is why, to have a complete procedure to calculate any AMR cycle, the method proposed by [12] will be further validated. [12] described a method to generate randomly packed beds from arbitrary shape particles. The employed software is Blender, which can effectively simulate Newton's equations of motion and elastic collisions with Bullet Physics Library (bulletphysics.org). Blender has its own Python library, which is key to automatize the geometry generation. The Python tool developed in this study employs arbitrary receptacle and particle geometries. The particles are set in an initial matrix, and then they fall by the action of gravity into the receptacle. It is possible to specify a random bounded variation of the original particle size, and a bounded noise in the positions of the particles in the initial matrix. [12] also commented that it is important to set a low enough elastic dissipation and friction coefficients. This way, the falling particles will have better chances of rearranging themselves and not generate voids in the packing. Table 3.2 shows some typical values of these coefficients.

The fluid and solid domains, defined by the particles of Figure 3.3, were discretized using the native OpenFOAM mesher, snappyHexMesh. This software refines a primitive mesh around the input enclosed surface. Then, the user specifies a reference point to choose which side of the mesh is to be saved (sides are defined by the enclosed geometry). This set

Parameter	*value*
Size variation	1
Initial position	0.2
Elastic dissipation	0.9
Friction coefficient	0.3

Table 3.2 Example of the coefficients used in the geometry generation of the particle stacks of Figure 3.3.

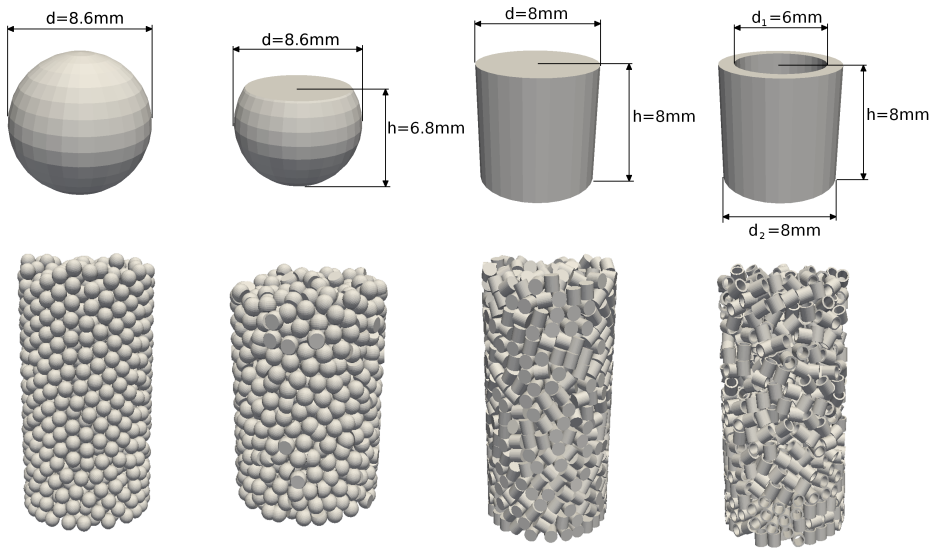

Figure 3.3 Up, dimensions of the particles stacked by [32]. From left to right spheres, deformed spheres, cylinders and Raschig rings. Down, respective packed beds generated with Blender. The packed beds are 80 mm in diameter, as in the experiments described by [32].

of operations treat the singular contact point between the particles by making a "bridge" between them (Figure 3.4). The more the mesh is refined, the more thin this bridge is. According to [25] this seems to be the best strategy to calculate phenomena in porous media, specially when dealing with heat transfer cases. This technique adds some extra heat transfer surface between the particles. To know whether or not the generated geometries represent adequately the real packed beds, the porosity ($\varepsilon = \frac{V_{gap}}{V_{Total}}$) distribution of packed beds was studied.

Figure 3.5 shows the distribution of porosity averaged over the circumference of a given cylinder radius r (so $R - r$, is the distance from the outer side of the packed bed). The generated fine and medium meshes match exceptionally well the experimental data from [32]. In their experiments, the authors measured the porosity and fluid velocity profiles of various packed beds. The measurements were done by filling a cylinder of 80 mm in diameter with the particles of Figure 3.3 and then gradually emptying the cylinder of a fluid to measure the fraction of volume that belong to the interstices. The largest discrepancy is observed for the stacking of Raschig rings, near the center of the packed cylinder (Figure 3.5). Nevertheless, the results shown in Figure 3.5 show a relative improvement when compared to the simulations done by [12].

3.2.3 Description of the numerical solver

The resolution of the partial differential equations describing the phenomena in MRs is done in the OpenFOAM framework. OpenFOAM consists on a C++ library of Finite Volume Method (FVM) solvers, closely related to computational fluid dynamics. In its essence though, is a mathematical tool that permits any Field Operation And Manipulation (FOAM). An advantage of FVM solvers is that they are conservative in their mathematical formulation. The numerical flux between cells is always conserved and thus, any conservation principle too. The general discretization of partial derivatives is already implemented, and the differential equations can be coded with a rather intuitive syntax.

Once the solver routines are coded in a main C++ program, the user is able to specify the discretization methods for each term of the equations, the iterative method to solve the resulting linear matrix, the under-relaxation coefficients of equations, and tolerances for each iterative procedure. The equations that drive the AMR cycle solver are the following:

$$\nabla \mathbf{u} = 0 \tag{3.3}$$

$$\frac{\partial \mathbf{u}}{\partial t} + (\mathbf{u} \cdot \nabla)\mathbf{u} = -\nabla p + \nu_f \nabla^2 u \tag{3.4}$$

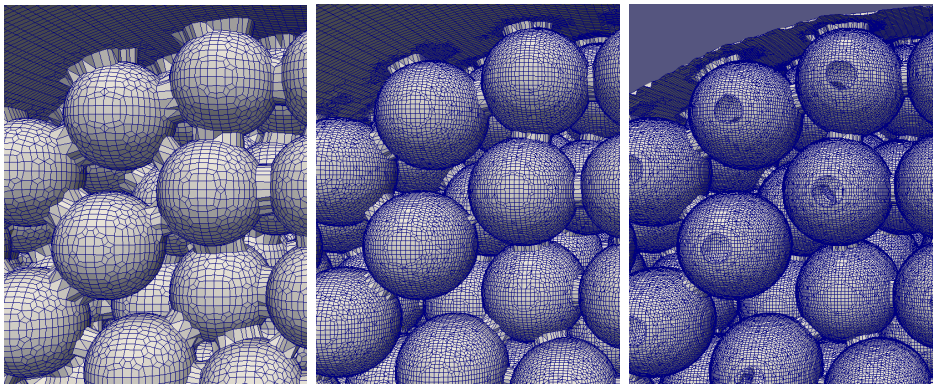

Figure 3.4 Surface mesh over consecutive refinements of the sphere filled packed bed. The characteristic length of the surface cells is $666\mu m$, $444\mu m$ and $350\mu m$ from left to right. The "bridges" at the contact points are reduced every time the surface mesh is refined.

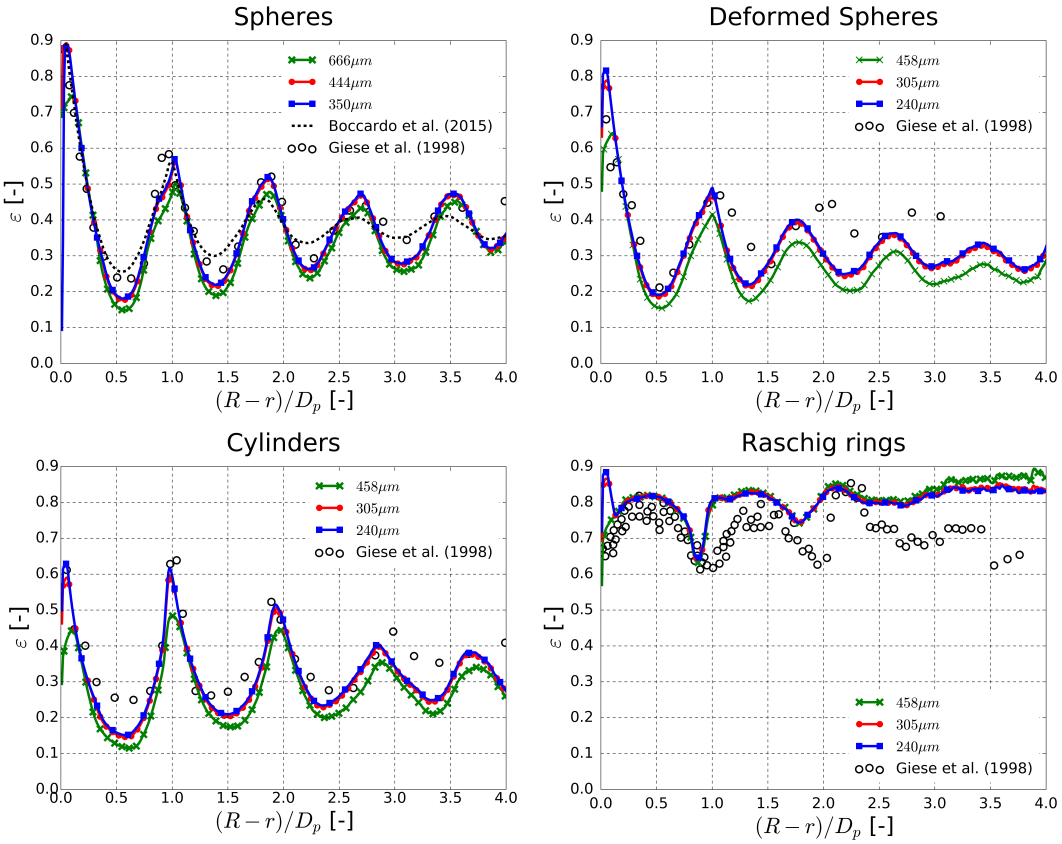

Figure 3.5 Radial porosity of the different packed beds presented in Figure 3.3. Lines represent different surface cell characteristic lengths.

$$\nabla \cdot (\mu \nabla \varphi) = 0 \tag{3.5}$$

$$c_H \frac{\partial T}{\partial t} + \mu_0 T \left.\frac{\partial M}{\partial T}\right|_H \frac{\partial H}{\partial t} = \frac{\lambda_s}{\rho_s} \nabla^2 T \tag{3.6}$$

$$\frac{\partial T}{\partial t} + \mathbf{u} \nabla T = \frac{\lambda_f}{\rho_f c_f} \nabla^2 T \tag{3.7}$$

Note that the temperature increase due to viscous dissipation in Equation (3.7) was omitted. The fluid velocity field $\mathbf{u}$, will determine the transport of heat in the fluid domain, and thus the level of regeneration in the machine. This field is calculated by the Navier-Stokes and fluid continuity equations ((3.3) and (3.4)). The internal magnetic field intensity H drives the MCE in Equation (3.6). This variable determines the magnetization of the MCM as explained in the introduciton ($M = M(H, T)$). The H field is recovered from the magnetic potential ($\mathbf{H} = -\nabla\varphi$). The magnetic potential φ is calculated by the magnetostatic potential in Equation (3.5). This equation is solved in the MCM and its non-magnetic surroundings. Finally, the temperature field T is computed from the coupled solution of Equations (3.6) and (3.7).

In the following subsections the resolution of each of these equations is detailed separately. At the end of this section, the whole AMR cycle solver will be presented.

Flow field

The simpleFoam solver in OpenFOAM library is dedicated to solve incompressible flow continuity and momentum Equations (3.3) and (3.4). The pressure-velocity coupling is treated with the SIMPLE algorithm (see [100]). SimpleFoam has widely been used in the past and consequently validated (e.g. [63]). Nevertheless, section 3.2.4 checks if the produced packed bed meshes are sufficiently accurate to calculate the fluid flow that runs through porous structures. In addition, the influence of Re on the velocity profiles of porous media will be investigated to clear the weight of the first coupling mechanism presented in the introduction.

MCE

As explained in the introduction, the MCE happens due to a sudden change of the thermodynamic properties of the MCM. The heat exchanged by the MCM can be expressed by two kinds of heat capacities: at constant field c_H, and at constant temperature c_T.

$$dq = c_H dT + c_T dH \tag{3.8}$$

The following expression for c_T can be derived from a Maxwell relation:

$$c_T = \mu_0 T \left.\frac{\partial M}{\partial T}\right|_H \tag{3.9}$$

By adding the Fourier law of conduction, Equation (3.8) becomes Equation (3.6). The data characterizing the MCM ($\left.\frac{\partial M}{\partial T}\right|_H$ and c_H) is implemented through 2D tables that are later interpolated. Temperature and internal magnetic field are used as inputs to get the values of $c_H = c_H(H,T)$, and $\frac{\partial M}{\partial T} = \frac{\partial M}{\partial T}(H,T)$. Thus, the implementation of any kind of MCMs is straight forward.

Conjugate Heat Transfer

MCM and HTF temperature fields were solved in separate meshes, because different information needs to be loaded to them (Equation (3.6) for the MCM and Equation (3.7) for the HTF). The MCM mesh needs the values of the internal magnetic field, and the HTF mesh the values of the fluid flux. Also, MCM and HTF domains need to exchange information at their common boundaries through Equation (3.10) (conservation of energy through the interface). This is generally called a Conjugate Heat Transfer (CHT) problem.

$$\lambda_s \frac{\partial T_s}{\partial n} = \lambda_f \frac{\partial T_f}{\partial n} \tag{3.10}$$

OpenFOAM already provides a CHT solver (chtMultiRegionFoam), but is formulated with ρ_{HTF} as a variable. This is to account for buoyancy employing the Boussinesq approximation. In fact, the maximum Richardson number (see Equation (3.11)) of an MR was calculated here with conservative estimations for its parameters $Ri = 3.65 \cdot 10^{-2}$ ($g = 9.81 m \cdot s^{-2}$, $\beta = 207 \cdot 10^{-6} K^{-1}$ for water (see [67]), a $\Delta T = 5K$ along the thickness of the channel, $L = 1mm$, and the maximum velocity of this study $u = 16.67 mm \cdot s^{-1}$). So, the fine geometric structures of regenerators, the low temperature differences, and rapid fluid surges make natural convection a negligible effect in MRs.

$$Ri = \frac{g\beta\Delta T L}{u^2} \tag{3.11}$$

This reduces significantly the computational resources of the new CHT solver, where ρ_{HTF} and ν_{HTF} are constant. In order to maintain the conservative nature of FVM, the resolution of Equation (3.7) is done in the same mesh employed to calculate the velocity

field. So, the flux between cells ($m^3 \cdot s^{-1}$) from the velocity field calculations, is directly fed to the CHT solver in order to calculate the convective heat transport.

The CHT solver starts first by solving the solid domain until the initial residual is under a tolerance defined by the user. Then, the same happens with the fluid domain. There is an routine that wraps both domains in order to control the residual of the coupled solution. Every time the solid or fluid domains are solved, the interface boundary condition needs to be updated. The updated boundary temperature T_B is calculated by discretizing Equation (3.10) with a 1st order method:

$$\lambda_s \frac{T_s - T_B}{\delta_s} = \lambda_f \frac{T_B - T_f}{\delta_f} \tag{3.12}$$

This 1st order discretization is proven to be sufficient in the coming section 3.2.4. Because regenerators have usually a large heat transfer surface, the discretization of Equation 3.12 means that effectively, the order of accuracy of the temperature field will be closer to 1st order methods. If the user finds out that 1st order accuracy is not sufficient for their application, time should be devoted to code an OpenFOAM function that recovers values further from the first set of cells that are adjacent to the boundary. Alternatively this issue could be circumvented by refining the mesh at the interface boundary. T_f is interpolated to the faces of the solid mesh and vice versa for T_s. This means that if the mesh interfaces are not conformal, the numerical flux at the boundary will not be automatically conserved. No issues have been found in this study to achieve a converged solution, where the energy at the interface is practically conserved. However it does make the FVMs slower to converge.

Magnetic Field

The magnetic field that crosses MRs changes through space and time, and therefore it should in principle generate eddy currents in conductive materials. However, the fine geometric structures of regenerators allow to neglect the magnetic response of eddy currents. On the one hand, packed beds have the MCM broken apart in small particles. On the other hand, plates usually have the applied field parallel to the plates to reduce shape demagnetization. If this is the case, the electric field is confined to the thickness of the plates according to Lenz's law. Thus, it becomes apparent that is only necessary to solve the magnetostatic field for each magnet position. Knowing that $\mathbf{B} = \mu\mathbf{H}$, the simplified Maxwell Equations (3.13) and (3.14) make possible the use of a scalar potential function

defined by $\mathbf{H} = -\nabla\varphi$ (this leads to Equation (3.5)).

$$\nabla \cdot \mathbf{B} = 0 \tag{3.13}$$

$$\nabla \times \mathbf{H} = 0 \tag{3.14}$$

In the context of this study, magnetic permeability $\mu = \mu_0\mu_r$ is considered isotropic, but not always homogeneous. This makes the resolution of the internal magnetic field a non linear problem, as $\mu_r = \mu_r(H, T)$. OpenFOAM already has a magnetostatic solver called magneticFoam, but it does not allow for the coupled solution of different domains through a mesh interface. Also, in magneticFoam μ_r can only be isotropic and homogeneous, and the magnet needs to be defined within the mesh. In the case of MRs, the magnetic field lines are tightly confined between the poles of a magnet, so their action can be simplified through a boundary condition with a constant $\frac{\partial\varphi}{\partial n}$. This enables the user to solve the magnetic field in the MR and its non-magnetic surroundings, without including the magnet itself. Thus, apart from a new magnetostatic solver, two more boundary conditions were coded: one for the continuity of the normal magnetic flux between domains (Equation (3.15)), and another one to represent the magnetic field $H = \frac{\partial\varphi}{\partial n}$ of a moving magnet. The later is represented by a fixed gradient at the moving area of the magnet poles, and $\frac{\partial\varphi}{\partial n} = 0$ elsewhere.

$$\mu_1 \frac{\partial\varphi_1}{\partial n} = \mu_2 \frac{\partial\varphi_2}{\partial n} \tag{3.15}$$

Equation (3.15) is conceptually identical to the thermal boundary condition of Equation (3.10). Thus, it is treated as explained before in section 3.2.3, although there is one exception related to the meshing process. As opposed to the CHT problem, the solution of φ is characterized by much larger gradients than T. As an example, a magnet that holds a field intensity of $1T$ at the center of a 40mm gap, creates an approximate potential difference of $\Delta\varphi \approx \frac{B\Delta L}{\mu_0} = 3.09 \cdot 10^4\ A \cdot m^{-2}$ between the poles of the magnet. So, if a non conformal mesh interface is constructed betweeen the MCM and its non-magnetic surroundings, the vector solution $\mathbf{H} = -\nabla\varphi$ will show significant perturbations at the boundary due to the mismatch of cell interfaces (see Figure 3.6).

These perturbations are generally localized at the boundary, and usually do not affect greatly the solution of the internal field of large objects. But in the specific case of MRs, the heat transfer surface of the regenerator is specially large compared to the volume of the MCM. Thereby, the use of conformal meshes to solve the magnetic field becomes

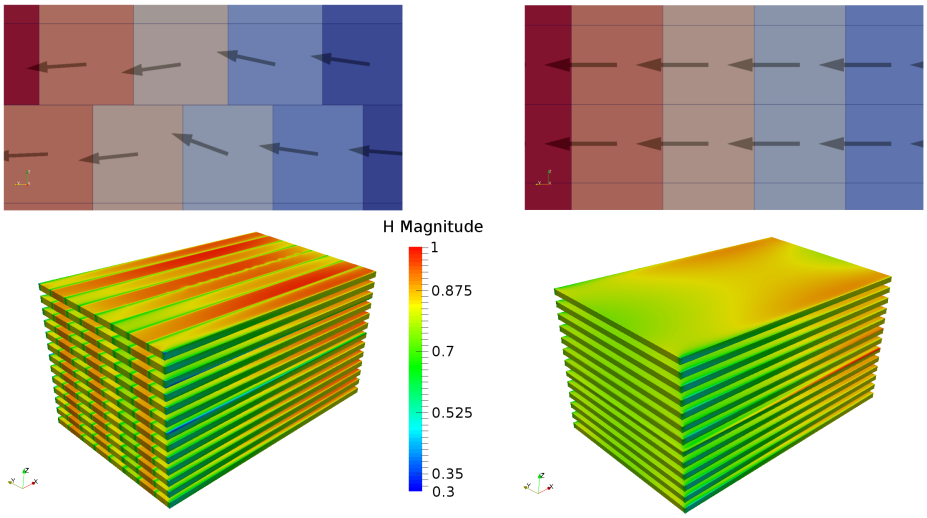

Figure 3.6 Differences in the solution of the magnetic field intensity H for the case presented in section 3.2.4. A non conformal mesh was used in the left, and a conformal one on the right. On top, the vector for $\mathbf{H}$ is represented on the coloring for the potential φ. Below, the coloring represents the magnitude of $\mathbf{H}$

indispensable to avoid miscalculations as shown in Figure 3.6. Moreover, the use of conformal meshes as explained in section 3.2.3 leads to lower computation time, due to the conservation of $\mathbf{B}$ at the interfaces.

AMR cycle

The solver presented in this section calculates the transient evolution of AMR cycles with the help of the models presented in the previous sections. The flowchart of the algorithm is described in Figure 3.7. Two solvers were produced, one for the cases where the magnetic field is heavily coupled to the temperature field (DNSamrFoam), and another one for the cases that is not (decoupledAMRFoam). In the later, the red rectangle of Figure 3.7 is replaced by a routine that updates the magnetic field from a file that is calculated beforehand.

The meshes employed in the calculations of the magnetic field and the fluid velocity, are used to solve the temperature fields on the MCM and HTF domains. The only mesh that is not reused, is the one employed to calculate the magnetic field of the non-magnetic surroundings.

Figure 3.8 states the inputs and outputs of the AMR cycle solver. Regarding the MCM domain, c_H, $\frac{\partial M}{\partial T}$ and M tables need to be supplied. The first two are used in Equation (3.6), and the later is used to calculate the magnetic work of the MCM by the following expression (see [39]):

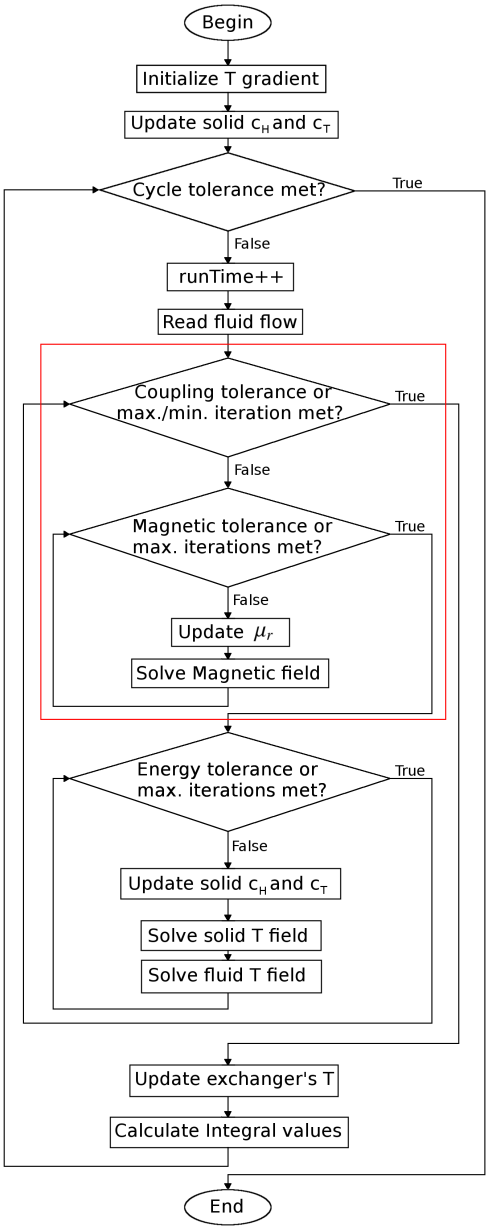

Figure 3.7 Flowchart of DNSamrFoam algorithm. decoupledAMRFoam works the same way, only by replacing the red square for a routine that updates the magnetic field from a file.

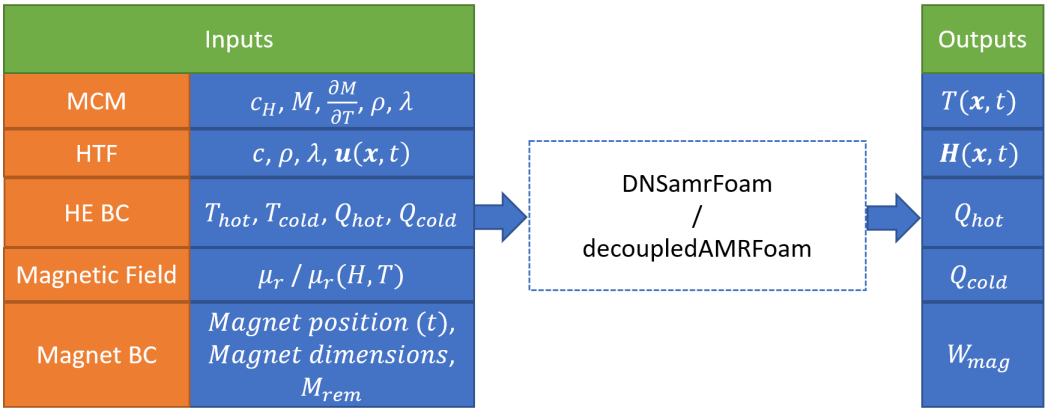

Figure 3.8 Inputs and outputs of DNSamrFoam and decoupledAMRFoam.

$$dw_{mag} = \mu_0 M dH \tag{3.16}$$

Constant values of ρ and λ are also necessary. It is possible to have different MCMs on the same MR by adding them through dedicated meshes. In decoupledAMRFoam, an extra dictionary is necessary to specify which H field file needs to be read. It suffices to specify a vector where its components express the amount of time that each H field file is going to act upon the regenerator. So, the sum of this vector components is the cycle period.

For the resolution of the magnetic field, the value of μ_r needs to be specified. When using DNSamrFoam a table is needed, but with decoupledAMRFoam a representative constant value of μ_r is sufficient. To precalculate the magnetic field for decoupledAMRFoam a separate magnetostatic solver, described in section 3.2.3, is needed. The boundary condition representing the moving magnet has two cross section shapes available: rectangular or circular. The dimensions of the magnetic poles are specified in a separate dictionary, along with other data that defines the position of the magnet during the cycle. The cells of the boundary patch that fall inside the specified magnet area at a particular time will have the remanence magnetization specified by the user $\frac{\partial \varphi}{\partial n} = M_{rem}$. The cells that are outside this area though, will have $\frac{\partial \varphi}{\partial n} = 0$ as a boundary condition. This is based on the hypothesis that the magnetic field is mostly straight from one pole to the other.

For the fluid domain, constant values of c, λ, and ρ need to be supplied. Similar to the reading of the magnetic field in decoupledAMRFoam, a vector with the time frames for each fluid flow file needs to be specified. The cyclical evolution of the fluid domain is taken as a reference to evaluate if the machine has achieved a steady state. So, if multiple HTFs are defined, a single simulation might handle multiple AMR cycles at once.

A boundary condition was developed to represent ideal heat exchangers at the inflow and outflow boundaries of the HTF. They have no dead volume and the mixture is considered perfect. Another separate dictionary specifies the operating conditions of the heat exchangers. In this file, fixed temperatures or heat loads can be specified, along with the initial temperatures of the heat exchangers. These linear initial temperatures can be used to set an initial gradient over the MCM and HTF domains. This initial guess of the temperature field is crucial to reduce the number of cycles needed to achieve steady state operation.

Finally, the last task of each time step is to calculate the integral values of the cooling load Q_{cold}, the rejected heat Q_{hot}, and the magnetic work W_{mag}. In the following sections, all of the spatial differential terms of Equations (3.3), (3.4), (3.5), (3.6), and (3.7) were represented by second order numerical schemes. The temporal differential terms though were set to use a second order implicit scheme.

3.2.4 Validation of the numerical model

The numerical solvers described in the last section are tested here. A preliminary validation is done for each of the subroutines representing the simulation of a physical phenomenon (subroutines that solve Equations (3.3), (3.4), (3.5), (3.6), and (3.7)). At the end of this section, a full AMR cycle is benchmarked to experimental measurements.

Flow field

To find out the validity of the meshes of Figure 3.4 to calculate the fluid flow through packed beds, the experiments performed by [32] are reproduced. After measuring the porosity for the packed beds of Figure 3.3, they proceeded to measure the fluid velocity profiles by Lase Doppler Velocimetry. The employed fluid had a kinematic viscosity of $8.44 \cdot 10^{-6}\ m^2 \cdot s^{-1}$. In the simpleFoam simulations, a parabolic velocity with a mean value of 4 $mm \cdot s^{-1}$ was set at the inlet, which was located at one end of the cylinders of the packed bed (see Figure 3.3). This inlet velocity corresponds to the lowest Re_p specified by [32] ($Re_p = 4$) . For the reminding cases, the kinematic viscosity was adjusted to match the desired Re_p at the inlet. Re_p is the Reynolds number for the characteristic length of particle diameters and cylinder lengths. The flow is hypothesized to have a laminar steady nature.

For each particle shape of [32], a Grid Sensitivity Analysis (GSA) was conducted at the highest Re_p (Figures 3.9, 3.10, 3.11, and 3.12). These figures represent the axial velocity component U normalized by the average inlet velocity U_m. The properties of the meshes

employed in the GSA can be found in Table 3.3 (at lower Re_p the medium size mesh was used). This is also true for the porosity of the packed beds (Figure 3.5).

The flow velocity profiles shown in Figures 3.9, 3.10, and 3.11 follow closely the experimental data obtained by [32]. On the case of the Raschig rings, the porosity of the mesh at the center of the packing is slightly overestimated (Figure 3.5). That causes slight discrepancies on the velocity profile, that fade when Re_p increases (Figure 3.12).

Figure 3.13 shows a close comparison of the velocity profiles at different Re_p for each packed bed. Consequently, for the low Re_p regimes studied here, a temperature dependence of viscosity (ν_{HTF}) will not change significantly the shape of the velocity profiles. This means that the temperature field will not act significantly upon convective heat transfer properties. So, the first possible coupling mechanism described in the introduction can be disregarded.

Magneto-Caloric Effect

The Mean Field Theory (MFT) has been the most employed model to describe the entropy state of MCMs in AMR models. In MFT, single atom magnetic dipoles are hypothesized to interact with the rest of the crystal through an effective field, which is proportional to the net magnetic moment of the crystal (see [84]). In the case of Gd though, MFT has some discrepancies with experimental adiabatic temperature change (ΔT_{ad}) of about $2K$ ([9]). With the objective of closely representing the behaviour of Gd, the approach presented by [55] is employed here. It uses tabulated magnetization data of Gd from [44] to calculate c_T (Equation 3.9).

Results of Figure 3.14 were computed with Equation 3.6 on an adiabatic cube that experienced a uniform magnetic field change from 0 to $2T$.

The density of Gd was taken to be $\rho_{MCM} = 7900\ kg \cdot m^{-3}$, and its thermal conductivity $\lambda_{MCM} = 10.5\ W \cdot m^{-1} \cdot K^{-1}$ ([48]).The specific heat at constant field (c_H) was extracted from [76]. It can be argued that using the separate sources of data to compute the MCE of Gd (one for c_H and another one for c_T) is base for some incoherence. However, the results seem to give a more accurate solution than the MFT. Thereby, due to the lack of information and resources to better characterize Gd, this approach is considered good enough for the purposes concerning this study.

Mesh Type	*Smallest cell size*	*Number of Cells*
Spheres Coarse	666 μm	0.943M
Spheres Medium	444 μm	5.34M
Spheres Fine	350 μm	9.41M
Def. spheres Coarse	458 μm	0.813M
Def. spheres Medium	305 μm	5.19M
Def. spheres Fine	240 μm	9.66M
Cylinders Coarse	458 μm	0.857M
Cylinders Medium	305 μm	6.32M
Cylinders Fine	240 μm	11.7M
Raschig rings Coarse	458 μm	1.65M
Raschig rings Medium	305 μm	7.67M
Raschig rings Fine	240 μm	12.9M

Table 3.3 Number and size of the cells used in the GSA of Figures 3.9, 3.10, 3.11, and 3.12. The packed beds were 150mm high and the meshes were unstructured.

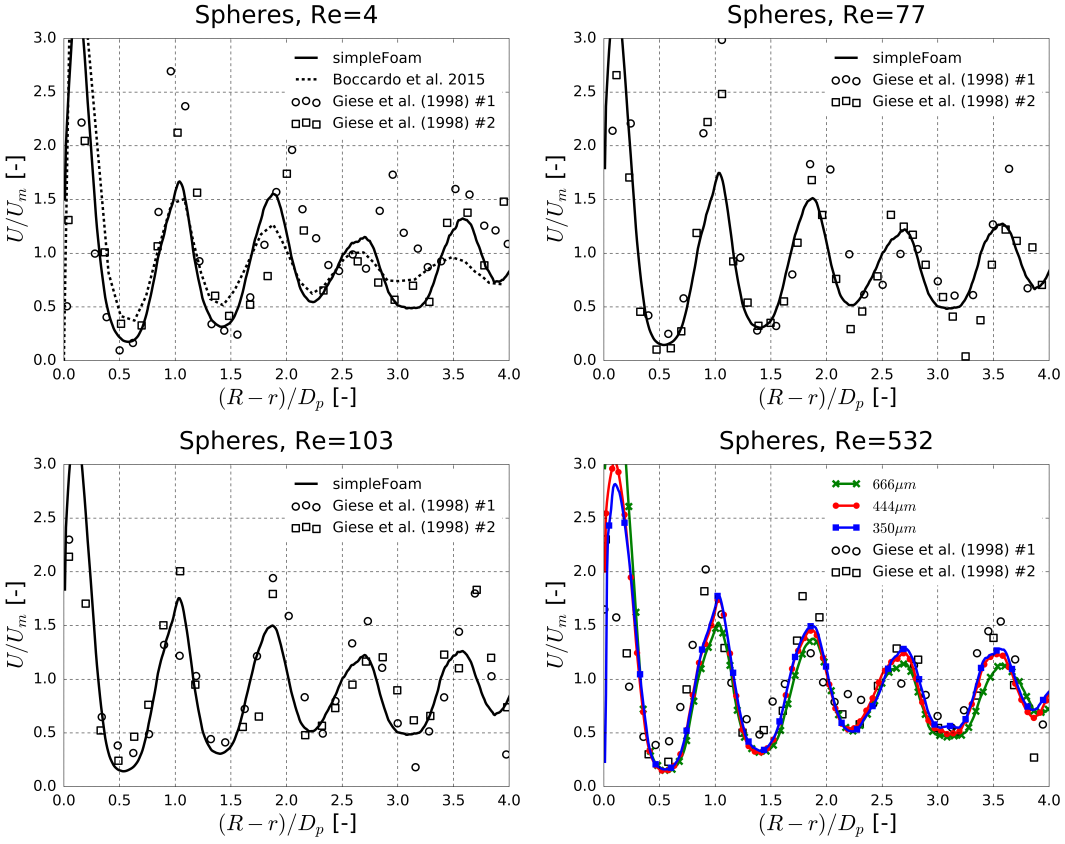

Figure 3.9 Radial distribution of the axial velocity for the sphere packed bed. Lines on the last graph represent different mesh refinements (see Table 3.3 for more information).

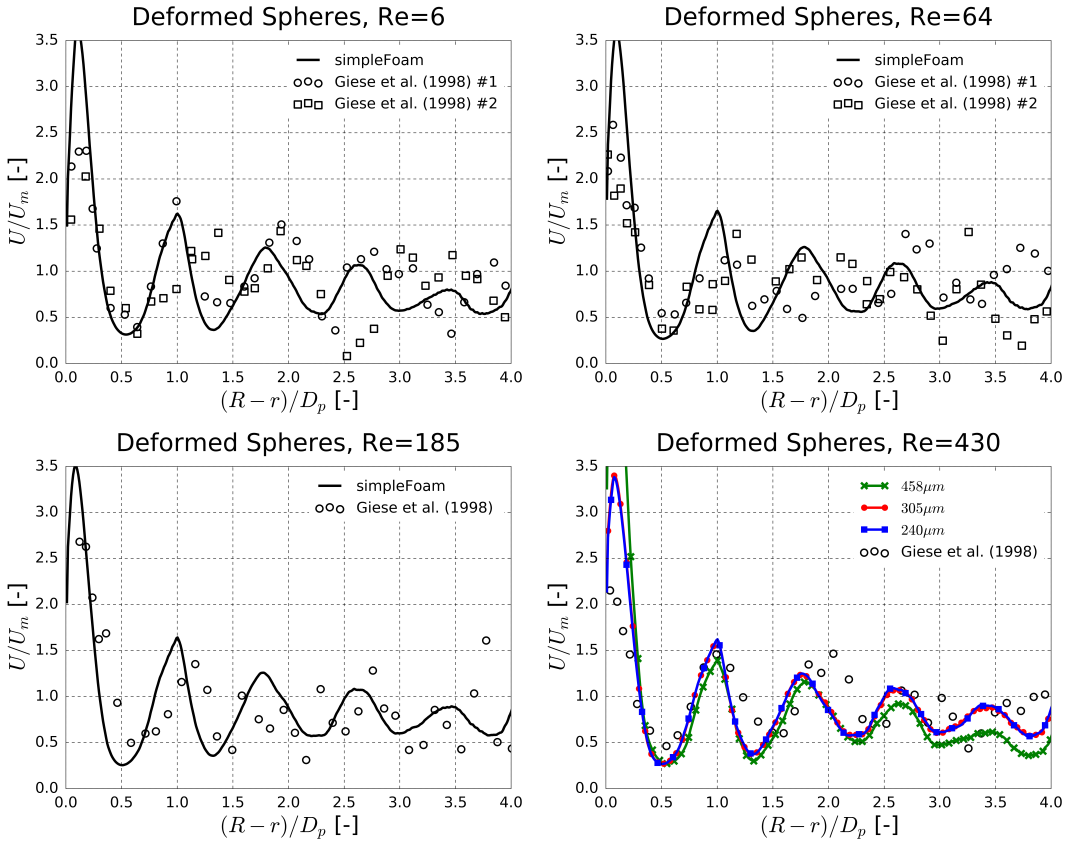

Figure 3.10 Radial distribution of the axial velocity for the deformed spheres packed bed. Lines on the last graph represent different mesh refinements (see Table 3.3 for more information).

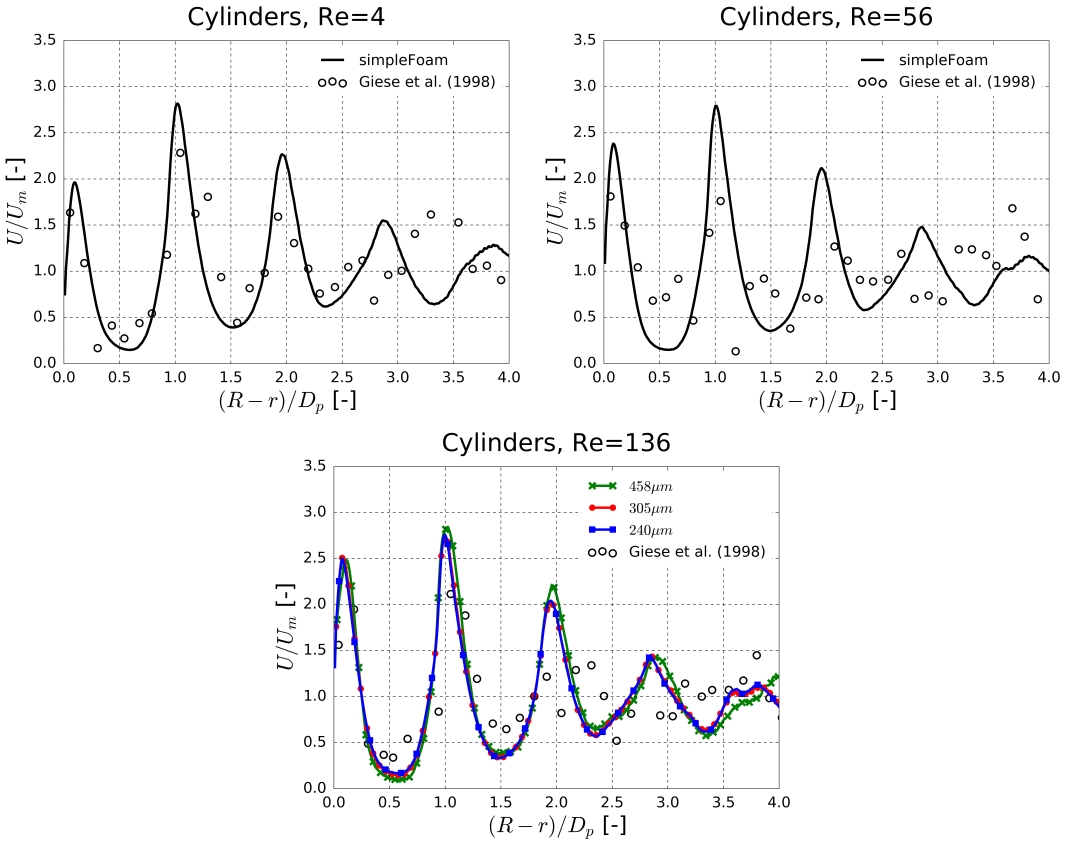

Figure 3.11 Radial distribution of the axial velocity for the cylinder packed bed. Lines on the last graph represent different mesh refinements, ordered by the smallest cell size size of the mesh (see Table 3.3 for more information).

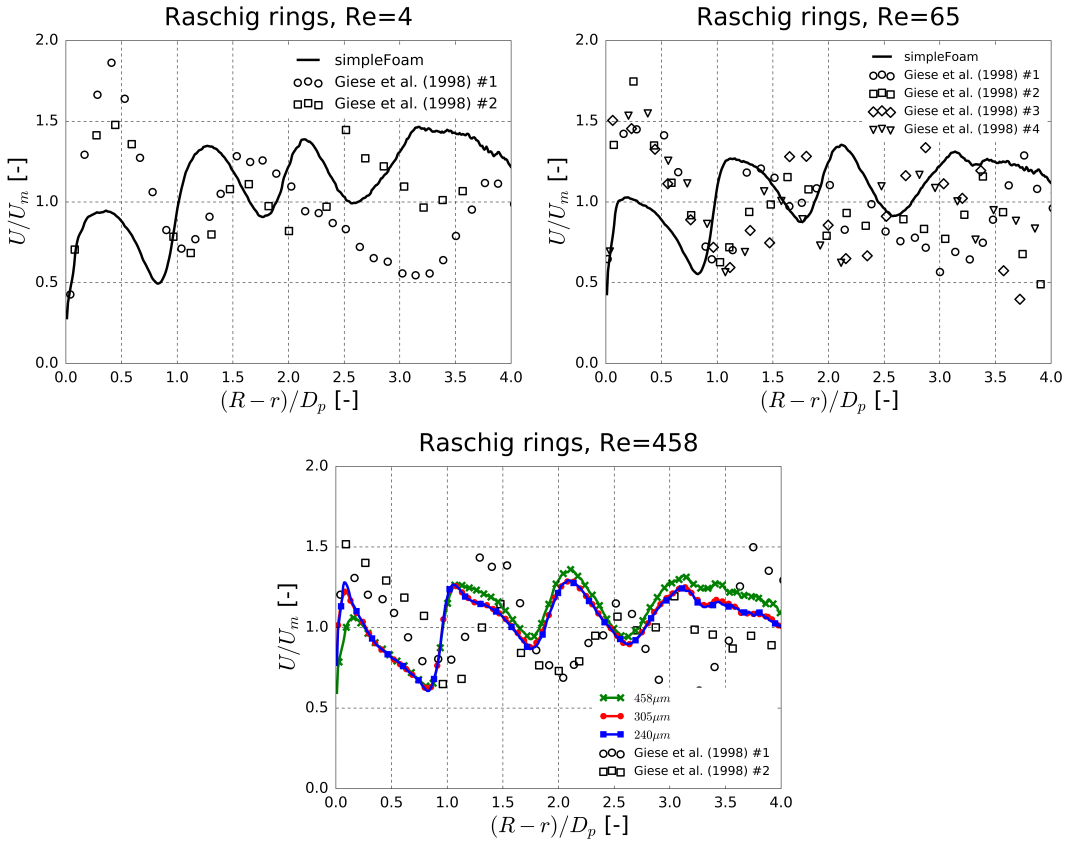

Figure 3.12 Radial distribution of the axial velocity for the Raschig ring packed bed. Lines on the last graph represent different mesh refinements, ordered by the smallest cell size size of the mesh (see Table 3.3 for more information).

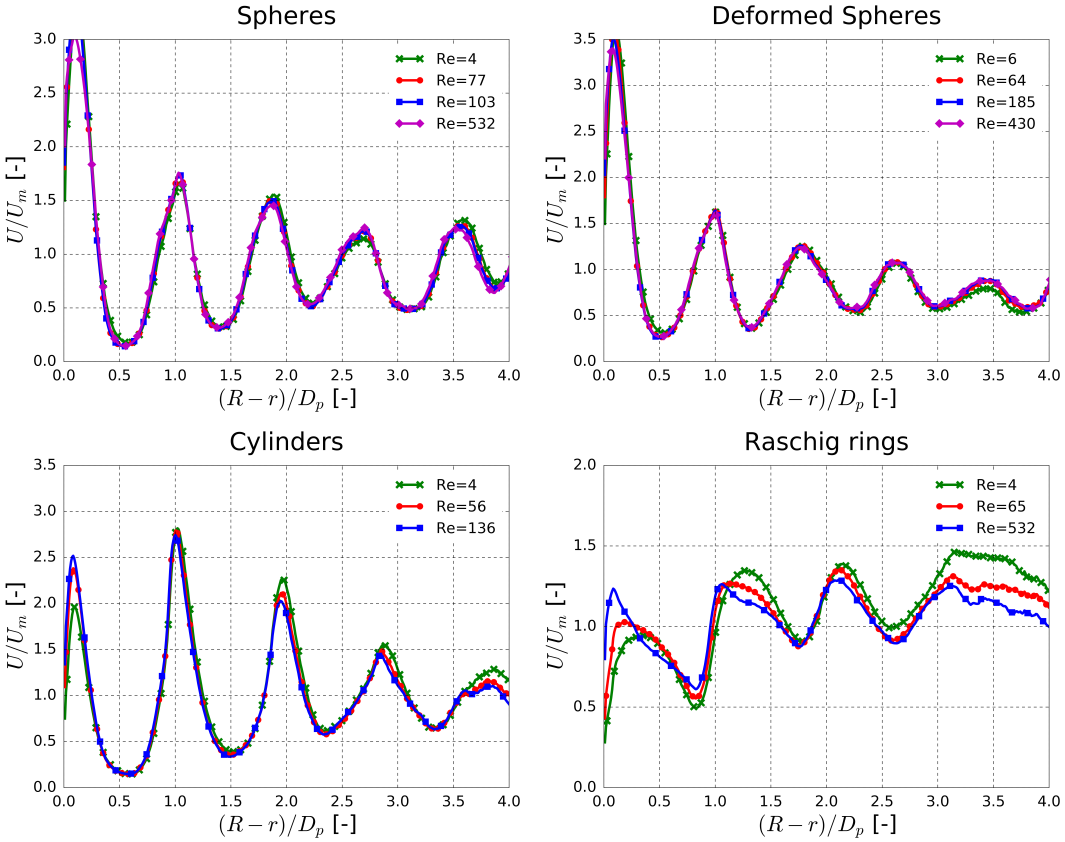

Figure 3.13 Radial distribution of the axial velocity when Re increases, for the geometries presented in figure 3.3.

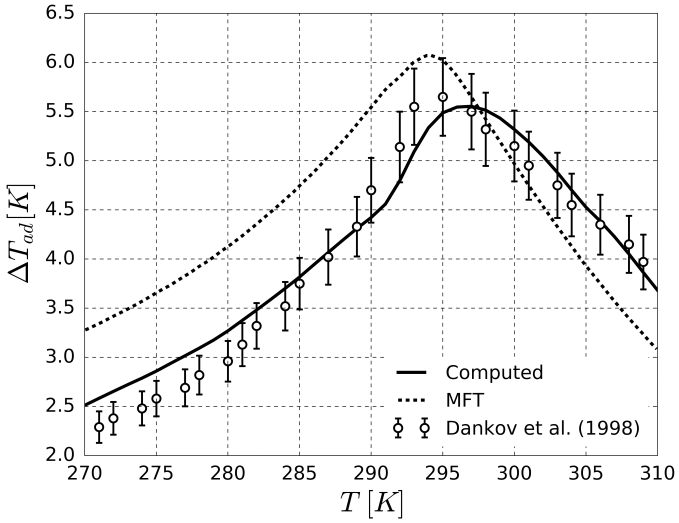

Figure 3.14 Comparison of the computed MCE, the results of MFT and experimental data from [23], for initial temperatures between 270K and 310K, when the magnetic field changes from 0 to $2T$.

Conjugate Heat Transfer

In order to validate the CHT solver, results were compared to the benchmark case of [75]. This benchmark consists on a 2D flow channel, where the inlet is raised a distance equal to the width of the inlet itself (see Figure 3.15). [75] solved this problem by directly calculating the stream function vorticity formulation of Equation 3.3 and 3.4, through a Boundary Element Method (BEM). This configuration (Backward-Facing Step) gives rise to two flow detachments. First, the one at the lower wall, starts at the inlet and goes until $x_1 = 12.2h$. Then the second one at the upper wall, goes from $x_2 = 9.7h$ to $x_3 = 20.96h$ ([31]). The lower wall of the channel is the interface between solid and fluid domains. The solid domain consists of a slab that is heated at a constant non dimensional temperature of $\theta = 1$ ($\theta = \frac{T - T_{inlet}}{T_{wall} - T_{inlet}}$) on the lowest side. The rest of the boundaries are adiabatic with the exception of the inlet flow, that is kept at $\theta = 0$. The intlet velocity was set to have a laminar parabolic profile with an average velocity of 1 $m \cdot s^{-1}$.

Before computing the benchmark cases, a GSA was conducted on the fluid and thermal solutions. The meshes were structured and uniform with square cells. The size of the cells is marked in Figures 3.16 and 3.17. Figure 3.16 shows how consecutive refinements lead to the same velocity solution, at the point where the velocity field is meant to have the highest gradient ([74]). The location of the flow detachments also matched the benchmark case.

Similarly, Figure 3.17 shows how consecutive mesh refinements approach to the same temperature solution given by [75]. This temperature gradient is extracted at $x = 6h$, and the ratio between thermal conductivities was the highest considered by [75]: $k = \frac{\lambda_{solid}}{\lambda_{fluid}} = 1000$.

Figure 3.18 shows the temperature field and the Nusselt number (Nu) at the fluid-solid interface for different cases of k. Overall, the computed solutions match very closely the data from [75].

Magnetic Field

To test the validity of the magnetostatic solver, the benchmark case explained by [99] is used. It consists on the magnet of Figure 3.19 with a homogeneous magnetization value of $8.7 \cdot 10^5$ $A \cdot m^{-1}$ along the longitudinal dimension of the rectangular prism. The relative magnetic permeability of the prism was $\mu_r = 1.07$. The solution of the magnetic field of this geometry can be analytically calculated by the Biot-Savart law (as explained by [99]).

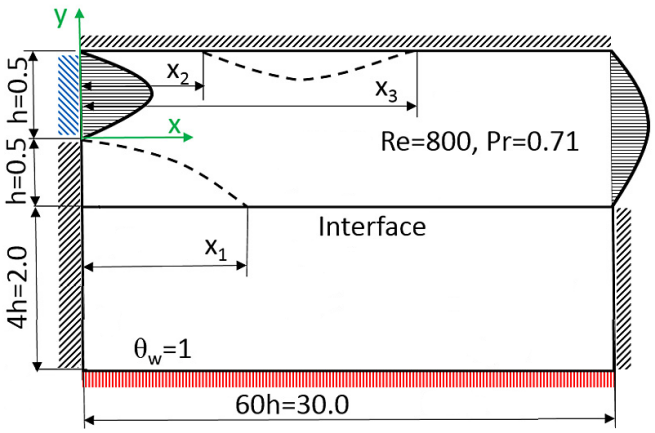

Figure 3.15 Description of the CHT benchmark case (modified schema from [75]).

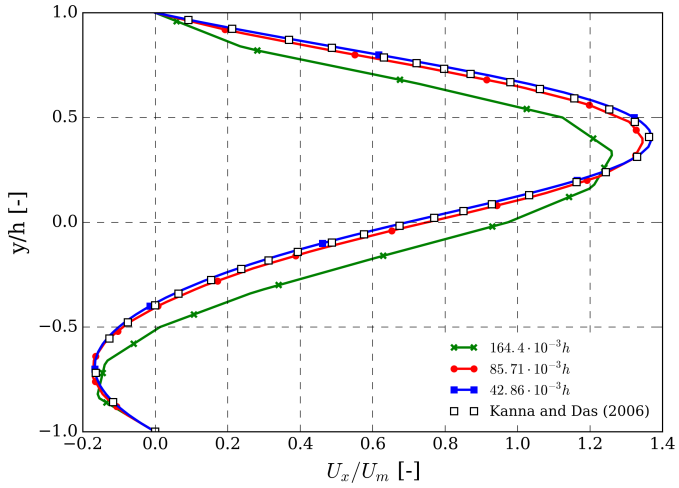

Figure 3.16 Velocity profiles of the BFS at $x/h = 6$. Lines represent different cell sizes. Results are compared to the DNS stream function vorticity solution provided by [74] with a 151x81 grid.

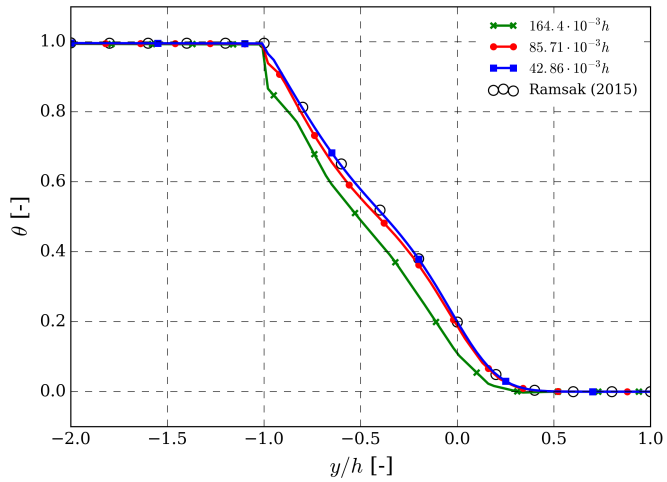

Figure 3.17 Temperature profile along the vertical direction at $x/h = 6$ for $k = 1000$. This is a comparison between the present results for different mesh grids and the numerical simulations of Ramsak (2015).

The case was solved in two different meshes, one for the magnetic prism and another one for the non-magnetic surrounding domain ($\mu_r = 1$). The far field boundary condition was taken to be $\frac{\partial \phi}{\partial n} = 0$. It was verified a posteriori, that the magnitude of $\mathbf{H}$ was negligible at the far field boundaries. Figure 3.20 shows how consecutive refinements of the surface mesh of the prism, lead to a better definition of the singular point located at the corner of the prism ($R = 14.14mm$).

As an extra verification, the shape demagnetization of a sphere was calculated under a uniform magnetic field. The shape demagnetization of an ellipsoid with homogeneous magnetization is constant (D) and it can be analytically obtained (see [54]). In the case of spheres, $D = \frac{1}{3}$. This value was attained with 95% accuracy after consecutive mesh refinements.

AMR cycle validation

The solver described in section 3.2.3, is here tested to replicate the results from the plate regenerator described by [6]. Packed bed regenerators were not employed in this validation, because of the very fine details of the regenerators available in the literature. The huge difference between the whole regenerator size and the individual particle size, demands meshes that are too big for the present computing facilities to handle (in the order of billion cells). So, first of all, a GSA is conducted in the plate regenerator to see which is an appropriate discretization of time and space. Figure 3.21 shows the chosen geometric origin for each spatial dimension. The plates are 0.9mm thick, 25mm wide and 40mm

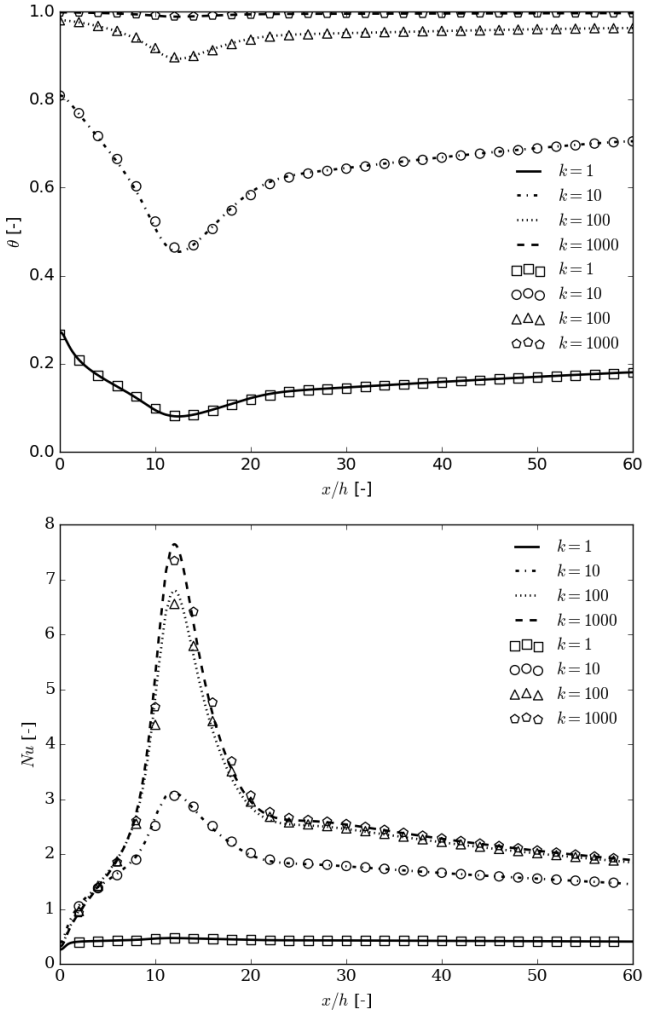

Figure 3.18 Temperature and Nu profiles at the fluid-solid interface of the benchmark presented in Figure 3.15. Markers represent data from [75] and lines the solution computed by the present solver.

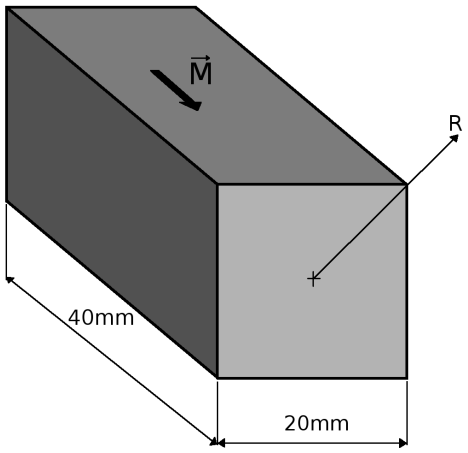

Figure 3.19 Dimensions of the magnet used in the validation case by [99]. The origin of the R direction is at the center of the square cross section.

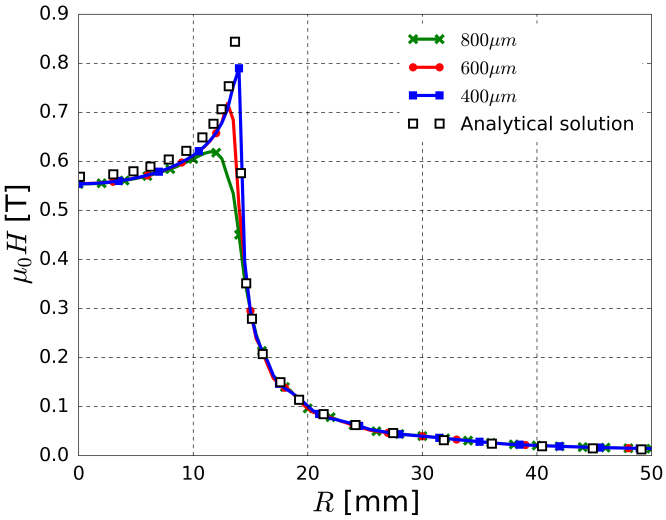

Figure 3.20 Magnetic field intensity on the surface of the prism of Figure 3.19. Lines represent results obtained for different values of the smallest cell size. The total size of the meshes are 0.1M, 0.378M, and 5.49M respectively.

long. The HTF channels bounded by the plates are 0.8mm thick, and 0.45mm thick on top and below the last plates.

The electromagnet described in [6] had circular pole caps of 76mm in diameter, and it was set so that at the center of the gap, the magnetic field was $\mu_0 H = 1\ T$ in the absence of the plates. It was then confirmed that the empty volume alocated to the regenerator experienced $0.97\ T$ due to the non uniformity of the magnetic field, as detailed by [6]. This was translated into an $M_{rem} = 9.434 \cdot 10^5\ A \cdot m^{-1}$ on the moving magnet boundary condition. The size of the magnet gap was not specified, so it was taken to be 40mm, the minimum possible value (exactly the diameter of the regenerator housing). The magnetic permeability of Gd was implemented through a table, constructed from magnetization measurements published by [44] and Equation 3.1. The magnetic far field on x and z directions was set far enough so that the calculated $\mu_0 H$ was less than $2 \cdot 10^{-3}$ T. Consecutive mesh refinements show how the solution converges at the edge of the middle plate when the magnetic field is set at the center of the stack (Figure 3.22). All the meshes are unstructured.

A simplified case was constructed to check the thermal field and fluid momentum GSA. It consisted on one of the plates described before, sandwiched by two 0.8 mm thick channels. For the fluid momentum GSA a velocity inlet of $16.67 mm \cdot s^{-1}$ was set, giving the parabolic laminar profile of Figure 3.23. This velocity corresponds to the maximum surge velocity employed in this study.

For the thermal field GSA, the domains were initialized with a temperature gradient that went from 285 to 310K in the x direction. At the inlet the fluid velocity was set so that the flow traveled 40% of the length in 3s, with a temperature of 280K. Figure 3.24 shows the temperature change after 3s, relative to the initial gradient. Once again, consecutive refinements converge into a single solution.

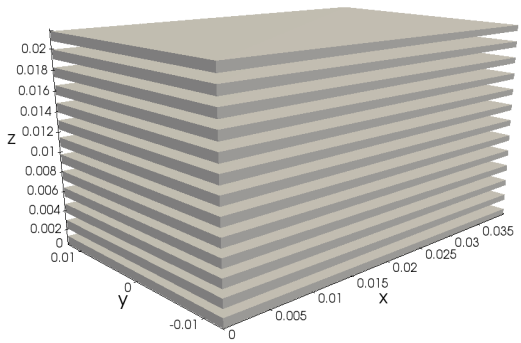

Figure 3.21 Geometry of the regenerator constructed by [6].

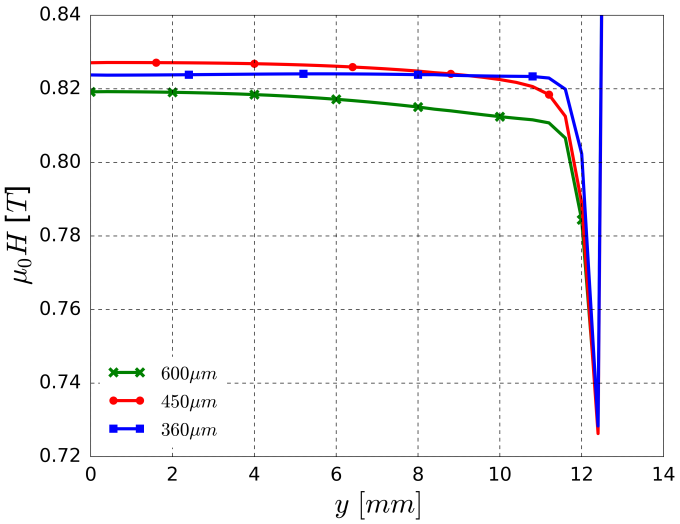

Figure 3.22 Magnetic field over a horizontal line at the center of the stack (x=20mm and z=11.05mm) of Figure 3.21. Lines on the graph represent different mesh refinements, ordered by the smallest cell size of the mesh.

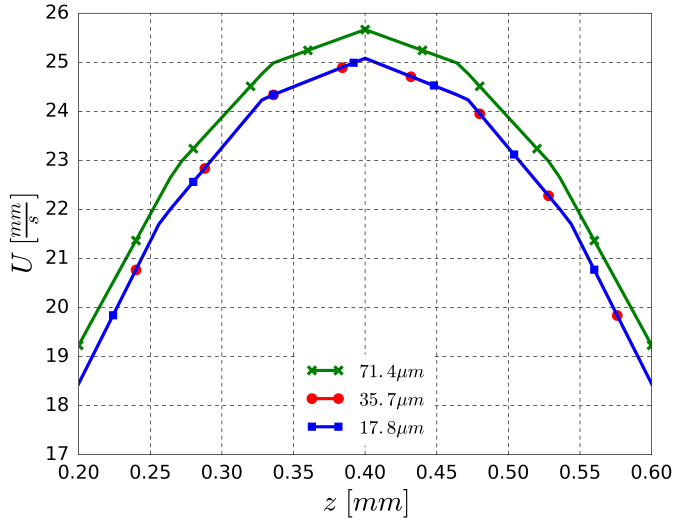

Figure 3.23 Velocity profile at the center of a channel described in Figure 3.21 when the mean inlet fluid velocity is set to $16.67mm \cdot s^{-1}$. Lines on the graph represent different mesh refinements, ordered by the smallest cell size of the mesh.

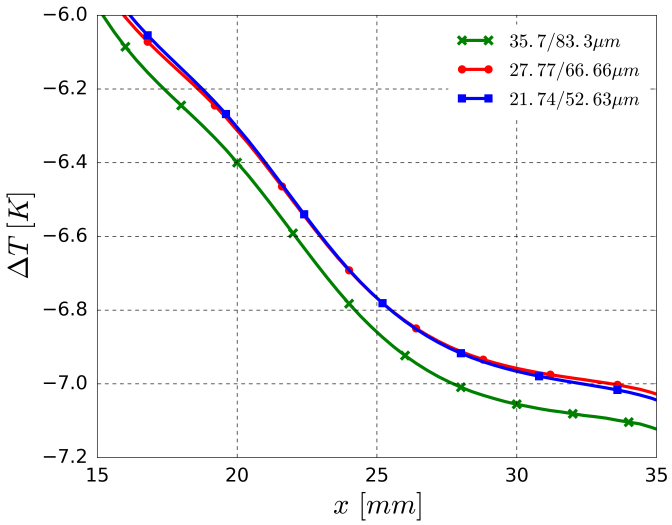

Figure 3.24 Streamwise distribution of the temperature change at the center of the plate ($y = 0$ and $z = 11.05mm$). Lines on the graph represent different mesh refinements, ordered by the smallest cell size of the HTF/MCM meshes.

The time step of the GSA cases of Figure 3.24 was set to $0.05s$. Figure 3.25 shows the influence of the time step on the case described earlier.

From Figures 3.22, 3.23 and 3.24, it is concluded that the temperature field sets the minimum cell size for the calculation of the AMR cycle. Thus, the meshes with a cell size of $27.77\mu m$ and $66.6\mu m$ were used in the AMR cycle simulations, for the HTF and MCM domains respectively. With this space discretization, Figure 3.25 shows how the numerical solution changes considerably for time steps larger than 0.05s. The final mesh sizes of all the domains in the AMR cycle simulation can be found in Table 3.4.

So, in order to choose between DNSamrFoam and decoupledAMRFoam, and clear the importance of the coupling between magnetic and thermal fields, a magnetization step described in [6] is calculated with each solver. The magnetization step is 3s in duration. The position of the magnet over time was made sinusoidal (when the magnet is being dis-

Domain	*Smallest cell size*	*Number of cells*
MCM	$66.6\mu m$	2.18M
HTF	$27.77\mu m$	1.84M
Non-magnetic Surroundings	$66.6\mu m$	2.57M

Table 3.4 Final size of the meshes used for the AMR cycle simulation of the regenerator built by [6].

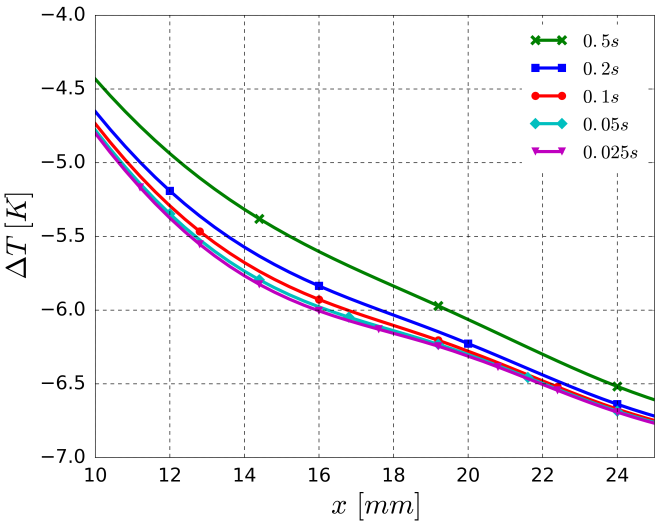

Figure 3.25 Streamwise distribution of the temperature change at the center of the plate ($y = 0$ and $z = 11.05mm$). Lines represent different time step sizes.

placed) to represent the constant acceleration of the linear relative motion of the magnet. The computational domain was initialized with a linear gradient that extended from 280 to 310K in the x direction. Also, the thermal conductivity of the MCM was set to zero not to blur by thermal diffusion the differences between coupled and uncoupled solutions. If the thermal diffusion term was included, not only the initial temperature gradient would partially fade, but the differences in ΔT_{ad} (caused by different starting temperatures), would be influenced by neighboring points. In the case of decoupledAMRFoam an average value for μ_r was calculated from 0 to $1T$ and from 280 to 310K. The result was $\mu_r = 2.1$.

Figure 3.26 shows the absolute difference between the temperature profiles (averaged in the y and z directions) after the demagnetization step computed by DNSamrFoam and decoupledAMRFoam. The maximum difference is near x=30mm with and initial temperature of 302.5K. This difference manifests at higher temperatures, where Figure 3.1 shows how μ_r is closer to 1.5, than 2.1.

Nonetheless, the maximum difference is about 0.25K, which is less than the expected accuracy from the MCE (Figure 3.14). Thus, decoupledAMRFoam is chosen to simulate the experimental set up of [6]. This will notably reduce the computational load, as the only phenomena to solve at run time is the temperature field.

Figure 3.27 shows the evolution of the temperature difference between both ends of the regenerator when increasing the fluid displacement of the surges. [6] kept the cold side adiabatically insulated, and the hot side exposed to room temperature (298K). Since the

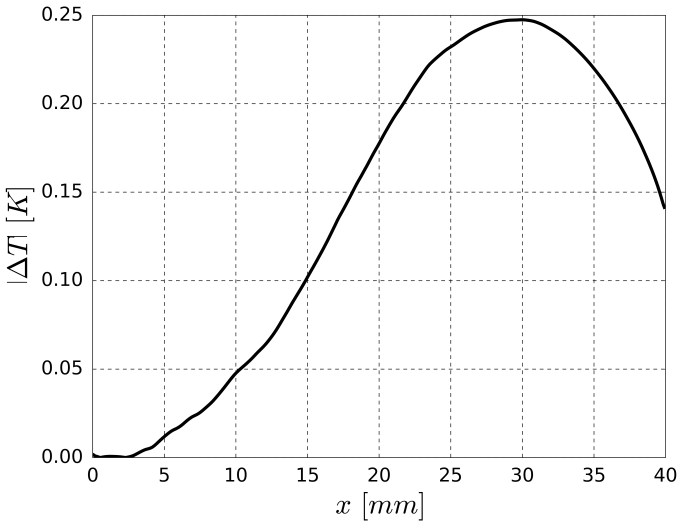

Figure 3.26 Absolute difference of the temperature profiles (averaged in y and z) calculated with DNSamrFoam and decoupledAMRFoam, after a magnetization step of the regenerator built by [6]. The initial temperature gradient was linear along x and went from 280 to 310K.

temperature at the hot end was not actively controlled, a higher than room temperature is expected at the hot end. Figure 3.29 shows how the hot side was measured around 300K. So, a constant temperature of 300K was set at the hot end of the simulations. In the cases calculated here, HTF exchanger boundaries are located right at the end of the plates.

All in all, the results from decoupledAMRFoam follow very closely the measurements made by [6]. Their 2D solver though (see [70] in Table 3.1), overestimated ΔT_{reg} by 3-4K. [6] argued that the difference in results could be associated to three simplified phenomena: differences on the real and calculated MCE, the magnetic field, and heat losses. In this study, no heat losses were taken into account except from the heat that leaves the hot end to maintain a constant temperature at the hot sink. Thus, the differences between simulations must be associated to the calculated MCE and internal magnetic field (see the phenomena in Table 3.1). Figure 3.14 shows that MFT discrepancies are about 0.5K for $2T$ between 295-300K. Thus, the difference between the computed results in Figure 3.27 might be a consequence of the direct numerical simulation of the internal magnetic field. [6] hypothesized an instantaneous and homogeneous internal field without shape demagnetization due to the parallel plate arrangement to the applied magnetic field. However, the calculated average internal field by the present magnetosatic solver of the plate stack was $0.778T$ when the regenerator was fully magnetized. As mentioned earlier, [79] and [11] have already pointed out that groups of similar geometric shapes have higher shape demagnetizations than their stand alone cases. The simulations carried out in this

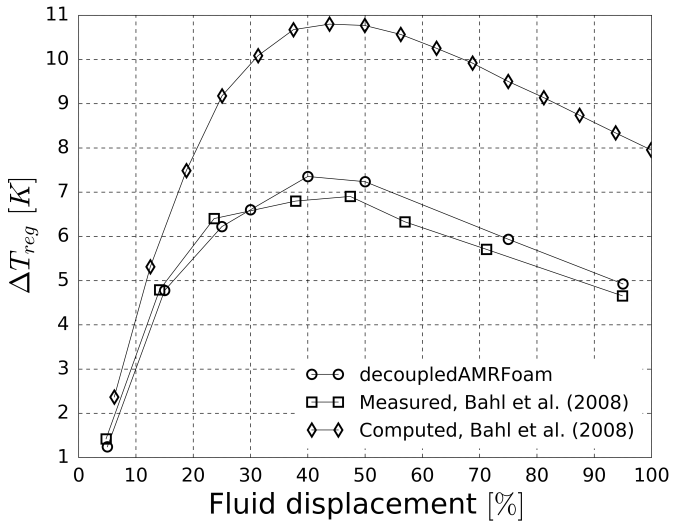

Figure 3.27 Evolution of the temperature span of the plate regenerator built by [6], as the fluid displacement of the surges increases. The fluid displacement shown in this figure is relative to the length of the regenerator.

study indicate that the increased demagnetization of the stack can affect substantially the solution of the temperature field in MR. Also, the spatial heterogeneities of the applied field might influence the temperature field of the regenerator. These are comprised of a the bell shaped applied magnetic field, and the gradual application of the magnetic field as the it moves along the x axis.

Similar results were produced when varying the timing ratio $\tau = \frac{t_{mag}}{t_{surge}}$. The ratio τ was increased by adding some idle time between magnetization phases, where the HTF is at rest. DecoupledAmrFoam predicted a temperature span close to the experimental results (see Figure 3.27). The biggest discrepancy is about 1K at $\tau = 4$. It seems that the difference between the computed and experimental results increases with the τ ratio. This seems logical, as the HTF is at rest more time when τ rises. This means that the fluid portion that goes into the hot and cold ends is there, at rest, for a longer time, increasing the heat losses that were not modeled.

For the case of $\tau = 0.5$, where the discrepancies in ΔT_{reg} are minimum, Figure 3.29 shows the temperature gradient in the regenerator. The differences between the measured and computed results are minimal.

3.2.5 Parallelization of the solver

After a thorough validation of the AMR cycle solver, the parallel speed up is presented in this section to give the user an idea of the computational resources needed to run a

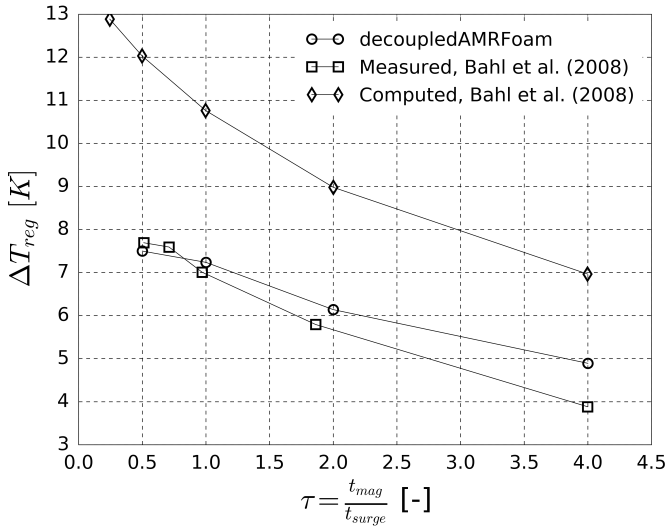

Figure 3.28 Evolution of the temperature span of the regenerator built by [6], when the time ratio $\tau = \frac{t_{mag}}{t_{surge}}$ is increased.

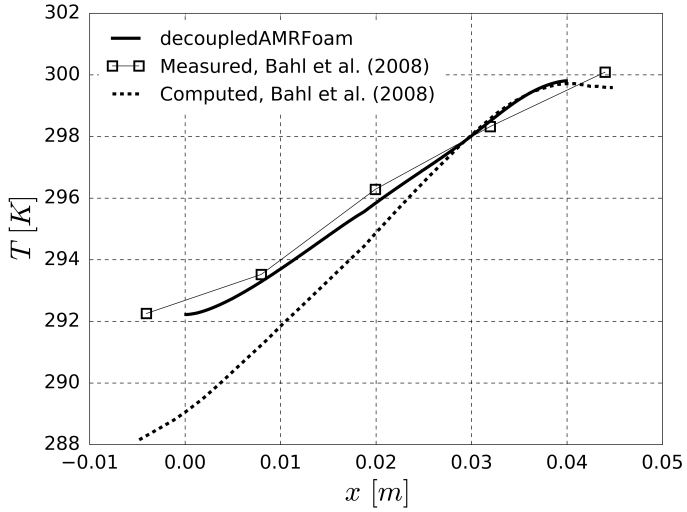

Figure 3.29 Temperature profile of the regenerator built by [6], at 50% fluid displacement and $\tau = 0.5$.

given case. The parallelization of the solver is already implemented in the OpenFOAM framework. The native application "decomposePar" splits the mesh into as many parts as wanted. "Metis" decomposition method is available too (see [38]). Once the mesh is partitioned, the size of the linear matrices that each CPU needs to solve is reduced. Figure 3.30 shows the evolution of the speed up (Equation 3.17) and efficiency (Equation 3.18) for a single cycle of the parallel plate regenerator and the "Geometric Agglomerated Algebraic Multigrid" linear matrix solver:

$$S = \frac{t_{serial}}{t_{parallel}} \tag{3.17}$$

$$E = \frac{t_{serial}}{t_{parallel} \cdot n_{proc}} \tag{3.18}$$

The ideal speed up is equal to the number of processors. The efficiency of parallelization is the contribution of each processor to the speed up. The processor model brand was AMD Opteron 6172, with a frequency of 2.1 GHz, and 32GB of memory per node. Each node is composed of 24 CPUs, located at the facilities of Calcul Québec.

The speed up in Figure 3.30 starts to show an asymptotic tendency around 300 processors. For larger meshes, the asymptotic limit should in principle come for a larger number of CPUs. Also, there is a sharp change in the evolution of the efficiency at 24 processors. This is the number of processors that a node of the employed computing cluster holds. Every time a node is added, 32GB of RAM are added, reducing the sharp drop in efficiency of the first parallel computations. Figure 3.31 shows the wall time dependency of the number of processors for a single cycle of the parallel plate regenerator. This graph could be used to guess the computational time required by a given case. However, the time needed to reach steady state will highly depend on the initial guess of the temperature gradient in the regenerator.

3.2.6 Conclusion

This study lays out and validates a procedure to directly simulate in detail Active Magnetocaloric Regenerative cycles (AMR). First, it explains how to generate the geometry of randomly packed beds. These are the most popular regenerator geometries of the published prototypes. Then, a multiphysics solver used to compute all the physical fields involving an AMR cycle is described and thoroughly validated. This is done in two ways, first by separately analyzing the constituent phenomena, and then as a whole, by simu-

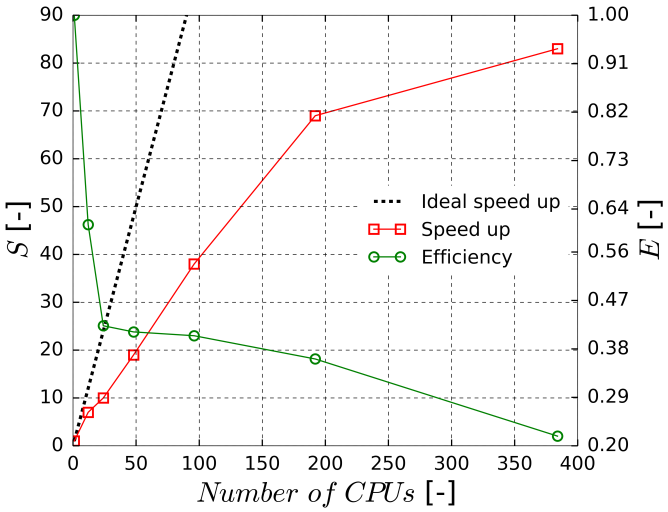

Figure 3.30 Speed up and efficiency of the parallel execution of decoupledAMRFoam for a single cycle of the regenerator built by [6].

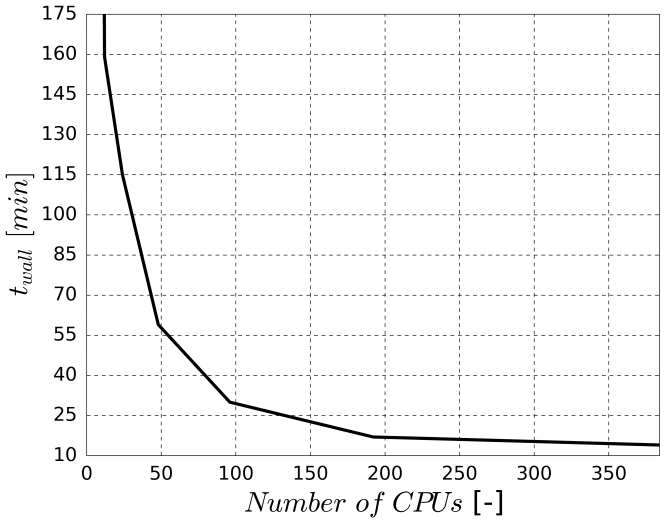

Figure 3.31 Wall time (or elapsed real time) of the parallel execution of decoupledAMRFoam for a single cycle of the regenerator built by [6].

lating a measured prototype ([6]). All the results show close agreement to the benchmark cases and measurements.

Along with the validation of an AMR cycle solver, two possible coupling mechanisms have been studied. First the temperature dependency of Heat Transfer Fluids like water, which changes substantially its kinematic viscosity in the temperature range of a typical AMR cycle (270-310K). It has been shown that for low Reynolds numbers, the velocity profiles do not change in shape considerably, and thus the convective heat transfer properties of Magnetic Regenerators (MR) stay unchanged. The second coupling mechanism was the influence of the magnetization of the Magneto-Caloric Material (MCM), on the resultant magnetic field in the MR. The conclusion was that for MCMs like Gd, it is safe to assume a constant mangetic permeability (μ_r) in the calculus of the magnetic field. These conclusions allow for the separate calculus of the fluid velocity, magnetic field, and temperature fields, which saves a substantial amount of computational resources during run time. The functionality of the solver presented here is centered in the conceptual design of MRs. It allows the user to obtain very detailed information on radically new regenerator geometries and cycle configurations. Once the characteristics of the regenerator are decided, this solver could be used to obtain critical parameters for a 1D AMR cycle solver, such as the Nusselt number (Nu) and the average internal magnetic field. Another positive aspect of the solver is that by changing the source term in the MCM energy equation, it can be easily adapted to perform thermoelastic, electrocaloric, barocaloric or similar alternative cycles.

3.2.7 Acknowledgments

This work is part of the NSERC chair on industrial energy efficiency established at Université de Sherbrooke in 2014 with the support of Hydro-Québec, Ressources Naturelles Canada (Canmet ÉNERGIE-Varennes) and Rio Tinto Alcan that are gratefully acknowledged for their financial support.

3.2.8 Nomenclature

B	Magnetic field flux	$[T]$
c	Specific heat capacity	$[J \cdot m^{-3} \cdot K^{-1}]$
D	Shape demagnetization	$[-]$
g	Gravity	$[m \cdot s^{-2}]$
Gd	Gadolinium	
H	Magnetic field intensity	$[A \cdot m^{-1}]$
M	Magnetization	$[A \cdot m^{-1}]$
$\mathbf{n}$	Normal vector	$[-]$
Nu	Nusselt number	$[-]$
p	Pressure	$[Pa]$
Pr	Prandtl number	$[-]$
q	Specific heat	$[J \cdot m^{-3}]$
Q	Heat power	$[W]$
Re	Reynolds number	$[-]$
Ri	Richardson number	$[-]$
T	Temperature	$[K]$
$\mathbf{u}$	Velocity field	$[m \cdot s^{-1}]$
U	Axial component of velocity	$[m \cdot s^{-1}]$
W	Work power	$[W]$

Greek symbols

β	Thermal expansion	$[K^{-1}]$
ε	Porosity	$[-]$
φ	Magnetic potential	$[A]$
λ	Thermal conductivityl	$[W \cdot m^{-1} \cdot K^{-1}]$
μ	Magnetic permeability	$[-]$
ν	Kinematic viscosity	$[m^2 \cdot s^{-1}]$
ρ	Density	$[kg \cdot m^{-3}]$

Subscripts

0	Vacuum
ad	Adiabatic
app	Applied
B	Boundary
C	Curie
f	Fluid
H	Constant magnetic field
int	Internal
m	Mean value
mag	Magnetic
p	Particle
reg	Regenerator
rem	Remanent
s	Solid
T	Constant temperature

Acronyms

AMR	Active Magnetocaloric Regenerative
BC	Boundary Condition
BFS	Backward-Facing Step
CHT	Conjugate Heat Transfer
CPU	Central Processing Unit
DNS	Direct Numerical Simulation
FVM	Finite Volume Method
GSA	Grid Sensitivity Analysis
HE	Heat Exchanger
HTF	Heat Transfer Fluid
MCE	Magneto Caloric Effect
MCM	Magneto Caloric Material
MFT	Mean Field Theory
MR	Magnetic Regenerator
RAM	Random Access Memory
SIMPLE	Semi-Implicit Method for Pressure Linked Equations

CHAPTER 4

Direct numerical simulations of rotatory active magnetic regenerators: influence of the pin geometry

4.1 Avant-propos

Auteurs et affiliations:

1. Ibai Mugica: étudiant au doctorat*
2. Sébastien Poncet: professeur*
3. Jonathan Bouchard: chercheur**

*Université de Sherbrooke, Faculté de génie, Département de génie mécanique.
**Laboratoire des Technologies de l'Énergie, Hydro-Québec, Shawinigan.

Date d'acceptation:

État de l'acceptation: Submitted

Revue: Applied Thermal Engineering

Titre français: Simulations numériques directes de régénérateurs magnétiques actifs rotatoires: influence de la géométrie des bâtonnets.

Contribution au document: Cet article contribue à la thèse en explorant en profondeur l'influence de la géométrie du régénérateur sur ses performances.

Résumé français: Le document suivant examine, par des simulations numériques directes, différentes configurations possibles de la géométrie des bâtonnets pour les régénérateurs magnétocaloriques rotatoires. L'analyse est d'abord effectuée en caractérisant les performances de chaque géométrie par rapport aux multiples phénomènes physiques qui se produisent dans un régénérateur magnétocalorique: champs magnétiques, hydrodynamique et transferts thermiques. Ensuite, des cycles complets AMR 3D sont simulés pour un groupe sélectionné de géométries de bâtonnets et des conclusions sont tirées entre la plage de température des régénérateurs et les phénomènes physiques analysés séparément. La principale nouveauté de cette étude est l'analyse d'un nouveau paramètre géométrique pour les régénérateurs magnétocaloriques: la

tortuosité de l'écoulement du fluide. La conclusion principale est qu'une augmentation de la tortuosité pourrait être une bonne stratégie pour augmenter la puissance des régénérateurs magnétocaloriques.

Connection with previous chapter: This chapter exploits the validated 3D solver presented in the last chapter to investigate the influence of the geometry on AMRs. The validity of the results obtained in this chapter rely on the thorough validation of the 3D solver done before.

4.2 Direct numerical simulations of rotatory active magnetic regenerators: influence of the pin geometry

The following paper examinates through direct numerical simulations, different possible configurations of pin geometries for rotatory magnetocaloric regenerators. The analysis is first done by characterizing the performance of each geometry against the multiple physical phenomena that occur in a magnetocaloric regenerator: magnetic, fluid and thermal fields. Then full 3D AMR cycles are simulated for a selected group of pin geometries, and conclusions are drawn between the temperature span of the regenerators and the separately analyzed physical phenomena. The main novelty of this study is the analysis of the tortuosity of the fluid flow, a characteristic parameter of packed beds. The main conclusion is that an increased tortuosity might be a good strategy to increase the power of magnetocaloric regenerators.

4.2.1 Introduction

Current commercial refrigeration systems exploit a liquid-gas phase transition to transport heat from one place to another (by latent heat more specifically). This "vapor-compression" cycles have provided so far, the refrigeration needs for the general population worldwide. Within the research field of refrigeration machines, new alternative technologies seek to overcome the drawbacks of current vapor-compression technology by exploiting a different thermodynamic phase transition. The use of alternative refrigeration technologies could mean amongst others: the reduction of polluting refrigerants (halogen fluid blends eg. HFCs, CFCs, HCFCs), reduced noise levels due to the absence of compression/expansion stages, and an increase in energy efficiency due to a more isentropic phase transition and thermodynamic cycle. One of the most researched and promising alternative refrigeration technologies is magnetocaloric refrigeration (see [33]).

Magnetocaloric cycles use the magnetic phase transition of solid-state refrigerants to transport heat. Much like the liquid-gas phase transition, the ferro-paramagnetic phase transition provides a sudden change of the thermodynamic properties of the refrigerant (see [84]), which can be exploited into a cycle to transport heat. In the vicinity of its transition temperature (Curie temperature T_C), a paramagnetic material can be externally magnetized to become ferromagnetic again. In the ferromagnetic state, an increased amount of molecular magnetic dipole moments are aligned with the external magnetic field, so the magnetic entropy of the solid refrigerant decreases (there are some exceptions, see [43]). The excess entropy is released in the form of heat (or thermal entropy, see Equation 4.1). This happens *vice versa*, so if the Magneto-Caloric Material (MCM) is demagnetized adiabatically around T_C, it would cool down.

$$s_{total}(H,T) = s_{magnetic}(H,T) + s_{thermal}(T) \tag{4.1}$$

Magnetocaloric refrigerators are composed of at least the following parts: a magnet (permanent or electrically powered), a porous regenerator made of MCM, a system that pumps the Heat Transfer Fluid (HTF), and the heat exchangers at the thermal sink and source (see Figure 4.1). Most published prototypes try to follow a Brayton-like thermodynamic cycle (see Figure 4.1): 1. Fast (quasi-adiabatic) magnetization of the regenerator 2. Surge of the HTF from the cold source to the hot sink 3. Fast demagnetization of the regenerator 4. Surge of the HTF from the hot sink to the cold source. The reader is referred to [39] for a more exhaustive explanation of the magnetocaloric cycles.

First room temperature magnetocaloric refrigerators used an electromagnet to magnetize the regenerator and they operated at low frequencies. Later on, the electromagnets were substituted by permanent magnets that do not require as much input power to induce the (de)magnetization steps. Two main types of magnetic refrigerators have been built, linear and rotatory (see [107] for an exhaustive review). Linear refrigerators are simpler to build, but are less efficient and they are limited by a lower frequency of operation due to the considerable inertia of the moving parts. [8] demonstrated how the power input of these linear regenerators can be substantially reduced by the use of a twin regenerator that is π out of phase in the thermodynamic cycle. This configuration considerably reduces the magnetic forces that come from (de)magnetizing the regenerator (see Equation 4.2).

$$\mathbf{F}_{dipole} = \int (\mathbf{M} \cdot \nabla)\mathbf{B} dV \tag{4.2}$$

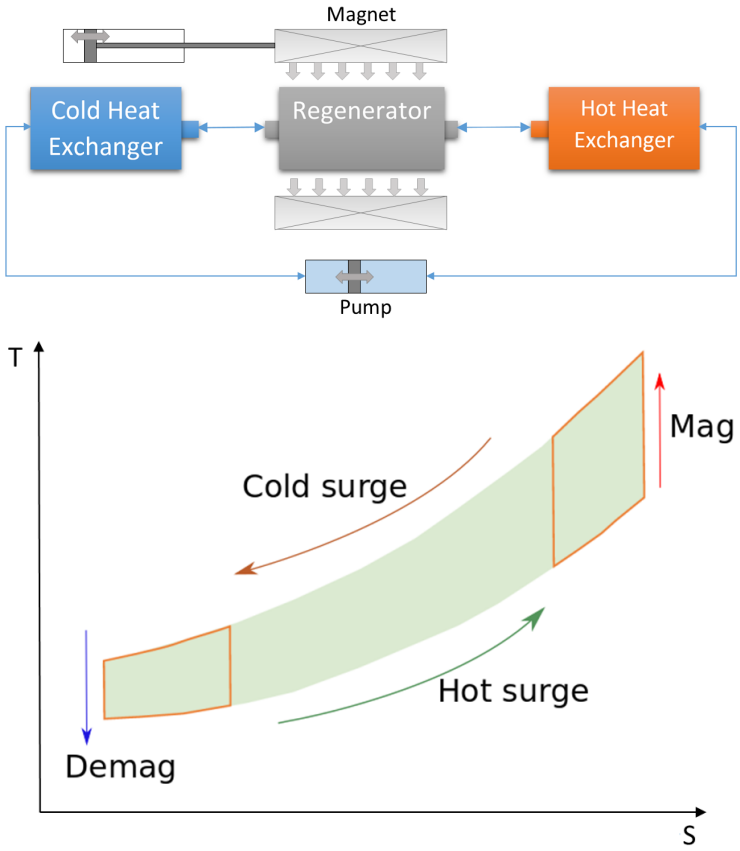

Figure 4.1 Up, schematic representation of a magnetic refrigerator. Down, Brayton-like thermodynamic cycle of an Active Magnetic Regenerator (AMR).

Most modern and performant magnetic refrigerators make use of a rotatory configuration. Rotatory configurations work by spinning either the permanent magnet or the regenerator bed to create a sinusoidal magnetic field that crosses the regenerator volume. The inertia of the wheel helps maintaining a constant relative movement of the magnetic field. This evens out the higher frequency torque that comes from the magnetization variations of the MCM. Each time a regenerator enters the external magnetic field, it gradually becomes ferromagnetic. So, regenerator and magnet pull towards each other by the force of their own magnetic dipoles. The regenerator gives mechanical work for lowering the magnetic entropy of the MCM. When the regenerator leaves the external magnetic field, mechanical work needs to be exerted to pull the regenerator out of the magnetized volume. The difference of mechanical work between the (de)magnetization phases, is the work done by the Magneto-Caloric Effect (MCE). So, if the regenerators come in twins, located π out of phase, the input work can ideally be reduced to the work done by the MCE (if the MCM does not suffer greatly from hysteresis or Joule effects). Numerous regenerators along the circumference provide a more continuous refrigeration power. However, they require a careful operation of the valve system. Good examples of this kind of machines are the prototypes published by [108] and [29] .

The most common regenerator geometries are made of parallel plates or packed particle beds. Parallel plates offer lower pressure drops than packed beds but have a lower cooling power because of the slower heat transfer between the MCM and the HTF. Over the recent years, several experiments have investigated the influence of the regenerator geometry on the performance of the AMR cycle.

[26] ran passive regenerator cycles (no applied magnetic field) with controlled heat sink and source to measure steady state temperature spans. The regenerators were made of flat, corrugated and dimpled plates. Corrugated plates were made by pressing flat plates onto cylinders. In a similar way, the dimpled plates were fabricated by pressing a flat plate onto spheres. Both dimpled and corrugated plates presented higher temperature spans than flat plates.

Similarly, [101] tested various passive regenerator geometries. They compared the pressure drop and heat transfer coefficients of various types of corrugated plates, flat plates and a packed bed. The latter showed higher heat transfer and pressure losses than the rest, but the lowest COP.

[3] continued investigating packed bed AMR cycles through 1D numerical modeling, more specifically, the aspect ratio of the whole regenerator volume. They concluded that longer and narrower regenerators suffer less from conduction losses, and more from viscous losses.

[60] extensively mapped the temperature span and available cooling power of plate regenerators with the help of a 2D numerical model. For all the tested frequencies and utilization ratios ($f = 0.14 - 4Hz$, $\varphi = 0.14 - 6.4$ see Equation 4.10), and for the cases where the mass of MCM was constant, the maximum temperature span and available cooling power decreased with an increasing porosity ($\varepsilon = V_{fluid}/V_{total}$). The maximum available cooling power always increased with an increasing frequency. So, the available cooling power favored lower porosities, and higher frequencies of operation. A higher porosity was linked to a lower predicted NTU. Higher frequencies of operation increase the velocity of the fluid surges (for a constant utilization ratio) which increases the convective heat transfer between phases (generally the Nusselt number (Nu) increases with the Reynolds number (Re), see [104]). However, it leaves less time for the heat transfer to take place. Even though the NTU is lower at of higher frequencies, the available cooling power increases by reducing the time of the AMR cycles.

[96] analyzed the consequences of varying the particle diameter of packed bed regenerators through a 1D numerical model. Decreasing the particle diameter increases the heat transfer surface of the packed bed, so at a constant frequency, the maximum cooling load increases with a decreasing particle diameter. More heat could be transferred to the liquid phase at the same surge time. Similarly to [60], they found that higher frequencies of operation are linked to a higher optimal mass flow rate. Nonetheless, unlike [60], after hitting a maximum, the cooling load decreased for higher frequencies of operation. This means that the convective heat transfer rate did not increase enough at higher mass flow rates to compensate for the reduced surge time. This effect was more pronounced at higher temperature spans. Indeed, the temperature span is representative of a cooling load that takes place within the regenerator. The equilibrium between the longitudinal conduction and the cooling power of the machine results in the temperature span at "zero" cooling load. So, at higher temperature spans, the regenerator has less available power to handle a cooling load at the cold heat exchanger. The COP showed a maximum at lower particle diameters and higher frequencies of operation because of the increased viscous losses. The pumping work increased due to an increase of the mass flow rate at higher frequencies of operation. At the same time, the viscous friction term in the energy equation increased, increasing the rejected heat. So, the optimum particle diameter increased at higher operating f.

[102] calculated the performance of active regenerators made of wires that are parallelly stacked to the direction of the flow. The calculations were done by a 1D numerical model and the investigated geometrical parameter was the diameter of the wires. Similar conclusions to past publications were drawn: the reduction of the wire diameter increases the cooling load and the viscous losses. This kind of regenerator showed slightly better COP and cooling power when compared to packed bed regenerators. Similarly to [96], the cooling load hit a maximum when increasing the operating frequency. In this case, it was most certainly due to a Nusselt number that was independent of the fluid velocity.

[95] calculated the optimal mass flow rate for the maximum COP and cooling power (Q_{cool}) for various geometrical parameters of plate and packed bed regenerators with a 1D numerical code. The simulations included 2 frequencies of operation (0.5 and 3Hz). The studied geometric parameters were: the regenerator length, particle diameter, plate thickness, and porosity. Like past findings, the studied plate regenerator geometries achieved a higher COP and a lower Q_{cool}^{max} when compared to packed-bed geometries. Similar to past authors, they concluded that thinner plates and smaller particles increase Q_{cool}^{max} in detriment of increasing the viscous losses.

[97] tested the performance of different AMR geometries experimentally. The geometries included 3 packed bed regenerators with different particle diameters and shapes, and another 3 plate regenerators with different plate thicknesses and spacings, as well as different orientations in regard to the applied magnetic field. In terms of the maximum temperature span, the optimum frequency and mass flow rate were related to the overall convective heat transfer properties of the regenerator. A higher heat transfer surface led to higher optimum frequencies and mass flow rates. They concluded that the efficiency of parallel plate regenerators was superior, and that the research towards more efficient regenerators should be focused on ordered structures.

[45] calculated through a 1D numerical model the performance of the following regenerator geometries: packed spheres, packed screens, parallel plates, and micro channels. The mass flow rate was tuned to get a cooling capacity of 100W/kg at a temperature span of 280-300K. They mapped the COP and the generated entropy for two variables: operational frequency and the aspect ratio of the regenerator volume $R_a = L/\sqrt{A_{cross}}$). The COP did not include the pumping power ($COP = Q_{cold}/(Q_{hot} - Q_{cold})$), and the volume of the regenerator was always kept constant. Packed screens, parallel plates, and micro channels were found to have a higher optimum COP when compared to packed sphere beds. As the following approximation exemplifies for the case of packed beds, the hydraulic diameter

and the heat transfer area (A_{HT}) have an inverse relationship if volume (V) and ε are kept constant ([3]):

$$A_{HT} = \frac{6}{D_p} V(1-\varepsilon) \tag{4.3}$$

[45] detailed how for each of the tested geometries, at constant porosity, the optimum COP (in terms of frequency and R_a) had a maximum for the hydraulic diameter (or equivalently for A_{HT}). As A_{HT} increases, so does the COP because of an increase in the cooling power. As calculated by [96], past a maximum, the heat generated by friction increased, increasing the heat rejected at the hot heat exchanger and lowering the COP. Geometries with lower A_{HT} favored lower frequencies of operation and larger R_a. As [96] and [97] detailed, the reduced heat transfer (by reducing A_{HT}) demands more surge time and lower conduction losses to achieve the optimum COP. The highest COP values seemed to favor higher porosities (around 0.64) for all the studied geometries, while the porosity of packed spheres is usually around 0.33 (see [41]).

[92] measured the cooling power and COP of packed bed, parallel plate and square pin regenerator geometries. They kept similar Gd mass, D_h, and porosity in the same regenerator housing. Thus, the results were characteristic to the specific geometries. The matrix of pins gave a close performance to the packed-bed regenerator. It had a slightly lower cooling capacity and better efficiency due to the lesser viscous losses. As previous authors ([101], [95],[97]); [92] concluded that packed bed geometries trade heating power for efficiency.

A few other authors have investigated the influence of geometry on the perceived magnetic field of a porous structure. In an AMR, the geometry not only determines the heat transfer properties and viscous losses of the HTF, but it also determines how the external magnetic field is funneled into the MCM, which is the fundamental phenomenon that drives the MCE. Usually, the analytic methods to calculate the perceived magnetic field are limited to isolated ellipsoids of constant magnetization ([54]). However, averaged solutions have been found for isolated rectangular prisms and cylinders ([1], and [73]). [52] experimentally validated an analytical method to approximate the demagnetizing field of a conglomerate of identical 2D particles of relatively high porosity ($\varepsilon > 0.9$). They detailed how the total demagnetizing factor is a sum of the self-demagnetizing factor and the dipolar interaction factor:

$$\begin{aligned} N_T &\approx N_{self} + N_{dip} \\ &\approx N_{self} + (N_{macro} - N_{self})(1 - \varepsilon) \end{aligned} \tag{4.4}$$

The demagnetization due to dipolar interaction (N_{dip}) was proposed as a function of the demagnetization of the macroscopic conglomerate N_{macro}, of the isolated pins N_{self}, and ε. [11] calculated with a 3D magneto-static model, the total demagnetization of rectangular prismatic packed beds, made of spherical particles. In terms of the particle size, the packed beds had monodispersed, normal and lognormal distributions. They also included 3 different aspect ratios for the macroscopic shape of the packed beds: 1, 1.5, and 2. The dimension that changed to accommodate the aspect ratios was parallel to the external uniform field. For relatively low relative magnetic permeabilities ($\mu_r \approx 2$, characteristic of Gd at 1T) Equation 4.4 fitted well the simulations. However, when μ_r was increased, the demagnetization decreased logarithmically. Thus, the total demagnetization N_T must be a function of μ_r too. Before [11] and [52], [18] studied the demagnetization of stacked plates. They studied different combinations of porosity, plate thickness, total size of the stack, and orientation of the external magnetic field. Their findings followed the logic of Equation 4.4.

[90] summarized the main challenges magnetic refrigeration faces. The total MCM mass and regenerator volume should be kept to a minimum, while the regenerator delivers a useful cooling load at a reasonable temperature span. So, the optimal geometry will depend on how three physical phenomena interact: the magnetic field, fluid flow and thermal energy. So far, the literature suggests that larger porosities seem to reduce the demagnetization and friction losses, but increase the magnetized volume and reduce the heat transfer by convection. Those larger porosities are translated into lower optimum frequencies of operation, a higher COP, and lower Q_{cool}.

Also, most of these results have been obtained with 1D numerical models. These models employ averaged correlations to model the heat transfer (Nu), demagnetization (N_T), and viscous losses (friction factor). This approach limits the scientific research to geometries where the dimensions of the regenerator are much larger than the characteristic length of the porous media. This might be sufficient when correlations are available and only the macroscopic behavior of the regenerator is of interest. However, correlations cannot model arbitrary geometries, and do not provide insight on how exactly the physical phenomena

develop within the regenerator. The latter is important to understand and engineer the geometry of future regenerators.

The novelty of the following study is threefold:

1. The presented data has been directly computed employing the thoroughly validated 3D AMR solver presented by [56].
2. A characteristic parameter of porous geometries has been studied: the tortuosity of the fluid surges (see the following Equation 4.5).

$$\tau = \frac{\int tr(x)dx}{L} - 1 \tag{4.5}$$

3. The cases studied here are centered on regenerators made of pins. Pin geometries are characterized by having the largest of their dimensions parallel to the applied magnetic field, which is the easy axis of magnetization. Another advantage is the reduced conduction losses due to the separation of the pins.

First, the proposed geometries are analyzed according to the three separate physical phenomena mentioned earlier. Then the full AMR operation of those geometries is directly simulated. The AMR simulations are centered on a single MCM stage of Gd and have a cyclic magnetic field characteristic of rotatory configurations (much like the prototype by [29]). This methodology has the objective of elucidating the relationship between the three separate phenomena (magnetic field, fluid flow and thermal energy) and the performance of the AMR.

4.2.2 Numerical code

The 3D solver presented by [56] directly solves the fundamental physical phenomena that take part in the AMR cyle:

1. A magnetostatic field computed by the scalar magnetic potential ($H = \frac{\partial \phi}{\partial n}$). Different domains have a constant magnetic permeability.
2. A steady state fluid flow field computed by solving Navier-Stokes equations with a constant viscosity.
3. A thermal field computed through the transport of energy, for the flow described by the Navier-Stokes equations. The MCM domain has a field distribution of the heat capacity ($c = c(H, T)$), and the following MCE source term:

$$\mu_0 T \left.\frac{\partial M(H,T)}{\partial T}\right|_H \frac{\partial H}{\partial t} \tag{4.6}$$

The validation of the 3D AMR solver was undergone by first validating the resolution of the separate physical phenomena, and then comparing the AMR cycle simulation to a detailed parallel plate experiment by [6]. Grid Sensitivity Analyses (GSA) were performed for every case, and all the discretized differential terms were represented by second order accurate numerical schemes. The solver employed in this study was developed within the OpenFOAM framework (Open Field Operation And Manipulation). This framework constitutes an open source library of mathematical tools written in C++. The tools included in OpenFOAM let the user solve partial differential equations of discretized mathematical fields through the finite volume method. OpenFOAM also includes a native geometry mesher, snappyHexMesh. That one and cfMesh were employed to generate the grids of this study.

4.2.3 Phenomenological study

In this section the properties of the pin geometries of Figure 4.2 and Table 4.1 are studied.

All cross-sections of Figure 4.2 have an area of $1mm^2$. The simulations of the magnetic, fluid, and thermal fields are done with the solvers presented by [56]. The reader is referred to that article for a thorough explanation of the solved equations and the validity of the solutions. Two types of pin clusters are studied: straight and staggered (see Figure 4.3). Straight clusters have the center of the pins aligned to each other, and staggered clusters have alternate columns of pins aligned with the interstice of the neighboring pins.

Demagnetization

In this subsection, the validity of Equation 4.4 is tested for the geometries presented in Figure 4.2, and the two arrangements of Figure 4.3. Indeed, it is yet unclear how the arbitrary outlines of the pins affect N_{dip} and N_{self}. The height of all the tested geometries was $10mm$, so the factor $H/\sqrt{A_{cross}}$, and volume of the pins stay constant through all the

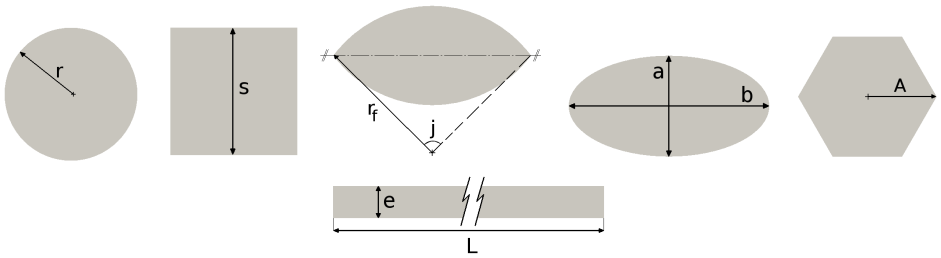

Figure 4.2 Description of the simulated pin cross-sections. From left to right and top to bottom: circle, square, foil, ellipse, hexagon, and plate.

Parameter	*Value*
r	$0.5642mm$
s	$1mm$
r_f	$1.12mm$
j	$106.26°$
a	$0.7979mm$
b	$1.5958mm$
A	$0.6204mm$
e	$0.25mm$
L	$4mm$

Table 4.1 Values for the geometrical parameters of Figure 4.2. All pin cross-section areas are $1mm^2$.

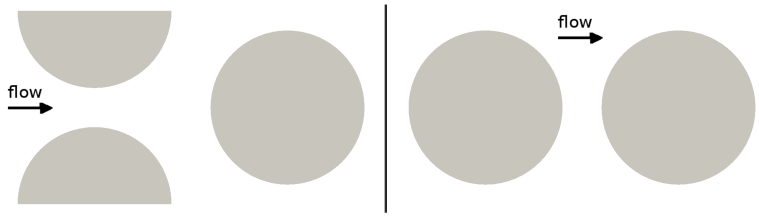

Figure 4.3 Tested pin regenerator layouts: left, staggered; right, straight.

cases. The porosity ε defines the space between pins, which is always the same for both cartesian directions.

The symmetries of the problem were exploited so that the computational domain could be simplified (see Figure 4.4). The sides of the domain were set to a zero gradient of the magnetic scalar potential. The applied magnetic field at the top and bottom boundary conditions imposed a uniform magnetic field of 1T parallel to the longitude of the pins, and were chosen far enough not to influence the solution near the pins. The magnetic permeability was chosen to be $\mu_r = 2$, similar to the one of Gd around 0-1T (see [11] and [56]). Figure 4.5 shows the GSA for the case with the finest geometrical features: staggered plates of $\varepsilon = 0.5$. A minimum cell size of $6\mu m$ at the surface of the pins was necessary to obtain a magneto-static solution that is independent of the discretization size.

Table 4.2 shows the self-demagnetization factor calculated with Equation 4.7 ([54]). To calculate N_{self} there is no need of a symmetry boundary condition, so the far-field boundary was chosen far enough not to disturb the solution around the pins.

$$H_{int} = H_{app} - NM \tag{4.7}$$

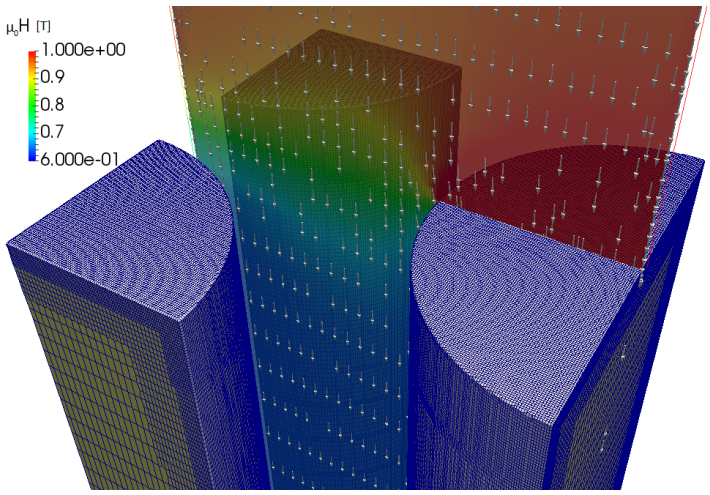

Figure 4.4 Example of the calculated magnetic field on the staggered circular cross-section of $\varepsilon = 0.5$. The yellow colored boundary cells had a zero gradient condition for the magnetic scalar potential.

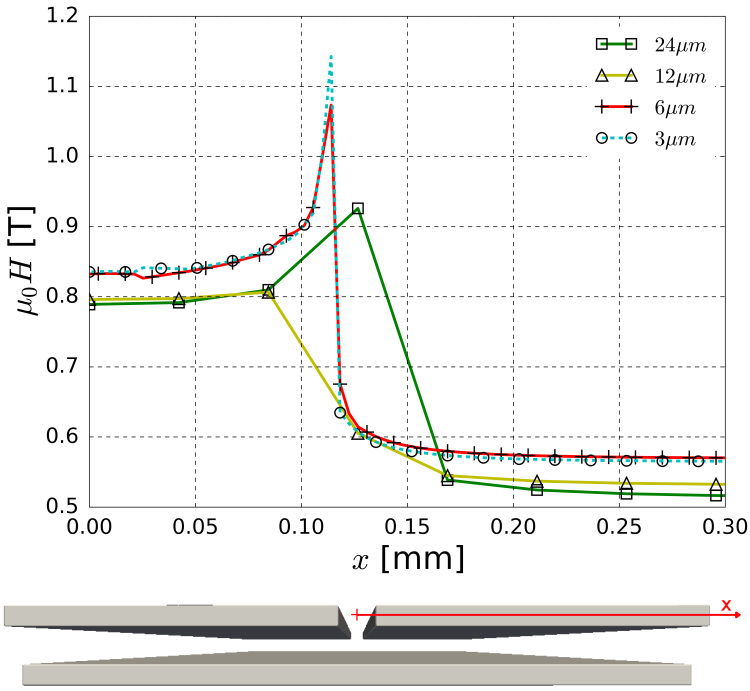

Figure 4.5 Magnetic field at the top of the staggered plate pins as the cell size decreases ($\varepsilon = 0.5$).

Type of pin	$N_{self} \cdot 10^3$
Circle	59.165
Square	59.55
Foil	57.72
Ellipse	58.44
Hexagon	59.126
Plate	45.337

Table 4.2 Standalone demagnetization for the pins described in Figure 4.2 and a height of $10mm$. The side far field boundary conditions were chosen so far, there was only a 10^{-3}T deviation in respect to the applied magnetic field (1T).

There is only a small variation of the demagnetization factor between the different cases of Table 4.2. Thus, it can be concluded that the outline of the pins does not affect N_{self} substantially, as long as the form factor $H/\sqrt{A_{cross}}$ is kept constant. Next, N_T is calculated for straight and staggered clusters of pins (Figure 4.6).

N_{macro} for the approximation of Equation 4.4 was set to 1, because in the limit case of $\varepsilon = 0$ the demagnetization of an infinite slab tends to 1. Since the magnetic field is a solenoidal field ($\nabla \cdot B = 0$), when all the applied magnetic field crosses to the MCM:

$$\mu_I H_I = \mu_{II} H_{II} \tag{4.8}$$

$$\mu_0 H_{app} = \mu_0 (H_{int} + M) \tag{4.9}$$

Equation 4.9 is an expression analogous to Equation 4.7 if $N = 1$. Equation 4.7 overestimates the total demagnetization of straight clusters by almost 0.1 in the worst case ($\varepsilon = 0.5$). Staggered clusters present a slightly higher demagnetization. The tendency seems to be quite linear for both kinds of clusters. Other authors ([11], [73]) have pointed out that the total demagnetization reaches an asymptotic minimum as μ_r increases. So, for higher values of μ_r the discrepancy between the approximation and the computed N_T should increase. Equation 4.7 might be a good option to approximate N_T for packings of high $\varepsilon > 0.5$, and low μ_r difference with the reference case (N_{self}).

Pressure losses and heat transfer

In this subsection, the pressure head and heat transfer of the geometries of Figure 4.2 are studied for the specific regenerator geometries of Table 4.3. These regenerator geometries were designed to accomodate the presented pin geometries, and to keep a similar width

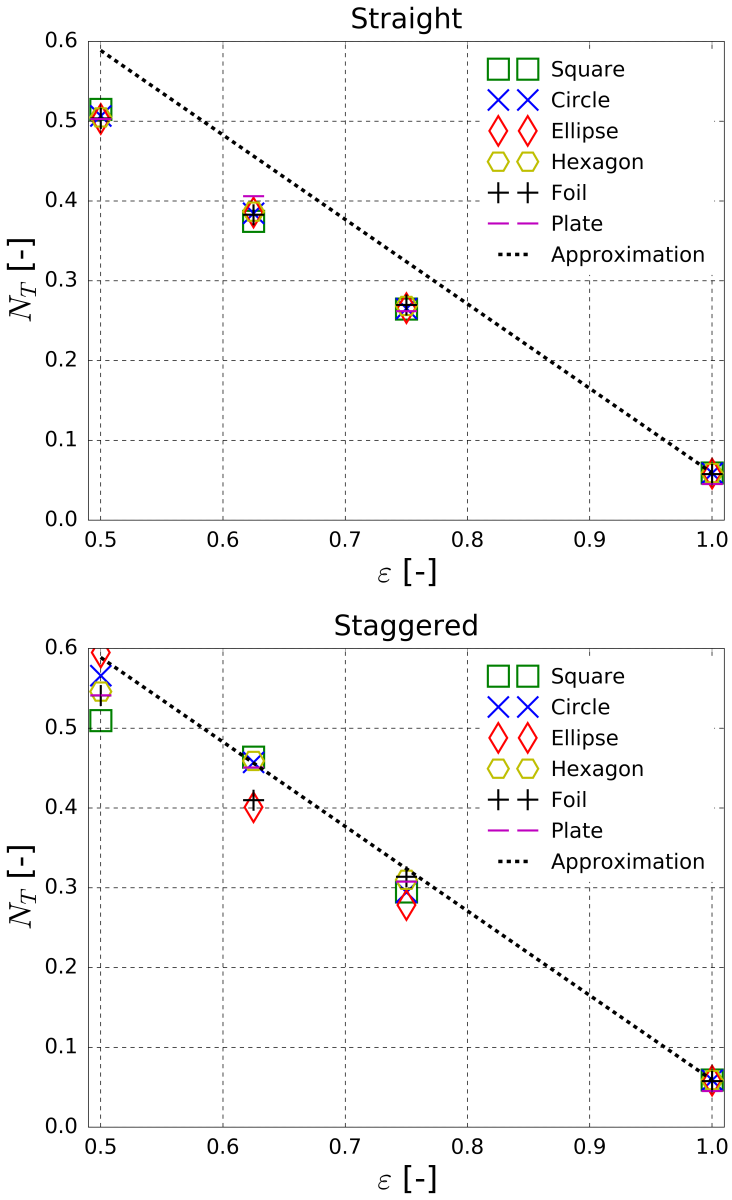

Figure 4.6 Variation of N_T with the porosity ($\varepsilon = 0.5$, 0.675, 0.75). $\varepsilon = 1$ is attributed to isolated pins, where $V_{fluid} \approx V_{total}$.

(W, see Figure 4.7). The latter constrain, ensures similar maximum and minimum bounds of the applied magnetic field. Otherwise, if the regenerator is too narrow, the magnetic flux of the high field boundary condition overflows the low field area, reducing the change in magnetic field necessary to drive the MCE. By the same logic, geometries with higher porosities, experience a slightly larger change in magnetic field due to their increased width. The relative difference in width could be reduced by simulating larger regenerators, however the cost of such simulations outgrows the present capabilities. Note that the regnerators of Table 4.3 keep a constant volume ($V_{reg} = W \cdot L \cdot H$) for the cases of same porosity. This means that, for a constant ε, the magnetized volume and the mass of MCM are constant, which establishes a good baseline for a comparative study.

The GSA of the regenerator geometries was done for the case that presents the highest gradients in the solution: staggered plates of $\varepsilon = 0.5$. The fluid properties were chosen to be like the water-ethanol mixture used by [6]: $\rho_f = 981 kg/m^3$, $c_f = 4330 J/(kg \cdot K)$, $\lambda_f = 0.52 W/(m \cdot K)$, and $\mu_f = 1.6 mPa \cdot s$. The thermal conductivity, density, and heat capacity of Gd were the same employed by [55] ($\lambda_s = 10.5 W/(m \cdot K)$, $\rho_s = 7900 kg/m^3$, and variable c_s). For the GSA, the fluid inlet velocity was set to match a conservative operational point that will not be surpassed: $f = 1 Hz$, and $\varphi = 10$.

$$\varphi = \frac{U_{inlet} A_{inlet} \chi}{4 f V_s} \tag{4.10}$$

$$\chi = \frac{\rho_f c_f}{\rho_s \bar{c_s}} \tag{4.11}$$

$$f = \frac{1}{4 t_f} \tag{4.12}$$

	W [mm]			L [mm]		
ε	0.5	0.625	0.75	0.5	0.625	0.75
Circle and Square	11.314	13.064	16	4.243	4.899	6
Foil	12.426	14.945	19.22	3.863	4.282	4.995
Ellipse	12.846	15.385	19.686	3.737	4.16	4.877
Hexagon	10.668	12.416	15.349	4.5	5.155	6.255
Straight plate	12	16	24	4	4	4
Staggered plate	12.67	13.084	13.849	3.788	4.891	6.932

Table 4.3 Dimensions of the tested regenerator geometries (see Figure 4.7). A similar width (W) was kept to have a comparable magnetic field change between cases. All geometries have 24 pins, and H=4mm for all cases.

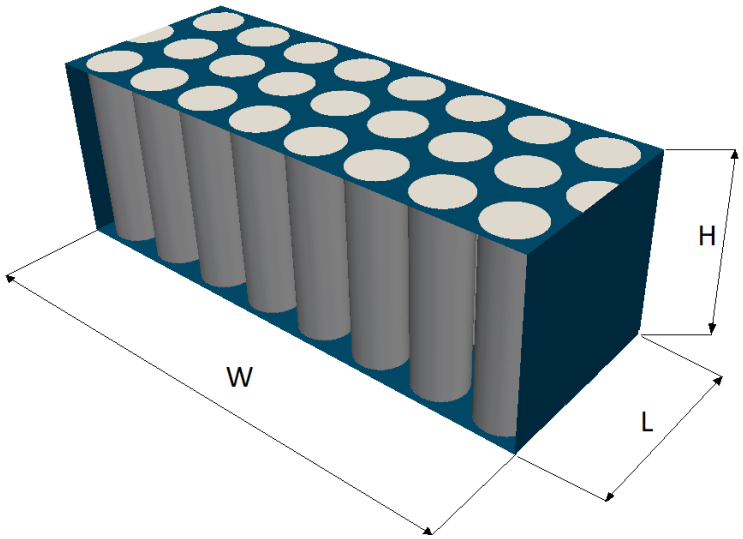

Figure 4.7 Reference for the dimensions specified in Table 4.3.

The computed cycle has a constant rotation of the magnetic field, and so, the cycle period is divided in four equal time periods (Equation 4.12). Equation 4.10 and $\bar{c}_s = 282.64 J/(kg \cdot K)$ yield an inlet velocity of $U_{inlet} = 39.8267 mm/s$ (for $f = 1Hz$, and $\varphi = 10$). Top and bottom boundary conditions of the regenerator (see Figure 4.7) were modeled as walls, but the sides were modeled by symmetry boundary conditions. That way, the influence of wall effects is kept out of the scope of this study. With a conservative approach in mind, the initial temperature of the walls was set to 310K and the inlet to 290K.

Figure 4.8 shows the velocity and temperature profiles of a steady state simulation of the fluid domain. This past figure shows how a characteristic cell size of $9.375 \mu m$ is sufficiently small to solve all the phenomena in the fluid domain. Cell sizes smaller than $50 \mu m$ for the solid domain, did not change the temperature field of the conjugated heat transfer solution after $0.25 s$ of simulation. However to ensure an accurate calculation of the heat transfer between solid and fluid phases, a size of $12.5 \mu m$ was employed in the solid domain. That way, the cells sizes of both domains are similar in size at the common boundary.

Pressure Losses

To compare the pressure head of the regenerators of Table 4.3, 2D steady state flow was directly simulated for the operational point of $f = 1Hz$, and $\varphi = 0.5$. By keeping φ constant, the mass flow is kept constant too. Thus, different regenerator widths provide different inlet velocities (The smaller the width, the higher the inlet velocity, see Table 4.3).

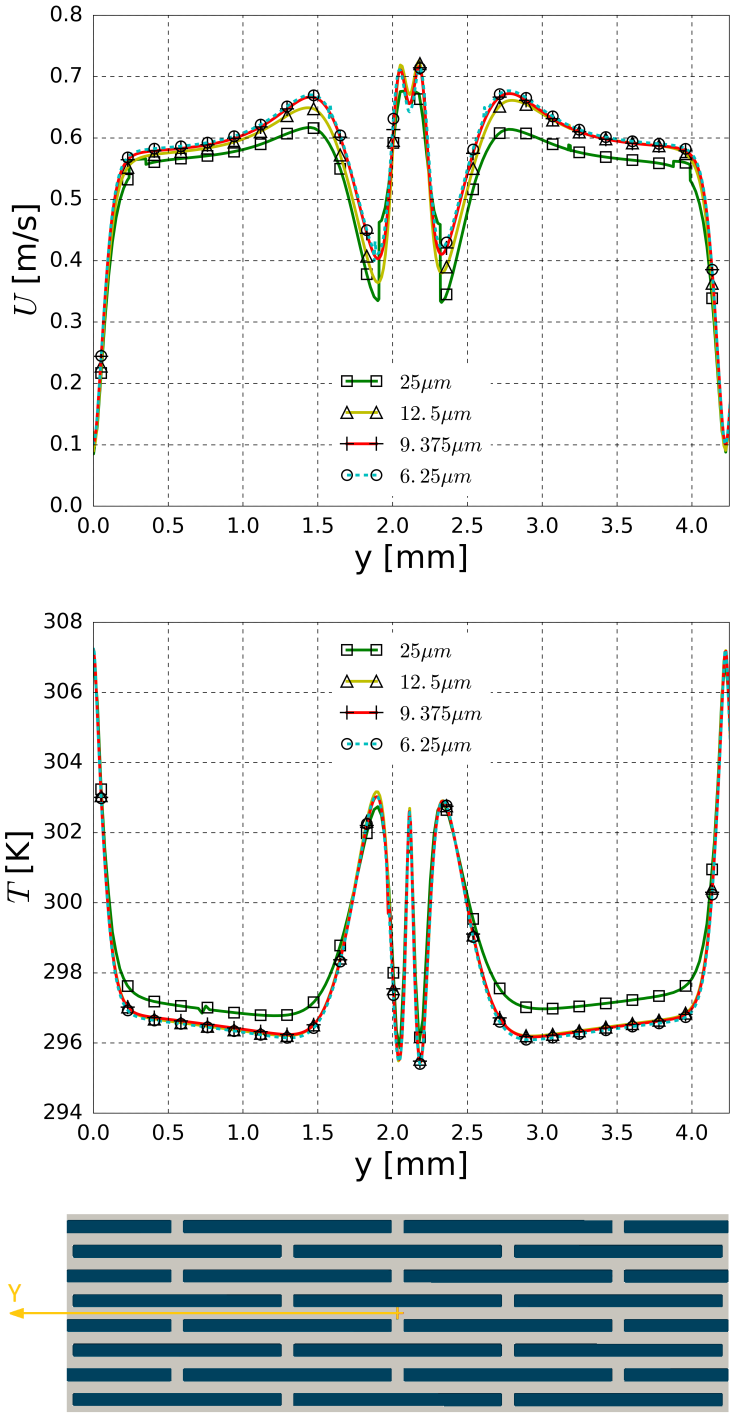

Figure 4.8 Up, velocity and temperature profiles of the GSA case at the middle of the staggered plate regenerator. Down, origin of the plotted spatial dimension.

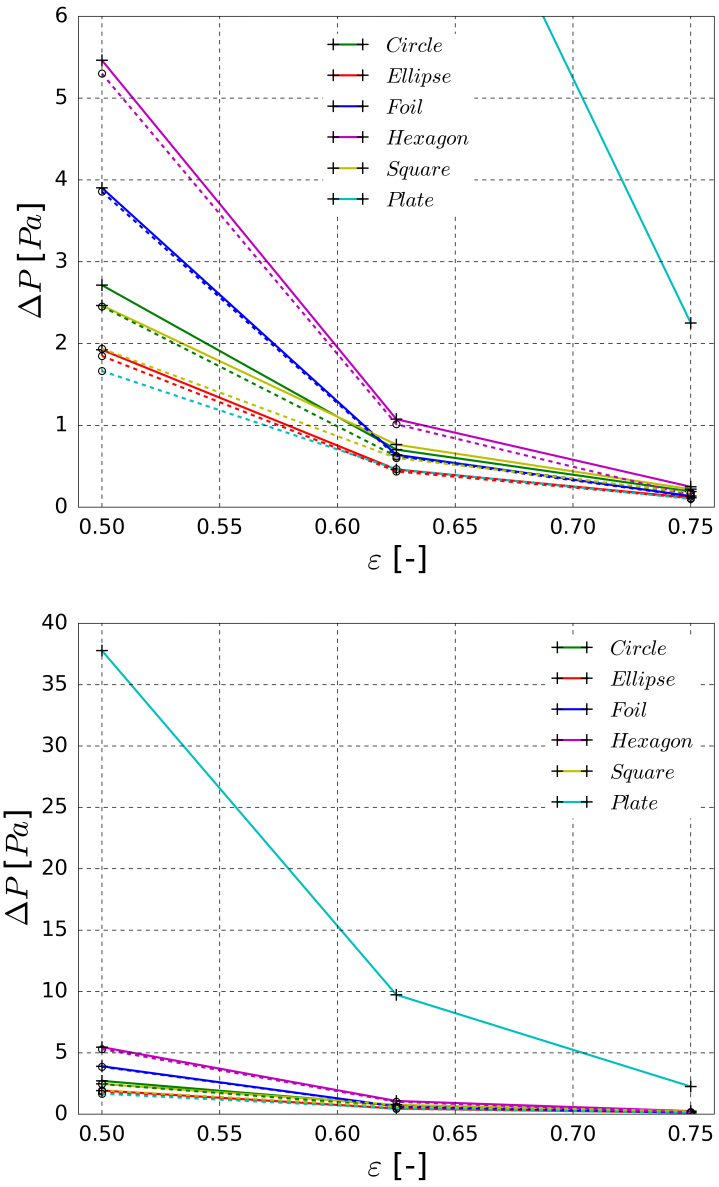

Figure 4.9 Pressure head of the regenerator geometries described in Table 4.3. Lines were drawn for a better visualization, continuous lines refer to staggered cases and dashed lines to straight cases.

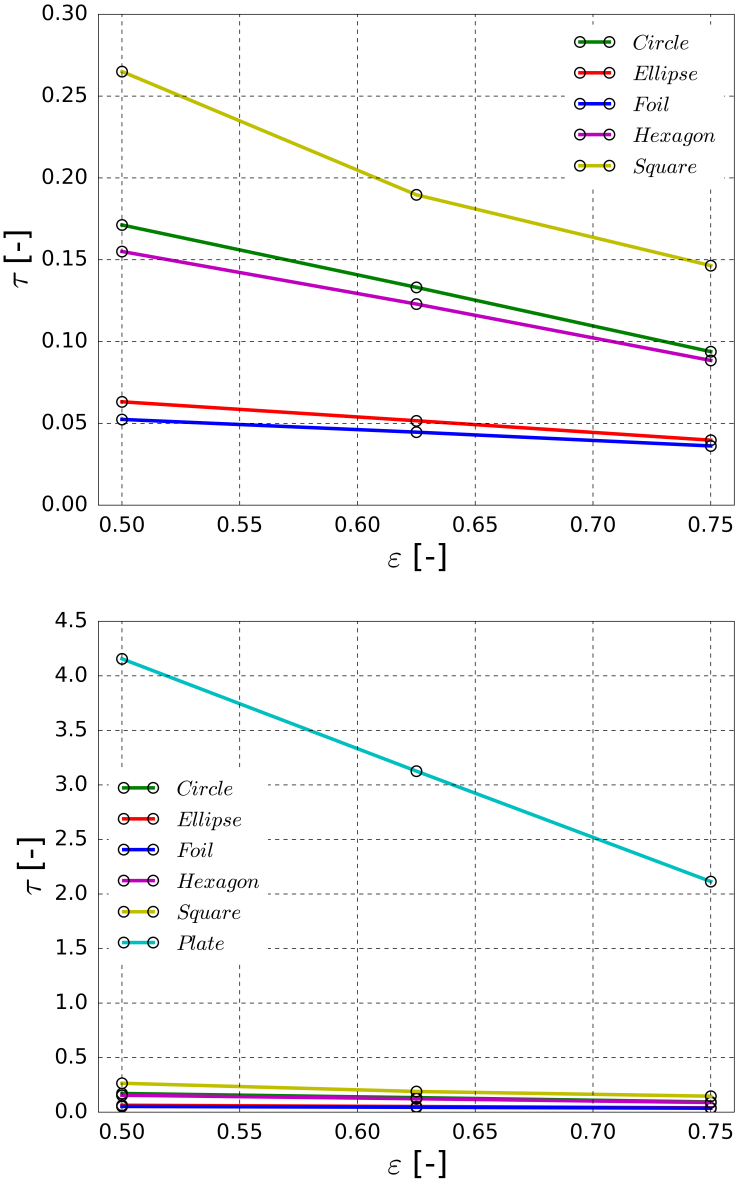

Figure 4.10 Tortuosity of the staggered regenerator geometries described in Table 4.3. Lines were drawn for a better visualization.

From Figures 4.9 and 4.10 it is concluded that the higher the tortuosity change between the straight and staggered cases, the higher is the ΔP between both cases. This difference is most apparent for the lower ε cases. The tortuosity of each geometry was calculated for an average of 10^3 streamlines that were longer than the length of the regenerator (L, see Equation 4.5). Therefore, the recirculation zones are out of the scope of τ. Straight clusters had a negligible tortuosity ($\tau < 0.02$). Since the Reynolds number Re of these simulations is rather low ($Re \approx 15$), the increase in pressure head of the staggered cases is attributed mostly to the increased shear stress at the pin walls. This increase in shear stress comes from an increase of the local velocity of the staggered cases. A higher tortuosity means that the fluid travels a longer distance to end up on the other side of the regenerator. Thus, if the mass flow is constant between straight and staggered cases, the local velocity must increase when the tortuosity increases. Furthermore, in a staggered configuration, the mainstream flow (away from the walls) has an stagnation point at the next line of pins. This exposes the mainstream flow to the wall shear stress, increasing the viscous pressure losses. Also, the flow field is always symmetrical around the pins. So if the flow was irrotational, the pressure head of the pins would theoretically be zero. Because of that, and the small flow detachments characteristic of a tight packing, the pressure head attributed to the shape of the pins is considered negligible.

Heat transfer

In order to analyze the heat transfer properties of each of the geometries of Table 4.3, a series of 2D thermal simulations were done. They all started with a 2K linear temperature gradient on both solid and fluid domains. This was approximately the maximum gradient seen on [6]. On the first set of simulations, an additional 1.5K was added to the solid domain to mimic the MCE. This is equivalent to the ΔT_{ad} of Gd for an internal magnetic field of 0.5-1T ([76]). Then, the temperature field was simulated for 0.25s without the HTF flow, and from that solution, another 0.25s were run with the fluid flow calculated in the last section 4.2.3. Figures 4.11 and 4.12 show the spatial average of the normal temperature gradients of the fluid domain at the pin boundaries, for the second half of the simulation (when the HTF is flowing).

Figure 4.11 shows how the regenerators made of hexagon, square, and circle pins achieve a slightly higher heat transfer on the staggered cases. This is replicated for all the other porosities in Figure 4.12. The decline of the surface temperature gradient of Figure 4.12 with an increasing ε is a consquence of a diminished inlet velocity due to an increase of the regenerator width for the higher ε cases (mass flow is constant for all cases). This

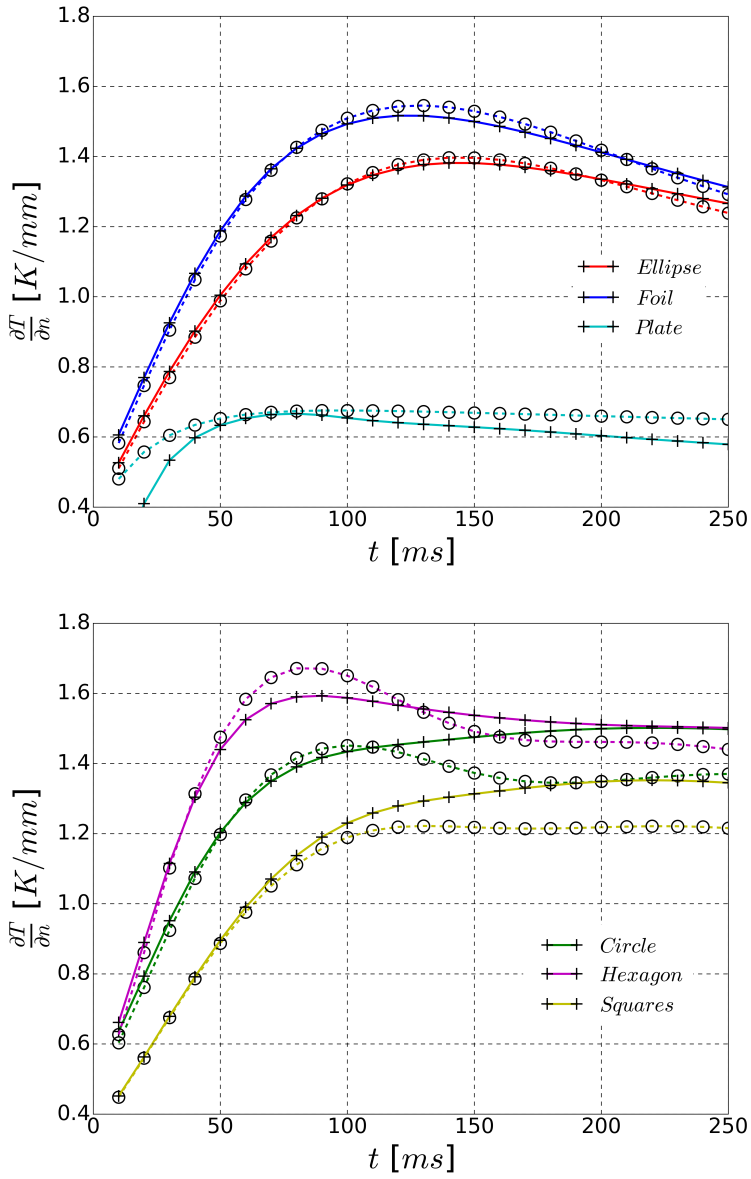

Figure 4.11 Evolution of the average temperature gradient in the fluid domain at the surface of the pins ($\varphi = 0.5$). Lines were drawn for a better visualization, continuous lines refer to staggered cases and dashed lines to straight cases.

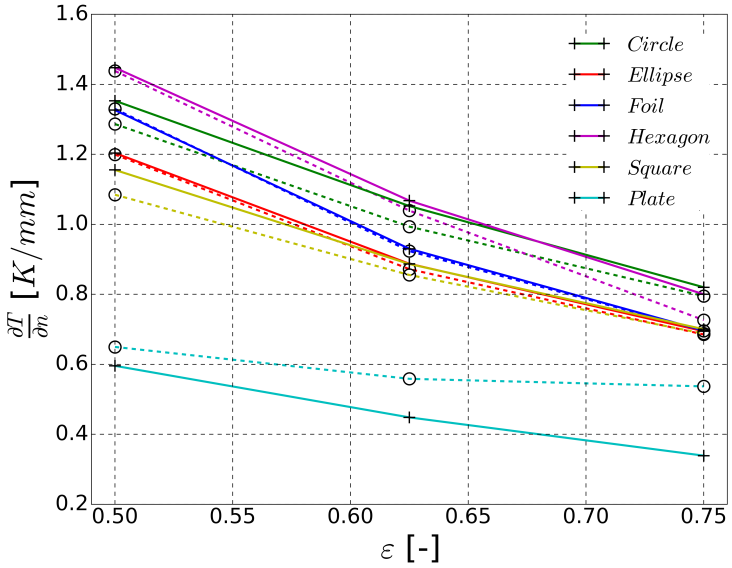

Figure 4.12 Overall average temperature gradient in the fluid domain at the surface of the pins for different porosities ($\varphi = 0.5$). Lines were drawn for a better visualization, continuous lines refer to staggered cases and dashed lines to straight cases.

is why, as seen in the literature, the maximum performace of the AMRs with higher ε is found at higher φ.

However, the staggered plates do not seem to follow this small improvement for $\varphi = 0.5$. Because of their much higher tortuosity, the cold flow does not reach as far down the regenerator as it does for the straight plates. Consequently, some streamdown plates do not come into contact with the cold inlet flow. Figure 4.13 shows the same calculations, but for the case of $\varphi = 1.5$. There, the staggered plates show a much higher heat transfer, when compared to the straight plates working in the same conditions.

From Figures 4.11 and 4.13 it can be concluded that, if φ is high enough, the heat transfer between phases increases when τ increases. So, τ acts as a multiplier of the inlet velocity. It increases the local velocity within the regenerator, and thus the convective heat transfer.

For the second set of simulations, no additional temperature was added to the solid phase, and the calculations were run without the fluid flow for 0.25s. The goal was to evaluate the longitudinal heat diffusion in all the presented geometries. Figure 4.14 shows the volume average of the total generated entropy by conduction (see Equation 4.13, Figure 4.17 indicates the spatial direction of the gradient).

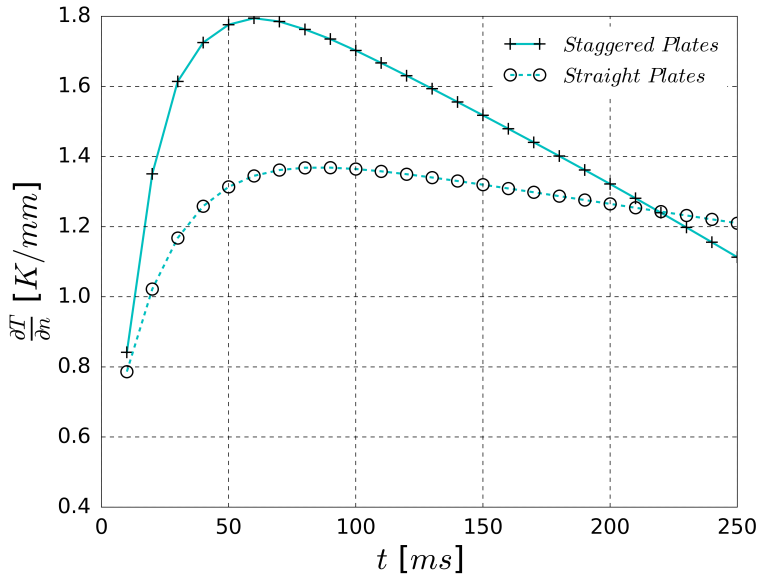

Figure 4.13 Evolution of the average temperature gradient in the fluid domain at the surface of the plate pins ($\varphi = 1.5$). Lines were drawn for a better visualization, the continuous line refers to the staggered case and the dashed lines to the straight case.

$$S_{cond} = \int \frac{\lambda_f}{T_f^2}\left(\frac{\partial T_f}{\partial x}\right)^2 + \frac{\lambda_s}{T_s^2}\left(\frac{\partial T_s}{\partial x}\right)^2 dt \tag{4.13}$$

The difference between staggered and straight cases is minimal, with the exception of the plate pins (see Figure 4.14). In the case of the straight plates, the solid phase holds the entire initial temperature gradient (2K/4mm), which is translated in an increase of the conduction losses due to $\lambda_s >> \lambda_f$. For the staggered plates, the initial gradient is split between the fluid an solid domains many times. So the thickness of the staggered plates hold a much smaller temperature gradient. The diminishing trend of S_{cond} with ε in Figure 4.14 is caused partly, by a lower initial temperature gradient due to the longer regenerator length of the higher ε cases, and partly by the increased proportion of fluid with lower λ. The latter lowers the volumetric average of S_{cond}.

4.2.4 AMR simulation

In this section the AMR cycle of some of the geometries of Table 4.3 is simulated. First of all the GSA of the magnetic field solution is checked. The magnetic field is set up to represent the conditions of a rotatory regenerator. The magnetic field swipes at a constant speed from one side to the other, always in the same direction (positive to r, see Figure

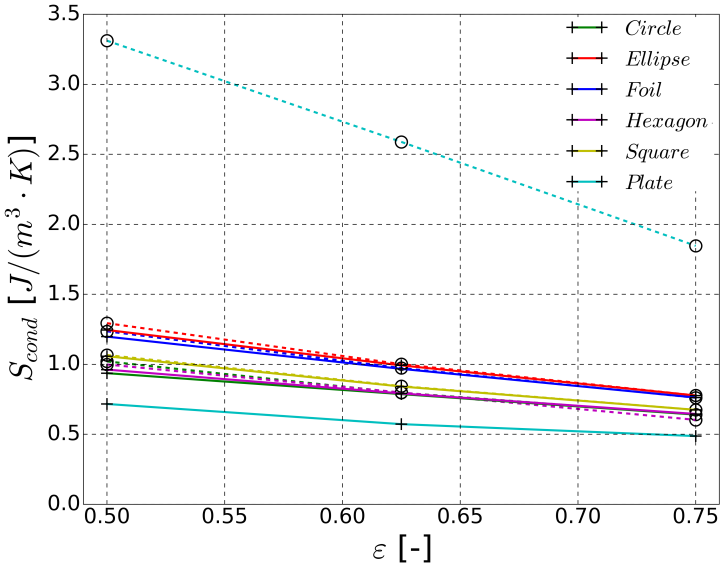

Figure 4.14 Overall generated entropy by conduction after 0.25s and a $\Delta T = 2K$ on the geometries of Table 4.3. Lines were drawn for a better visualization, continuous lines refer to staggered cases and discontinuous to straight cases.

4.15). The speed of the magnet is determined by the cycle frequency ($1Hz$). As implied by Equation 4.12, (de)magnetization time is equal to the fluid surge times ($t_{mag} = t_f$) . In order to model the influence of neighboring regenerators, half a regenerator is placed on both sides of the investigated geometry (grey plates on Figure 4.15) The neighboring half regenerators are linked to each other through periodic boundary conditions (see Figure 4.16). Effects of curvature were neglected, so the circumference of the machine is hypothesized to be substantially larger than the height of the pins (4mm). The modeled regenerators were designed to represent a single MCM stage, so the magnetic boundary conditions of the cold and hot sides are symmetric, as if another stage was present next to the cold and hot sides.

Figure 4.15 shows the GSA on the case with the finest geometry details (staggered plates of $\varepsilon = 0.5$). The size of $12.5\mu m$ employed before for the MCM domain seems to be fine enough to calculate the magnetic field. The intensity of the field was set to 1T at the moving magnet boundary, and the airgap was 1 mm. For the GSA, the magnet was set still at the beginning of the left periodic boundary condition (see Figure 4.16).

Sections 4.2.3 and 4.2.3 showed how τ needs to be larger than 2 to have a glaring effect on the regenerator properties. The computational cost of simulating an AMR cycle is relatively high (see [56]) so, only the following regenerator geometries were simulated: Staggered plates and circles, and straight plates. The last two were chosen so that the

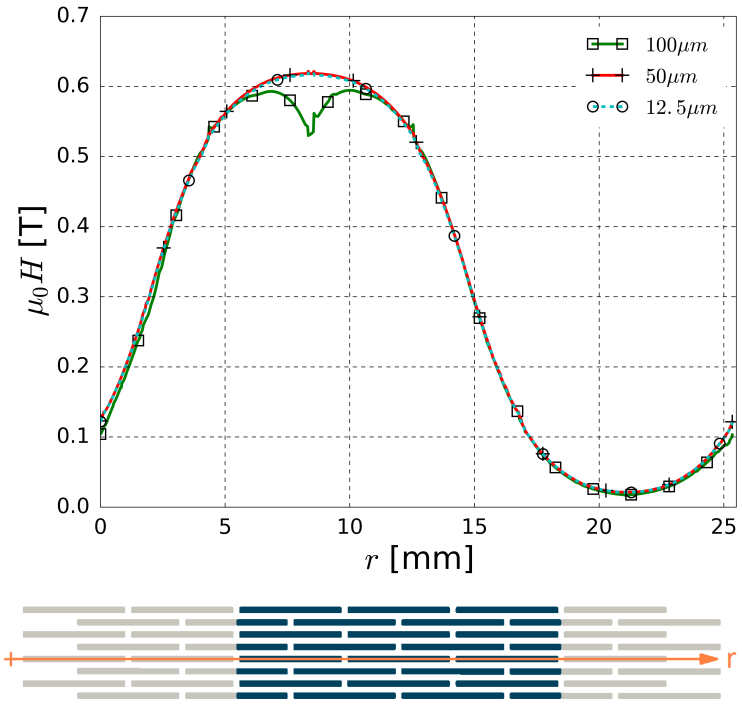

Figure 4.15 Magnetic field through the center of the staggered plate regenerator, for different cell sizes.

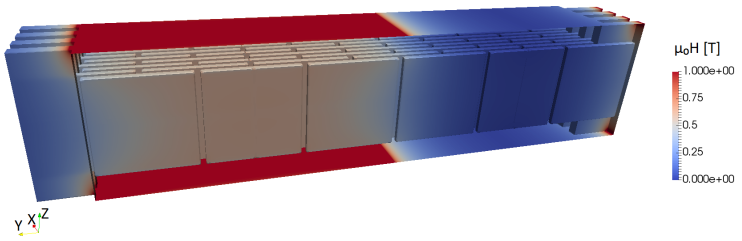

Figure 4.16 3D view of the case plotted in Figure 4.15. For the GSA, the magnet boundary condition of 1T was set between the regenerator of interest (blue) and the neighbor (grey) of Figure 4.15.

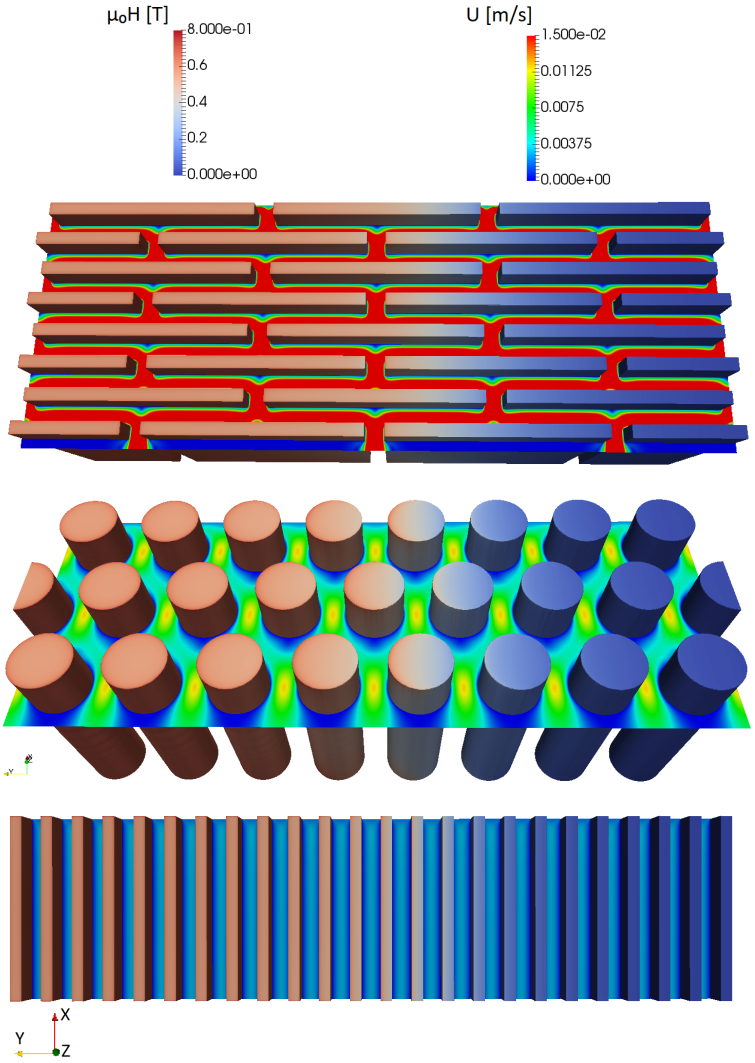

Figure 4.17 Magnetic and Velocity fields of the AMR cycle simulations, at the middle of the hot surge, for the case where $\varphi = 0.6$ and $\varepsilon = 0.625$. Top to bottom: staggered plate, staggered circle, straight plate. Velocity magnitude contours show how the higher tortuosity cases have a higher local velocity.

reader can make comparisons with other published regenerators. Figure 4.18 shows the temperature span of the regenerators at zero cooling load, for a fixed hot heat exchanger temperature of 300K. A steady state solution was reached when ΔT_{reg} changed less than 0.01K between cycles.

The best results are observed for the staggered plates. It seems that the increased heat transfer and the reduced conduction losses that come from increasing τ, enable the staggered circle and plate regenerators to work at noticeably higher temperature spans. Staggered circles and straight plates show a decreasing ΔT_{reg}, when increasing ε. As Figures 4.6, 4.12, and 4.14 show, by increasing ε demagnetization decreases, Nu decreases (at constant φ), and the conduction losses are slightly reduced. Thus in the case of staggered circles and straight plates, the reduction of Nu overwhelms the two other positive effects of increasing ε. Also, the maximum ΔT_{reg} comes at higher φ, for higher ε cases. This maintains coherence with past findings, as more mass flow (φ) is needed for the higher ε cases to reach the same Nu value.

The staggered plates show an inverse behavior: ΔT_{reg} increases when ε increases. This means that the benefit of the decreased demagnetization and conduction losses outweighs the reduced Nu of higher porosities. The benefits of reducing the conduction losses can be clearly seen for $\varphi = 0.5$. Figures 4.6 and 4.11 show how N_T and Nu of staggered and straight plates of $\varepsilon = 0.5$ are similar. Therefore, the reason why ΔT_{reg} is higher for staggered plates than for straight plates at $\varphi = 0.5$ in Figure 4.18, must be because of the reduced conduction losses of Figure 4.14.

A drawback of the staggered plates is the increased pressure head. However, the minimum ratio between the rejected heat and the pumping work was $\frac{Q_{hot}}{W_{pump}} = 368.4$ (staggered plates of $\varepsilon = 0.5$ at $\varphi = 1.8$). Thus for these geometries, the magnetic work is still significantly higher than the pumping work. Furthermore, the higher ΔT_{reg} cases come at higher ε cases which showed a noticeably lower pressure losses in Figure 4.9.

4.2.5 Conclusion

A detailed phenomenological analysis of AMR pin regenerator geometries was undergone. Demagnetization, pressure head and heat transfer properties were analyzed before computing the temperature span of their AMR cycle. All regenerators had the same amount of MCM distributed equally between the pins. The outer shape of the regenerators was kept as similar as possible, in order to maintain a similar magnetic field change and flow velocity. The introduction of a larger tortuosity by changing the arrangement and shape

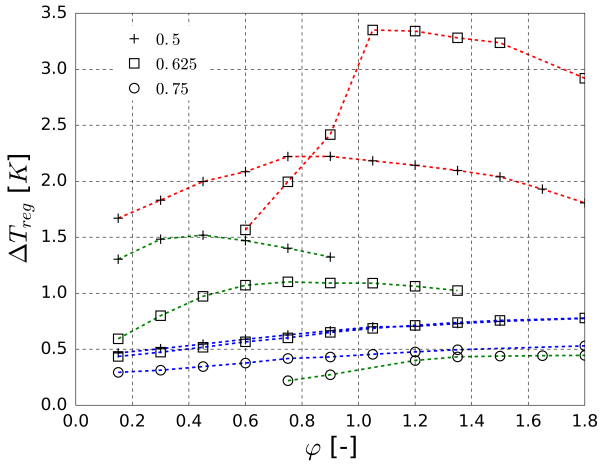

Figure 4.18 Temperature span of the staggered plates (red), staggered circles (green), and straight plates (blue) for a zero cooling load and a constant 300K in the hot heat exchanger. Symbols represent different values of ε.

of the pins resulted in the following: slight increase of the total demagnetization (less than 0.1), increase of the pressure head, increase of the convective heat transfer, and decrease of the conduction losses. The increase of the pressure head and convective heat transfer is caused by an increase of the local velocity within the regenerator, due to the longer trajectory the HTF must follow at a constant mass flow. Simulations of the AMR cycles indicate that the main contribution to the increased temperature span of the higher τ cases is due to the reduction of the conduction losses. Furthermore, ΔT_{reg} seems to increase with ε for the highest tortuosity cases. This means that the decrease of conduction losses and demagnetization, outweighs the reduced inlet velocity for higher ε cases.

The increase of tortuosity is believed to be an alternative solution to increase the power of magnetocaloric regenerators. To increase the cooling power of packed beds, the strategy has been to increase the heat transfer surface by employing smaller particles. However, packed beds have their particles in contact with each other, which increases the conduction losses as ε decreases. Staggered arrangements of elongated pin cross sections, have inherently less conduction losses, and can provide a similar increase in convective heat transfer due to the local increase of fluid velocity. Furthermore, if most of the heat transfer is controlled by the fluid surges (due to the increased local velocity of the high τ cases), the thermodynamic cycle will be closer to a Brayton-like cycle. This comes from an increased difference of Nusselt number betweeen the (de)magetization and surge periods. Also, since higher tortuosity cases proved to work better at higher porosities, the magnet could possibly be reduced to avoid magnetizing stripes of HTF parallel to the swiping motion of the magnetic field.

Acknowledgments

This work is part of the NSERC chair on industrial energy efficiency established at Université de Sherbrooke in 2014 with the support of Hydro-Québec, Ressources Naturelles Canada (CanmetENERGIE), and Rio Tinto Alcan that are gratefully acknowledged for their financial support. The calculations have been performed on the *Mammouth Parallèle 2* cluster of Compute Canada, which is also here gratefully acknowledged.

4.2.6 Nomenclature

A	Area/Surface	$[m^2]$
B	Magnetic field flux	$[T]$
c	Heat capacity	$[J \cdot kg^{-1}K^{-1}]$
F	Force	$[N]$
f	Frequency	$[Hz]$
N	Demagnetization factor	$[-]$
Nu	Nusselt number	$[-]$
M	Magnetization	$[A \cdot m^{-1}]$
Q	Heat power	$[W]$
Re	Reynolds number	$[-]$
S	Specific entropy	$[J \cdot m^{-3}K^{-1}]$
T	Temperature	$[K]$
t	Time	$[s]$
V	Volume	$[m^3]$
W	Work power	$[W]$

Greek symbols

ε	porosity $[-]$
φ	Utilization ratio $[-]$
λ	Thermal conductivity $[W \cdot m^{-1}K^{-1}]$
μ_f	Fluid viscosity $[Pa \cdot s]$
μ_r	Relative magnetic permeability $[-]$
ρ	Density $[kg \cdot m^{-3}]$
τ	Tortuosity $[-]$

Subscripts

0	Vacuum
app	Applied
C	Curie
cond	Conduction
dip	Dipolar
f	Fluid
HT	Heat Transfer
int	Internal
p	Particle
reg	Regenerator
s	Solid

Acronyms

AMR	Active Magnetic Regenerator
CFC	Chloro Fluoro Carbons
COP	Coefficient Of Performance
GSA	Grid Sensitivity Analysis
HCFC	Hydro Chloro Fluoro Carbons
HFC	Hydro Fluoro Carbons
HTF	Heat Transport Fluid
MCE	Magneto Caloric Effect
MCM	Magneto Caloric Material
NTU	Number of Transfer Units

CHAPTER 5

CONCLUSION FRANÇAISE

Une étude numérique approfondie des cycles de AMR a été présentée. Plus important encore, la validité de la solution produite par les solveurs numériques a été soigneusement testée par rapport à des données analytiques et expérimentales. À partir du modèle 1D (chapitre 2), le MCE de Gd était le premier aspect du code numérique à être validé. La magnétisation relie les champs magnétique et thermique, de sorte que cela devient l'équation d'état des MCM. Pour la commodité du programmeur, une expression adaptée pour la magnétisation de Gd peut être trouvée dans la annexe B. La validation finale du code AMR présenté dans cette thèse a été réalisée sur deux prototypes de plaques différents ([97] et [6]). Cette stratégie s'est avérée la moins risquée en raison de la simplicité de la géométrie et des données déjà disponibles (nombre de Nusselt, coefficient de frottement et démagnétisation). L'inclusion d'un modèle magnétique dans le code 1D s'est avérée essentielle pour obtenir des résultats proches des données expérimentales. Cela signifie que la différence entre le champ magnétique appliqué et interne n'est pas négligeable. En plus de cela, avec l'aide de ce code numérique 1D, il a été démontré qu'en insérant des couches isolantes, les pertes par conduction dans le domaine MCM pouvaient être réduites.

La prochaine étape du projet consistait à développer un solveur numérique capable de produire une solution véritablement fiable. Le développement d'un solveur de cycles AMR 3D précis nécessitait un chapitre dédié (3). Ce chapitre abordait la validation du résolveur de cycles 3D AMR en abordant au début la validation de ses phénomènes physiques les plus fondamentaux: hydrodynamique, champs magnétique et thermique. Une fois que ces phénomènes calculés avec précision, le fonctionnement d'un prototype de plaques a été reproduit avec succès. Le succès de cette approche réside dans le calcul numérique direct des phénomènes fondamentaux. En effet, les solveurs 1D incluent des modèles pour le transfert de chaleur entre les phases solide et liquide (nombre de Nusselt), pour la démagnétisation du MCM (facteur de démagnétisation), pour la magnétisation du MCM (MFT), et même pour le débit de fluide. Il devient donc impossible de juger si la solution du solveur est exacte car les modèles représentent fidèlement les phénomènes ou parce que l'erreur combinée des modèles fournit une solution particulièrement proche des cas testés. La validation du solveur de cycles 3D AMR représente la réalisation de l'un des

objectifs principaux de cette thèse, car il est maintenant possible de simuler le cycle AMR de géométries quelconques. De plus, la force des phénomènes éventuellement couplés a été testée. Il a été conclu que l'écoulement de fluide et le champ thermique ainsi que les champs magnétique et thermique peuvent être découplés sans perte de précision.

Enfin, le solveur de cycles 3D AMR a été exploité dans une série d'expériences numériques pour déterminer la géométrie plus favorable de régénérateurs constitués de bâtonnets. Afin de comprendre pourquoi une configuration pourrait être meilleure qu'une autre, une analyse préalable des géométries présentées a été effectuée pour chacun des phénomènes entrants. Les bâtonnets testés conservaient une démagnétisation similaire lorsque leur facteur de forme était maintenu constant ($H/\sqrt{A_{cross}}$), quelque soit leur périmètre. En outre, l'approximation trouvée dans la littérature pour la démagnétisation de grappes de particules s'est avérée appropriée pour les porosités supérieures ($\varepsilon > 0.5$). L'introduction d'une augmentation de la tortuosité dans l'écoulement hydrodynamique a augmenté les pertes de charge des régénérateurs et leur taux de transfert de chaleur moyen, en raison de l'augmentation de la vitesse locale du fluide. Cependant, le principal avantage de l'échelonnement des bâtonnets pour augmenter la tortuosité du fluide provient de la diminution des pertes par conduction. La géométrie nécessaire pour obtenir une haute tortuosité alterne les domaines solides et fluides le long de la plage de température de la machine. Cela réduit fortement les gradients de température dans le domaine solide, qui a une conductivité thermique remarquablement supérieure. Globalement, cela pourrait constituer une stratégie alternative pour augmenter la puissance de refroidissement des AMR. Jusqu'à présent, on s'est attaché à réduire le diamètre des particules des lits, afin d'augmenter la surface de transfert de chaleur du MCM pour un transfert de chaleur plus rapide. Un transfert de chaleur rapide entre les phases permet à la machine de fonctionner à des fréquences plus élevées, et fournit ainsi une puissance de refroidissement accrue. Cependant, le faible ε associé à des particules plus petites augmente les pertes par conduction. La stratégie alternative proposée consiste à augmenter la tortuosité des régénérateurs pour: réduire les pertes par conduction et (contrairement à l'augmentation de A_{HT}) augmenter le taux de transfert de chaleur entre les périodes de magnétisation et de débits fluides. Cette dernière pourrait être la clé de la performance accrue observée dans les cas de porosité et tortuosité plus élevées. Au lieu d'augmenter le transfert de chaleur pour les périodes de magnétisation et des débits fluides (en raison d'une augmentation de A_{HT}), le nombre de Nusselt peut être transformé en un commutateur permettant la majeure partie du transfert de chaleur pendant les périodes des débits fluides. Cela devient essentiel pour produire un cycle de type Brayton capable d'exploiter des fréquences plus élevées.

L'analyse de sensibilité à la grille (GSA) est une étape cruciale de la validation numérique. En utilisant la méthode des volumes finis (voir [100]), les termes différentiels des lois physiques qui régissent le comportement du cycle de la AMR peuvent être linéarisés. Cependant, la linéarisation de ces équations différentielles partielles (PDE) a un coût en précision. En plus de l'erreur de troncature (associée à la troncature de la série de Taylor), l'erreur de discrétisation pose un défi pour le calcul des cycles AMR. En effet, les calculs présentés sont coûteux en calcul (voir la section 3.2.5), de sorte que l'utilisateur a toujours tendance à utiliser le nombre de points minimale pour une résolution plus rapide des matrices linéarisées. Cependant, l'erreur de discrétisation est pratiquement inconnue jusqu'à ce que l'utilisateur ait démontré que la solution converge lors de la réduction de la taille de la discrétisation. La GSA n'a pas été une technique largement utilisée (ou du moins rapportée) parmi les expériences numériques publiées sur les cycles AMR. Le fait de signaler la taille du maillage nécessaire peut donner au prochain utilisateur une idée du coût de calcul auquel il sera éventuellement confronté, et augmente la confiance du lecteur dans les résultats rapportés.

Perspectives futures

Le solveur AMR 3D présenté peut être conceptualisé comme un outil pour étudier les nombreuses possibilités de conception des réfrigérateurs magnétiques. Le MCM utilisé dans cette étude était le Gadolinium Gd, car sa caractérisation avait déjà été publiée dans la littérature, et la plupart des prototypes utilisent ce MCM. Cependant, une bibliothèque plus riche de propriétés MCM serait bénéfique pour la recherche sur les AMR multi-matériaux. Celles-ci sont considérées comme essentielles pour générer la puissance de refroidissement requise par les machines de réfrigération commerciales. En effet, T_C désigne une température de départ pour le changement maximal d'entropie magnétique ($\Delta s_{magnetic}$) due à une aimantation adiabatique soudaine. Cela signifie que la transition de phase tombe dans une plage de température limitée. Les MCM sont classés en fonction de l'inclinaison de l'aimantation à la température de transition entre les matériaux du premier et du second ordre (voir la figure 6.1).

Ainsi, si la plage de température du régénérateur est prédéfinie, le concepteur peut affecter différentes étapes de MCM avec un T_C qui optimise le travail magnétique.

Le code présenté nécessite une quantité relativement importante de ressources de calcul (voir la section 3.2.5). Ainsi, l'application est limitée à des domaines de calcul relativement petits (par rapport à la taille de la plupart des prototypes AMR). Cette restriction

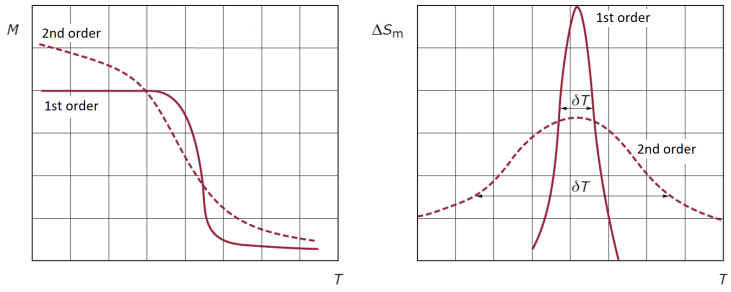

Figure 5.1 Différence entre les MCM du 1er et du 2ème ordre. Schéma modifié après [79].

provient de la longueur caractéristique généralement faible des supports poreux, qui découle de la volonté du concepteur d'augmenter A_{HT} pour un transfert de chaleur rapide. Comme cela a été commenté dans la dernière section, il serait peut-être plus avantageux d'augmenter la tortuosité de l'écoulement fluide, et donc de ne pas nécessiter un aussi gros A_{HT}. Cela pourrait réduire de manière collatérale la mémoire requise pour représenter la géométrie des AMR. Néanmoins, comme cela a été fait dans le chapitre 4, des expériences numériques peuvent être effectuées à une plus petite échelle, puis les résultats pourraient être généralisés à des machines de plus grande envergure. Les avantages introduits par une augmentation de la tortuosité s'appliquent à la stratégie consistant à introduire des dispositifs à effet Peltier pour contrôler le flux de chaleur ([41]). Contrairement à une augmentation de A_{HT}, une tortuosité plus élevée du fluide augmente la différence du nombre de Nusselt entre les périodes de (de)magnétisation et d'écoulement. Ainsi, le concepteur pourrait essayer de réduire A_{HT} au profit d'une augmentation de la tortuosité pour fonctionner à des fréquences encore plus élevées. De plus, les cas de tortuosité plus élevées semblent avoir des pertes de conduction plus faibles et favoriser des porosités plus élevées. Cela pourrait même ouvrir la porte pour réduire la masse de l'aimant permanent, car les bandes de HTF parallèles au balayage de l'aimant n'ont pas besoin d'être magnétisées.
Le fonctionnement continu d'un appareil rotatoire donne un champ magnétique qui ressemble à une sinusoïde en mouvement. Cela éloigne le cycle de celui de Brayton, en raison du transfert de chaleur vers le HTF qui se produit entre les (de)magnétisations. L'utilisation d'un moteur pas à pas pour impulser l'aimant peut entraîner une forte augmentation du travail en raison du freinage et de l'accélération de la charge d'inertie. Cependant, le cycle peut être modifié en ajustant les périodes d'écoulement (voir [6]).

Parallèlement à un effort visant à augmenter le transfert de chaleur dans le régénérateur, au lieu d'augmenter A_{HT}, un ensemble de simulations 1D a été réalisé avec un HTF de conductivité thermique accrue. Les détails de la publication peuvent être trouvés

dans l'Annexe A. Le HTF était un mélange de nanofluides Al_2O_3 à base d'eau. Une concentration plus élevée de nanoparticules a augmenté la viscosité et la conductivité thermique du HTF. Cela a entraîné des cycles AMR de performance réduite (Q_{cool} et COP inférieurs), en raison de l'augmentation des pertes de conduction de fluide.

Dans l'ensemble, il existe encore de nombreux aspects du cycle AMR où ce solveur 3D pourrait être utile, par exemple, la détermination du travail magnétique, et la prédiction du COP. En outre, le terme source de l'équation de l'énergie pourrait être modifié pour adopter d'autres types de changements de phase, d'autres technologies de réfrigération alternatives (par exemple, des matériaux électrocaloriques, élastocaloriques ou barocaloriques). La mise en œuvre d'un système exploitant un changement de phase alternatif comprendrait d'abord une caractérisation de l'équation d'état de ces réfrigérants alternatifs, et deuxièmement, la résolution des nouveaux champs physiques qui déterminent le changement de phase alternatif.

CHAPTER 6

ENGLISH CONCLUSION

A thorough numerical study of AMR cycles has been presented. Most importantly, the validity of the solution produced by the numerical solvers has been carefully tested against analytic and experimental data. Starting form the 1D model (chapter 2), the MCE of Gd was the first aspect of the numerical code to be validated. The magnetization links the magnetic and temperature fields, so it becomes the equation of state of MCMs. For the commodity of the programmer, a fitted expression for the magnetization of Gd can be found in appendix B. The final AMR cycle validation of the numerical codes presented in this thesis was done against two different plate prototypes ([97] and [6]). This proved to be the least risky strategy due to the simplicity of the geometry and the already available data (Nusselt number, friction factor, and demagnetization). The inclusion of a magnetic model in the 1D code proved to be key to obtain close results to the experimental data. This means that the difference between the applied and internal magnetic field is not negligible. On top of that, with the help of this 1D numerical code it was demonstrated that by inserting insulator layers, conduction losses in the MCM domain could be reduced.

Next step in the project was to develop a numerical solver that would produce a truly reliable solution. The development of an accurate 3D AMR cycle solver required a dedicated chapter (3). This chapter approached the validation of the 3D AMR cycle solver by tackling first the validation of its most fundamental physical phenomena: flow, magnetic, and thermal fields. Once these fundamental pieces were proven to be computed accurately, the operation of a plate prototype was successfully reproduced. The success of this approach lays in the direct numerical computation of the fundamental phenomena. Indeed, 1D solvers include models for the heat transfer between phases (Nusselt number), for the demagnetization of the MCM (demagentization factor), for the magnetization of the MCM (MFT), and even for the fluid flow (plug flow). Thus it becomes impossible to judge if the solution of the solver is accurate because the models represent faithfully the phenomena, or because the compounded error of the models gives a particularly close solution for the tested cases. The validation of the 3D AMR cycle solver represents the accomplishment of one of the main objectives of this thesis, as now it is possible to simulate the AMR cycle of arbitrary geometries. Additionally the strength of the possibly coupled phenomena was

tested. It was concluded that the fluid flow and thermal field, and magnetic and thermal fields can be decoupled without losing significant accuracy.

Finally the 3D AMR cycle solver was exploited in a series of numerical experiments to determine what is a favorable geometry for regenerators made of pins. In order to understand why one configuration might outperform another one, a previous analysis of the presented geometries was undergone for each of the intervening phenomena. The tested pins kept a similar demagnetization when their form factor was kept constant ($H/\sqrt{A_{cross}}$), regardless of their outline. Also, the approximation found in the literature for the demagnetization of particle clusters was found to be appropriate for higher porosities ($\varepsilon > 0.5$). The introduction of an increased tortuosity of the fluid flow increased the pressure head of the regenerators and their average heat transfer rate, due to an increase of the local fluid velocity (specially for the higher φ cases). However, the main benefit of staggering the pins to increase the fluid tortuosity came from the decreased conduction losses. The geometry needed to achieve a high tortuosity, alternates solid and fluid domains along the temperature span of the machine. This highly reduces the temperature gradients within the solid domain, which has a remarkably higher thermal conductivity. All in all, this could constitute an alternative strategy to increase the cooling power of AMRs. So far, the attention has been set on reducing the particle diameter of packed beds, to increase the heat transfer surface of the MCM for a faster heat transfer. A fast heat transfer between phases enables the machine to operate at higher frequencies, and thus provides an increased cooling power. However, the lower ε associated to smaller particles increases the conduction losses. The proposed alternative strategy is to increase the tortuosity of the regenerators to: lower the conduction losses, and (contrary to increasing A_{HT}) increase the heat transfer rate between the magnetization and surge periods. The latter might be key to the observed increased performance of the higher porosity and tortuosity cases. Instead of increasing the heat transfer for both magnetization and surge periods (due to an increase of A_{HT}), the Nusselt number can be made a switch that lets most of the heat transfer occur in the surge periods. This becomes key to produce a Brayton-like cycle that can operate at higher frequencies.

A crucial step of the numerical validation was the Grid Sensitivity Analysis (GSA). By using the Finite Volume Method (see [100]), the differential terms of the physical laws that govern the most fundamental behaviour of the AMR cycle can be linearized. However, the linearization of those Partial Differential Equations (PDEs) comes with an accuracy cost. On top of the truncation error (associated with truncating the Taylor series), the discretization error poses a challenge to the computation of AMR cycles. Indeed, the

presented calculations are costly computationally speaking (see section 3.2.5), so the user always tends to employ the minimum mesh size for a faster resolution of the linearized matrices. However, the discretization error is practically unknown until the user has demonstrated that the solution converges when reducing the discretization size. The GSA has not been a widely employed (or at least reported) technique among the published numerical experiments of AMR cycles. Reporting the necessary mesh size can give the next user an idea of the computational cost that they will eventually confront, and increases the confidence of the reader in the reported results.

Future perspectives

The presented 3D AMR solver can be conceptualized as a tool to investigate the copious design possibilities of magnetic refrigerators. The MCM employed in this study was Gd, because its characterization was previously published in the literature, and most of the prototypes have employed this MCM. However, a richer library of MCM properties would benefit the research of multimaterial AMRs. These are believed to be key to generate the cooling power demanded by commercial refrigerator machines. Indeed, T_C denotes a starting temperature for the maximum change in magnetic entropy ($\Delta s_{magnetic}$) due to a sudden adiabatic magnetization. This means the phase transition falls into a limited temperature range. MCMs are classified according to the steepness of the magnetization at the temperature of transition into 1st order and 2nd order materials (see Figure 6.1).

Thus, if the temperature span of the regenerator is predefined, the designer can assign different stages of MCM with a T_C that maximizes the magnetic work.

The presented code demands a relatively high amount of computational resources (see sections 3.2.5). Thus the application is restricted to relatively small computational domains (in comparison with the size of most AMR prototypes). This restriction comes from the

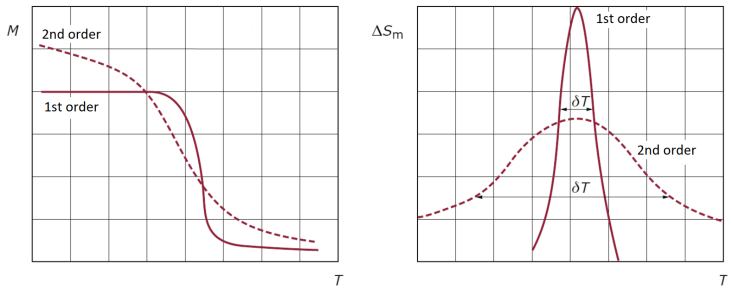

Figure 6.1 Difference between 1st and 2nd order MCMs. Modified schema after [79].

generally small characteristic length of porous media, which comes from the designer's willingness to increase A_{HT} for a fast heat transfer. As it has been commented in the last section, it might be more beneficial to increase the tortuosity of the fluid flow, and Thus not require such large A_{HT}. This could collaterally lower the memory required to represent the geometry of AMRs. Nonetheless, as it has been done in chapter 4, numerical experiments can be performed at a smaller scale, and then generalize the results to machines of greater scale.
The benefits introduced by an increased tortuosity approach the conceptual strategy of introducing Peltier devices to control the heat flow ([41]). Unlike an increased A_{HT}, a higher tortuosity of the fluid flow increases the difference of the Nusselt number between (de)magnetization and surge periods. So, the designer could try to lower A_{HT} in favor of increasing tortuosity to operate at even higher frequencies. Furthermore, higher tortuosity cases seem to have lower conduction losses and favor higher porosities. This might even open the door to reduce the mass of the permanent magnet since the stripes of HTF that are parallel to the swiping motion of the magnet do not need to be magnetized.
The continuous operation of a rotatory device gives a magnetic field that looks like a traveling sinusoid. This distances the cycle from being Brayton-like, due to the heat transfer towards the HTF that happens between (de)magnetizations. Using a stepper motor to drive the magnet might result in a steep increase of the input work due to the braking an acceleration of the inertial load. However, the cycle can by modified by adjusting the surge periods, just as [6] experimented.

In a parallel effort to increase the heat transfer within the regenerator, instead of increasing A_{HT}, a set of 1D simulations were performed with an HTF of increased thermal conductivity. The details of the publication can be found in Appendix A. The HTF was a mixture of water based Al_2O_3 nanofluids. A higher concentration of nanoparticles increased the viscosity and thermal conductivity of the HTF. This resulted in AMR cycles of reduced performance (lower Q_{cool} and COP), due to the increase of the fluid conduction losses.

All in all, there are still many aspects of the AMR cycle where this 3D solver could be useful, e.g. determination of the magnetic work, and prediction of COP. Furthermore, the source term in the energy equation could be modified to adopt other types of solid state phase changes of other alternative refrigeration technologies (e.g. electrocaloric, elastocaloric or barocaloric materials). The implementation for a system that exploits an alternative phase change would include first, a characterization of the equation of state of those alternative refrigerants, and secondly the resolution of the new physical fields that dirve the alternative phase change.

APPENDIX A

Exergy Analysis of a Parallel-Plate Active Magnetic Regenerator with Nanofluids

A.1 Avant-propos

Auteurs et affiliations:

1. Ibai Mugica: étudiant au doctorat*
2. Steven Roy: étudiant en maîtrise*
3. Sébastien Poncet: professeur*
4. Jonathan Bouchard: chercheur**
5. Hakim Nesreddine: chercheur**

*Université de Sherbrooke, Faculté de génie, Département de génie mécanique.
**Laboratoire des Technologies de l'Énergie, Hydro-Québec, Shawinigan.

Date d'acceptation: 31 Août 2017

État de l'acceptation: version finale publiée

Revue: Entropy

Titre français: Analyse Exergétique d'un Régénérateur Magnétique Actif à plaques parallèles avec Nanofluides

Contribution au document: Cet article contribue à l'ensemble de la thèse en montrant comment une augmentation de la conductivité thermique du HTF réduit les performances de l'AMR en augmentant les pertes par conduction dans le fluide.

Résumé français: Cet article analyse les performances énergétiques et exergétiques d'un réfrigérateur à régénération magnétique actif utilisant des nanofluides eau / Al_2O_3 comme fluides caloporteurs. Un modèle numérique 1D a été largement utilisé pour quantifier les performances exergétiques d'un système composé d'un régénérateur à plaques parallèles, d'une source magnétique, d'une pompe, d'échangeurs de chaleur et de vannes de régulation. Les nanofluides à base d'eau / Al_2O_3 sont testés à l'aide de la bibliothèque CoolProp, en tenant compte des propriétés dépendant de la température et de corrélations appropriées. Les résultats sont discutés en termes de coefficient de performance, d'efficacité exergétique et de puissance de refroidissement en fonction de la fraction volumique de nanoparticules et du temps de pompage pour une configuration géométrique donnée. Il est démontré que, même si le transfert de chaleur entre le fluide et le solide est amélioré, il s'accompagne de gradients de température plus faibles dans le fluide et de pertes de charge plus importantes lors de l'augmentation de la concentration en nanoparticules. Cela conduit dans toutes les configurations à des performances inférieures à celles avec de l'eau liquide pure.

A.2 Exergy Analysis of a Parallel-Plate Active Magnetic Regenerator with Nanofluids

This paper analyzes the energetic and exergy performance of an active magnetic regenerative refrigerator using water-based Al_2O_3 nanofluids as heat transfer fluids. A 1D numerical model has been extensively used to quantify the exergy performance of a system composed of a parallel-plate regenerator, magnetic source, pump, heat exchangers and control valves. Al_2O_3-water based nanofluids are tested thanks to CoolProp library, accounting for temperature-dependent properties, and appropriate correlations. The results are discussed in terms of the coefficient of performance, the exergy efficiency, and the cooling power as a function of the nanoparticle volume fraction and blowing time for a given geometrical configuration. It is shown that while the heat transfer between the fluid and solid is enhanced, it is accompanied by smaller temperature gradients within the fluid and larger pressure drops when increasing the nanoparticle concentration. It leads in all configurations to lower performance compared to the base case with pure liquid water.

A.2.1 Introduction

Refrigeration and air conditioning demand has continuously grown during the last decades. Environmental requirements and current ecological standards limit conventional technologies, such as vapor compression cycles. Research on future technologies of refrigeration turned to other principles. Around room temperature, magnetic refrigeration suggests many industrial applications: domestic or industrial cold production for food storage or air conditioning of buildings as few examples. It offers economic, ecological and environmental benefits and a high potential to develop higher efficiencies and lower noise production than current refrigeration systems. The operating principle is based on the magnetocaloric effect (MCE), which is related to a change of entropy in the magnetocaloric material (MCM) due to a variation of the applied magnetic field. This generates a quasi-instantaneous temperature change, typically about $2K \cdot T^{-1}$ for gadolinium at room temperature [14]. A heat transfer fluid, typically water, is then used as a heat transfer medium to remove heat. This process (Brayton cycle) produces cold and reaches steady-state conditions after a number of repeated cycles.

Researches in magnetic refrigeration focus mainly on three specific axes: magnetocaloric materials, magnets, and regenerators. The reader can refer to [41] for a complete review about magnetic refrigeration and to [68] for some recent perspectives. Recently, Trevizoli et al. [90] reviewed different design of Active Magnetic Regenerator (AMR) and proposed an extended optimization methodology based on the minimization of the generated entropy.

One of the main remaining concerns in magnetic refrigeration remains indeed to find the best architecture for the regenerator, which can be composed or parallel-plates, packed-bed media or wires [107]. For this purpose, constant researches have been conducted over the last decades to develop efficient AMR systems. Tusek et al. [97] compared experimentally six AMRs with gadolinium, namely three parallel-plate AMRs and three packed-bed AMRs. Their results showed that the parallel-plate AMR with the smallest porosity and a magnetic field parallel to the plates offers the best overall performance

in terms of temperature span, cooling capacity and COP (Coefficient of Performance). Trevizoli et al. [92] compared three different regenerator geometries (parallel-plate, pin array and packed bed of spheres) having the same porosity and interstitial area. Thus, they could quantify the thermal, viscous and magnetic losses individually. The pin array offered the highest COP and second-law efficiency, while the parallel-plate AMR exhibited the lower performance.

Numerical 1D or 2D models appeared also as valuable tools to design new active magnetic regenerative refrigeration (AMRR) systems ([85],[94],[62],[91],[65],[82],[56],[45]). Tagliafico et al. [85] considered a reciprocating AMR with powder of gadolinium and investigated the influences of both the utilization factor UF (within the range [0.5, 3.5]) and the cycle frequency (within the range [0.1, 0.6]Hz). They showed that, for the optimal value of UF that maximizes the cooling power, the cycle frequency has only a weak influence on the COP of the system contrary to the effect the ambient temperature has on the system. Tura et al. [94] included the demagnetization effect in their 2D model, for which the velocity of water varies with the distance to the plates. They obtained a good agreement between their 2D model and experimental data, and showed that very thin plates and channels are required to get performances comparable to those of a packed-bed regenerator. Wu et al. [106] developed a 2D porous model to investigate the influence of the heat transfer fluid on the performance of the AMRR. For example, mercury offers a 600% enhancement of the cooling capacity. A detailed review about the numerical strategies to model magnetic regenerators up to 2011 may be found in [62].

Recently, Trevizoli et al. [91] quantified the internal (axial conduction, demagnetization, viscous losses) and external (heat transfer through the casing, dead volume, non-uniform applied magnetic field) losses in an AMR device using a 1D model. Losses to the surroundings and dead volumes are shown to have the largest impact on the AMR performance. The 1D model proposed by Niknia et al. [65] has been validated against experimental data for a packed bed regenerator with gadolinium spheres. These authors showed that the step change model for the applied magnetic field is a valid assumption for 1D models and that accounting for loss mechanisms like external heat leaks and demagnetization effects is necessary in the simulations not to overestimate the performance of the machine. Numerically, they introduced a sinusoidal meshing technique, which enables to save about 70% of computational time compared to uniform meshes. Roy et al. [82] compared several heat transfer fluid mixtures with temperature and pressure dependent properties using the same 1D numerical model as the one presented in Section 2. Pure liquid water clearly appeared to offer the best performance compared to mixtures with ethanol, ethylene-glycol, glycerol, ammonia or sodium chloride. They also investigated the effects of the mass flow rate along with the thicknesses of the plates and fluid channels on the COP, exergy efficiency and cooling load. The optimum configuration regarding the prescribed constraints requires a very low mass flow rate as well as low values of the fluid and plate thicknesses to increase the exchange surfaces. This way, conduction losses in the solid are also reduced because of a lower cross section of MCM. Finally, these last authors used a genetic algorithm to propose an optimized active regenerator. Mugica et al. [56] improved the previous 1D code to model a parallel-plate regenerator with insulator layers. Results showed higher temperature spans at zero cooling power, higher cooling load and

COP with the same amount of MCM and applied magnetic field. The authors suggested to find a compromise between reducing the entropy generation by heat conduction, and increasing the magnetocaloric work when introducing insulator layers. Lei et al. [45] published a parametric study about the influence of the cycle frequency, hydraulic diameter and mass flow rate on the COP and generated entropy of an AMR for five geometrical configurations using a 1D model. They recommended the use of the packed screen bed or of a similar matrix structure.

The objectives of the present paper are in three folds: (1) to test the potentiality of enhancing the heat transfer between the magnetocaloric material and the heat transfer fluid by the means of nanofluids; (2) to better understand the influence of each transfer mechanism on the performance of the system; (3) to perform a parametric study and qualify the influences of the nanoparticle volume fraction and the blowing time (through UF) on the COP, exergy efficiency and cooling power. To the best of the author's knowledge, these three objectives have not been considered yet in the literature.

In this article, the description of the thermodynamical model is first presented in Section 2. The assumptions are stated and the main parameters are introduced. The results are discussed in Section 3. Emphasis is made on the influence of the nanoparticle volume fraction and blowing time on the COP, exergy efficiency and cooling power of the system. Finally, conclusions are drawn in Section 4 about the relevance of using nanofluids in magnetic refrigeration to enhance the thermal exchanges between the magnetocaloric material and the heat transfer fluid.

A.2.2 One-Dimensional Numerical Method

Description of the System

The considered model is schematically depicted in Figure A.1. This device is made from two heat exchangers at each end, a source of magnetic field that can be removed with the help of an actuator, a pump that drives the heat transfer fluid and a regenerator which consists of parallel-plates composed of a magnetocaloric material (gadolinium). The valves allow the fluid inside the heat exchangers to flow only when the temperature gradient is sufficient. When steady state is reached, heat is absorbed at the cold end (CS) and rejected at the hot source (HS). This configuration is similar to the experimental reciprocating prototype constructed by Roudaut [79]

This system can be emulated into four steps following the Brayton cycle [41]. First, the magnetization occurs when the magnetic field is on. Due to the MCE, the temperature of the MCM rises. Second, the refrigerant flows from the cold to the hot reservoir, absorbing heat while passing through the regenerator. During this process which is referred as a cold blow, the temperature of the hot reservoir increases. When it reaches a specific limit (THHEX), the valve opens to keep the temperature constant. Third, the magnetic field is removed and the magnetic entropy increases. As a result of the demagnetization, the temperature of the MCM goes down below its original value. For the last step, the refrigerant is pumped from the hot to the cold end, referred as a hot blow. It follows that the temperature in the cold reservoir decreases. In a similar way to the cold blow,

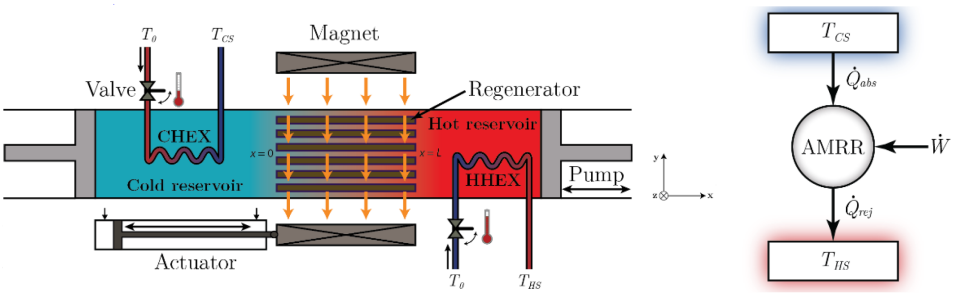

Figure A.1 Simplified scheme of the active magnetic regenerative refrigeration (AMRR) and its power balance.

the valve now opens if the temperature drops below TCHEX. Hence, heat is absorbed to maintain the same temperature level.

Numerical Modeling

Assumptions

1. The system operating near room temperature, adiabatic conditions may be assumed. It has been carefully checked that including losses to the surroundings leads to similar results.
2. The plates are made of gadolinium (Gd), which is the most common material used in magnetic refrigeration near room temperature. To model the magnetocaloric effect (MCE), the experimental data of Dankov et al. [23] are used showing better results compared to the Weiss-Debye-Sommerfeld model. The properties of Gd are temperature- and pressure-dependent thanks to Coolprop library
3. The magnetic field is applied in the y-direction (Figure A.1). As a first step, the demagnetization is neglected. The reader can refer to the works of Nielsen et al. [61], Engelbrecht et al. [27] and Mugica et al. [56] for details on the impact of the demagnetization effect on the performance of the AMR.
4. The magnetic field is assumed equally applied throughout the entire length of the regenerator. The parasitic losses are neglected. Their influence on the AMR performance has been discussed in [27].
5. The time for magnetization or demagnetization is fixed to $t_{mag} = t_{demag} = 0.01s$ and no idle time between each step of the cycle is considered.
6. The flow is supposed to be laminar, fully-developed and steady-state with only one uniform velocity component V in the streamwise direction. The impact of flow maldistribution discussed in [27] is not taken into account here.
7. Nanofluids are assumed to be single-phase fluids with constant volumetric concentration in nanoparticles f throughout the domain. Their thermophysical properties depend on the fluid and nanoparticle properties, f and the local temperature T.

Energy Equations

The equations that govern the temperature distributions in the fluid and solid parts during blows are obtained from the energy conservation law applied to a differential control volume inside the regenerator [41]:

$$\frac{\partial T_f}{\partial t} = -V\frac{\partial T_f}{\partial x} + \frac{h}{\rho_f c_{p,f} e_f}(T_s - T_f)\frac{1}{\rho_f c_{p,f}}\frac{\partial}{\partial x}\left(\lambda_f \frac{\partial T_f}{\partial x}\right) \tag{A.1}$$

$$\frac{\partial T_s}{\partial t} = \frac{h}{\rho_s c_s e_s}(T_f - T_s)\frac{1}{\rho_s c_s}\frac{\partial}{\partial x}\left(\lambda_s \frac{\partial T_s}{\partial x}\right) \tag{A.2}$$

where the indexes f and s refer to the (nano) fluid and the solid (gadolinium) respectively. V is the mean axial fluid velocity (in the x direction) and t is time. ρ, c_p (or c) and λ represent the density ($kg{\cdot}m^{-3}$), the heat capacity ($J{\cdot}kg^{-1}{\cdot}K^{-1}$) and thermal conductivity ($W \cdot m^{-1} \cdot K^{-1}$) of the materials respectively. Note that the solid is subjected to an instantaneous increase in temperature due to magnetization since the magnetic work term is neglected in Equation A.2. The heat capacity of the solid depends also on the applied magnetic field.

The convective heat transfer coefficient h ($W \cdot m^{-2} \cdot K^{-1}$) is evaluated through: $h = NuD_h/\lambda_f$, where D_h is the hydraulic diameter defined by $D_h = 4e_f l/(2e_f + l)$, for a parallel-plate regenerator. As the flow between two plates is symmetric, e_f is half the fluid thickness only and l represents the width of one plate. The heat transfer coefficient h is evaluated using the Nusselt number for constant laminar flow in rectangular ducts (see in [78]):

$$Nu = 8.235\left(1 - 2.0421\alpha + 3.0853\alpha^2 - 2.4765\alpha^3 + 1.0578\alpha^4 - 0.1861\alpha^5\right) \tag{A.3}$$

where $\alpha = 3.95 \times 10^{-3}$ is the aspect ratio of the duct leading to $Nu = 8.2831$. The maximum value of the Reynolds number is obtained here for pure liquid flow: $Re = \rho_f V D_h/\mu_f$ 40 confirming the laminar nature of the flow. During the magnetization and demagnetization phases, $Nu = 4$ as suggested in [79]. The pressure drop for laminar fully developed flows between infinite parallel plates or in a rectangular duct of high aspect ratio is evaluated through the Darcy-Weisbach Equation (see in [30]):

$$\frac{\Delta p}{L} = f\frac{\rho_f V^2}{2D_h} \quad with \quad f = \frac{96}{Re} \tag{A.4}$$

where p represents the pressure, f the friction factor and L the length of the regenerator.

Heat Transfer Fluid Properties

Water-based Al_2O_3 nanofluids are used in Section 3. The main advantages of alumina nanoparticles are their very low price and the absence of corrosion in thermal systems. Their properties are evaluated using the common relations for the density r and heat capacity Cp [10] as follows:

$$\rho_f = \phi\rho_{np} + (1-\phi)\rho_{bf}\rho_f C_{p,f} = \phi(\rho C_p)_{np} + (1-\phi)(\rho C_p)_{bf} \tag{A.5}$$

where the index np refers to the nanoparticles, bf to the base fluid and f to the nanofluid. For Al_2O_3-water-based nanofluids with a mean particle diameter of 47nm, Equations A.6 and A.7 provided by Maïga et al. [51] then used by Mintsa et al. [53] have proven to be accurate in most configurations as shown by Sekrani et al. [83] for laminar flows in an uniformly heated pipe. Equations for the dynamic viscosity μ and the thermal conductivity λ of the nanofluid write:

$$\frac{\mu_f}{\mu_{bf}} = 1 + 7.3\phi + 123\phi^2 = 1 + C_{\mu\phi} \tag{A.6}$$

$$\frac{\lambda_f}{\lambda_{bf}} = \frac{\lambda_{np} + 2\lambda_{bf} - 2\phi(\lambda_{bf} - \lambda_{np})}{\lambda_{np} + 2\lambda_{bf} + \phi(\lambda_{bf} - \lambda_{np})} = 1 + C_{\lambda\phi} \tag{A.7}$$

The base fluid properties are temperature- and pressure-dependent thanks to Coolprop library. The properties of alumina at 20°C are fixed to: $\rho_{np} = 3900kg \cdot m^{-3}$, $C_{p,np} = 775J \cdot kg^{-1} \cdot K^{-1}$ and$\lambda np = 40W \cdot m^{-1} \cdot K^{-1}$.

The ratio C_μ/C_λ was introduced as a kind of merit function by Prasher et al. [72] to recommend or not a given nanofluid. In the present case, this ratio, which slightly varies both with temperature and nanoparticle concentration, remains close to $3.537 \pm 0.1\%$. It means that the increase in viscosity is always larger than the increase in thermal conductivity when the nanoparticle concentration increases but as C_μ/C_λ remains lower than 4, it can be recommended as a heat transfer fluid after [72].

Numerical Method and Parameters

Equations A.1 and A.2 are solved simultaneously using 2nd order finite-difference explicit schemes. The regenerator is discretized into 50 nodes and the maximum CFL is fixed to 0.30. This proved to be a good compromise between computational effort and accuracy. Steady-state is reached when the maximum discrepancy on work for two consecutive cycles is less than 0.005 J.

The boundary conditions for the fluid and solid domains are fully given in Roy et al. [82]. For hot and cold blows, adiabatic conditions are imposed for the fluid at the end of the regenerator assuming that the volume of each reservoir is large compared to the one of the regenerator. The temperatures of the reservoirs are calculated considering a perfect mixing and the displacement of the entire fluid contained within. Adiabatic conditions are imposed at each end of the solid. It is assumed that the heat exchangers absorb or reject all possible heat in order to keep a uniform temperature.

The present model has been validated for the parallel-plate regenerator of Roudaut [79]. It leads to very similar results compared to their experiments with less than 1% error on the hot and cold source temperatures and on the number of cycles to reach a steady-state and about 2% error on the temperature span under steady-state conditions.

Thermodynamic Analysis

The magnetization/demagnetization processes regarding the solid are associated with the heat absorption/rejection for the heat exchangers. In steady state, the work required to drive the AMRR is related to the actuator (magnetic work) and the pump (viscous dissipation). The overall efficiency must take into account several losses, such as the ones from the actuator, Foucault currents and magnetic hysteresis. Those coefficients given from Kitanovski and Egolf [40] are respectively: $\eta_{mot} = 0.90$, $\eta_{Fou} = 0.95$, $\eta_{hys} = 0.97$. The formula to evaluate work power (W) is:

$$\dot{W} = \frac{\dot{W}_{mag}}{\eta_{mot}\eta_{Fou}\eta hys} + \frac{\dot{W}_p}{\eta_p} = \frac{|Q_{rej}| - Q_{abs}}{2(\eta_{mot}\eta_{Fou}\eta hys)t_{mag}} + \frac{F\Delta p}{2\eta_p t_{blow}} \tag{A.8}$$

where the pump efficiency s fixed to $\eta_p = 0.95$, F is the flow rate ($m^3 \cdot s^{-1}$) and t_{blow} the blowing time (s).

The Carnot efficiencies are related to the ambient (T_0) and the source temperatures (T_{HS} andT_{CS}). The exergy (Ex) produced at each end is the product of the Carnot efficiency (θ) with the heat transfer rate ($\dot{Q}$):

$$\dot{E}x_{abs} = \dot{Q}_{abs}\dot{\Theta}_{abs} = \dot{Q}_{abs}\frac{\Delta T_{HX}}{T_{CS}} and \dot{E}x_{rej} = \dot{Q}_{rej}\dot{\Theta}_{rej} = \dot{Q}_{rej}\frac{\Delta T_{HX}}{T_{HS}}, \theta_{abs} = \frac{T_0}{T_{CS}} and \theta_{rej} = \frac{T_0}{T_{HS}} \tag{A.9}$$

with $\Delta T_{HX} = T_{HS} - T_0 = T_0 - T_{CS}$ (Figure A.1). Finally, COP and exergy efficiency η_{ex} are defined as:

$$COP = \frac{\dot{Q}_{abs}}{\dot{W}} \quad and \quad \eta_{ex} = \frac{\dot{E}x_{abs} + |\dot{E}x_{rej}|}{\dot{W}} \tag{A.10}$$

A detailed review on the thermodynamics of active magnetic regenerators has been proposed by Rowe [80],[81].

A.2.3 Results and Discussion

Table A.1 reports the default parameters used for all simulations chosen according to the optimization study of Roy et al. [82]. The applied magnetic field B is fixed to 1.5 T. Ambient conditions are set to $T_0 = 293K$ and $P_0 = 105Pa$. The parameter L and e_s represent the length and half the thickness of one plate, respectively.

Material	**B**	**L**	e_f	e_s	ΔT_{HX}
0.2 kg (Gd)	1.5 T	0.1 m	0.15 mm	0.5 mm	5 K

Table A.1 Fixed parameters used in the simulations.

The results will be discussed also as a function of the utilization factor $UF = \rho_f F cp, f t_{blow}/(\mu_s c_s)$. It is a dimensionless parameter classically used to characterize the conditioning of the system [41], which depends on the volumetric flow rate F and the blowing time t_{blow} among other parameters. The cycle frequency is given by $f = 1/[2(t_{blow} + t_{mag})]$ and will be varied between 0.125 Hz and 0.495 Hz. The fluid and solid properties are averaged values over the temperature range. Rowe [80],[81] introduced also the parameter R defined as: $R = 1 + UF$, which is the ratio of total thermal mass to the solid thermal mass. As it will be shown in the following sections, UF remains relatively small in the present study such that $R \approx 1$.

Influence of the Nanoparticle Concentration

When increasing the thermal conductivity of the heat transfer fluid by adding nanoparticles to liquid water, one expects to increase the heat transfer by convection between the fluid and the plates (positive effect on the performance of the system) but also to increase both the heat transfer by conduction within the fluid and the viscous losses (detrimental effects). The objective is first to qualify the influence of the nanoparticle volume fraction on the overall performance of the system.

The influence of the nanoparticle volume fraction ϕ on the COP, exergy efficiency and cooling power of the AMRR is displayed in Figure A.2 for $t_{blow} = 1s$ ($f = 0.495Hz$) and $F = 10^{-6} m^3 s^{-1}$. Note that, on this figure, UF slightly varies from one nanoparticle concentration to another, from $UF = 0.0473$ at $\phi = 0\%$ to $UF = 0.0467$ at $\phi = 5\%$. The COP and the exergy efficiency decreases quadratically with ϕ, while the absorbed power decreases linearly with the volume fraction in nanoparticles ϕ. For examples, for pure water: $COP = 4.87$, $\eta_{ex} = 16.81\%$ and $\dot{Q}_{abs} = 55.29W$ and for $\phi = 5\%$, $COP = 1.88$, $\eta_{ex} = 6.93\%$ and $\dot{Q}_{abs} = 49.44W$. Introducing nanoparticles increases rapidly the pressure drop and as a consequence, the pumping power $\dot{W}_p$ required to operate the system. It increases then the total work power $\dot{W}$ and then decreases the COP (Equation A.10). At the same time, the presence of nanoparticles leads to an increase of the cold source temperature. Though the weak increase of the mass flow rate, it is accompanied by a global decrease of the absorbed power $\dot{Q}_{abs}$ and so of the exergy efficiency η_{ex} (Equation A.10).

To better understand how the nanofluids affect the efficiency of the system, one needs to look at the heat transfer mechanisms responsible for the entropy generation within the regenerator. The local rate of entropy generation per unit volume is given by [88]:

$$\dot{S}_{gen} = \frac{h\beta(T_s - T_f)^2}{T_s T_f} + \frac{\lambda_f}{T_f^2} + \left(\frac{\partial T_f}{\partial x}\right)^2 + \frac{\lambda_s}{T_s^2}\left(\frac{\partial T_s}{\partial x}\right)^2 + \frac{1}{T_f} u \left|\frac{\partial P}{\partial x}\right| \tag{A.11}$$

where the first term on the right is the entropy generation rate per unit volume due to interphase heat transfer by convection $\dot{S}_{conv}$, the other terms are the entropy generation rates due to conduction within the fluid $\dot{S}_{Fcond}$, due to conduction within the solid $\dot{S}_{Scond}$ and due to the viscous losses $\dot{S}_{viscous}$, respectively. The coefficient β is the surface area

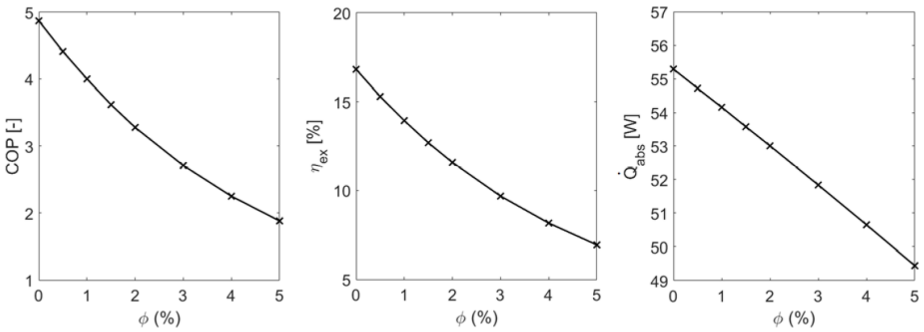

Figure A.2 Influence of the nanoparticle concentration ϕ on the Coefficient of Performance (COP), exergy efficiency and absorbed power $\dot{Q}_{abs}$. Results obtained for UF around 0.047 ($t_{blow} = 1s$ or $f = 0.495Hz$ and $F = 10^{-6}m^3s^{-1}$).

density (m^2/m^3), i.e., the ratio between the heat transfer area and the total volume of the regenerator.

Figure A.3 displays the evolution of the generated entropy as a function of the nanoparticle concentration. The different contributions to Equation A.11 have been integrated both along the regenerator and over a cycle after the system reached a steady-state regime. For $\phi = 0\%$, convection S_{conv} contributes to 87.71% of the total generated entropy S_{gen}. It may be attributed to the particularly high surface area density of the present regenerator. The other contributions come from the viscous losses $S_{viscous}$ (10.12%), the conduction within the MCM S_{Scond} (2.05%) and the conduction within the fluid S_{Fcond} (0.12%).

Figure A.3 confirms the detrimental effect that moderate fractions of Al_2O_3 nanoparticles dispersed in water have on the system. It does not only increase the viscous losses greatly, but the entropy generated by conduction within the fluid domain increases more rapidly than the one associated to convection. In this case, an increase of S_{conv} means a higher heat transfer between the fluid and solid domains. This result was expected as the thermal conductivity of the fluid increased by adding the nanoparticles. This increase is regarded as a positive effect, as S_{conv} can be lowered by shifting to a hybrid Brayton-Ericsson cycle by lowering F and increasing t_{blow} at the same time (see for example the work of Plaznik et al. [71]). Nonetheless, the increase of S_{Fcond} points out that more heat is traveling in the longitudinal direction of the regenerator, destroying to some extent the temperature difference attained in the case with pure water.

Influence of the Blowing time

As already mentioned, the utilization factor UF is a key parameter to describe the heat exchange in magnetic refrigeration as it appears as a prefactor in the advection term when one normalized adequately the fluid energy equation. Nevertheless, the temperature profile will change slightly if F and t_{blow} are modified, even if UF is kept constant. Thus, the objective of the present section is quantify the influence of the blowing time t_{blow} (or cycle frequency f) both at a constant volumetric flow rate (such UF will vary) and at constant UF (such that F is changed accordingly to the blowing time variations). Changing the

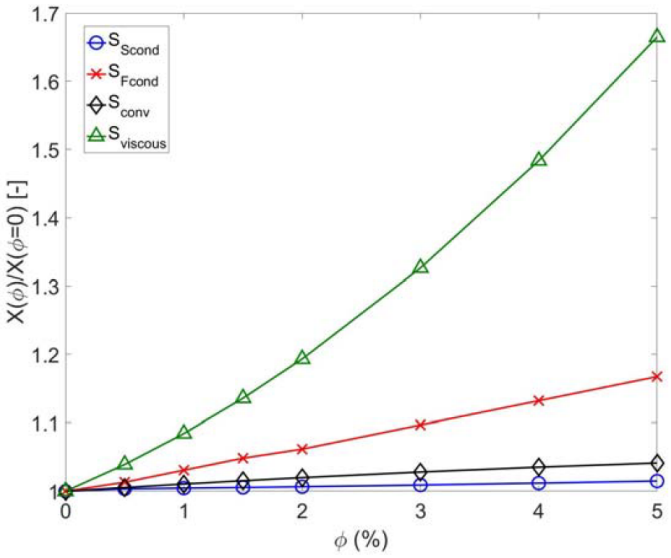

Figure A.3 Evolution of the generated entropy according to the nanoparticle concentration ϕ for utilization factor (UF) around 0.047 ($t_{blow} = 1s$ or $f = 0.495Hz$, $F = 10^{-6}m^3s^{-1}$). The results are normalized by their values for $\phi = 0\%$ ($S_{conv} = 16.95J \cdot m^{-2}K^{-1}$, $S_{Fcond} = 0.023J \cdot m^{-2}K^{-1}$,$S_{Scond} = 0.396J \cdot m^{-2}K^{-1}$, $S_{viscous} = 1.956J \cdot m^{-2}K^{-1}$).

blowing time is expected to enable the nanofluid to catch more or less thermal energy from the MCM.

Figure A.4 a,c,e display the evolution of the COP, exergy efficiency and cooling power as a function of the utilization factor UF for blowing time (resp. frequency) varying between 1s (resp. 0.495 Hz) and 4s (resp. 0.125Hz) and a constant volumetric flow rate $F = 10^{-6}m^3s^{-1}$. The variations of UF directly represent the variations of t_{blow}. The absorbed power increases almost linearly with the blowing time up to a maximum value at $t_{blow} = 3s$, while the COP and the exergy efficiency decrease at the same time. It confirms the results of Rowe [81] at $R \approx 1$, which obtained also a decrease of the efficiency and an increase of the cooling power when UF increases. The main result here is that, for this range of utilization factor ($UF = [0.0467, 0.187]$), introducing nanoparticles into the base fluid leads to lower overall performance of the system, whatever the value of ϕ.

In the present case, increasing UF is associated with a small increase of the pumping work as the pressure drop increases faster than the blowing time. At the same time, the absolute value of the rejected heat increases 1.25 faster than the absorbed heat leading to an increase also of the magnetic power. All in all, the total work power increases 2.5 faster than the absorbed heat, which induces a decrease of the COP. It is accompanied for the same reasons by a decrease of the exergy efficiency η_{ex}. The linear increase of the absorbed power $\dot{Q}_{abs}$ up to $UF \approx 0.14$ ($t_{blow} = 3s$ or $f = 0.166Hz$) is directly connected to a linear decrease of the cold source temperature when UF is increased.

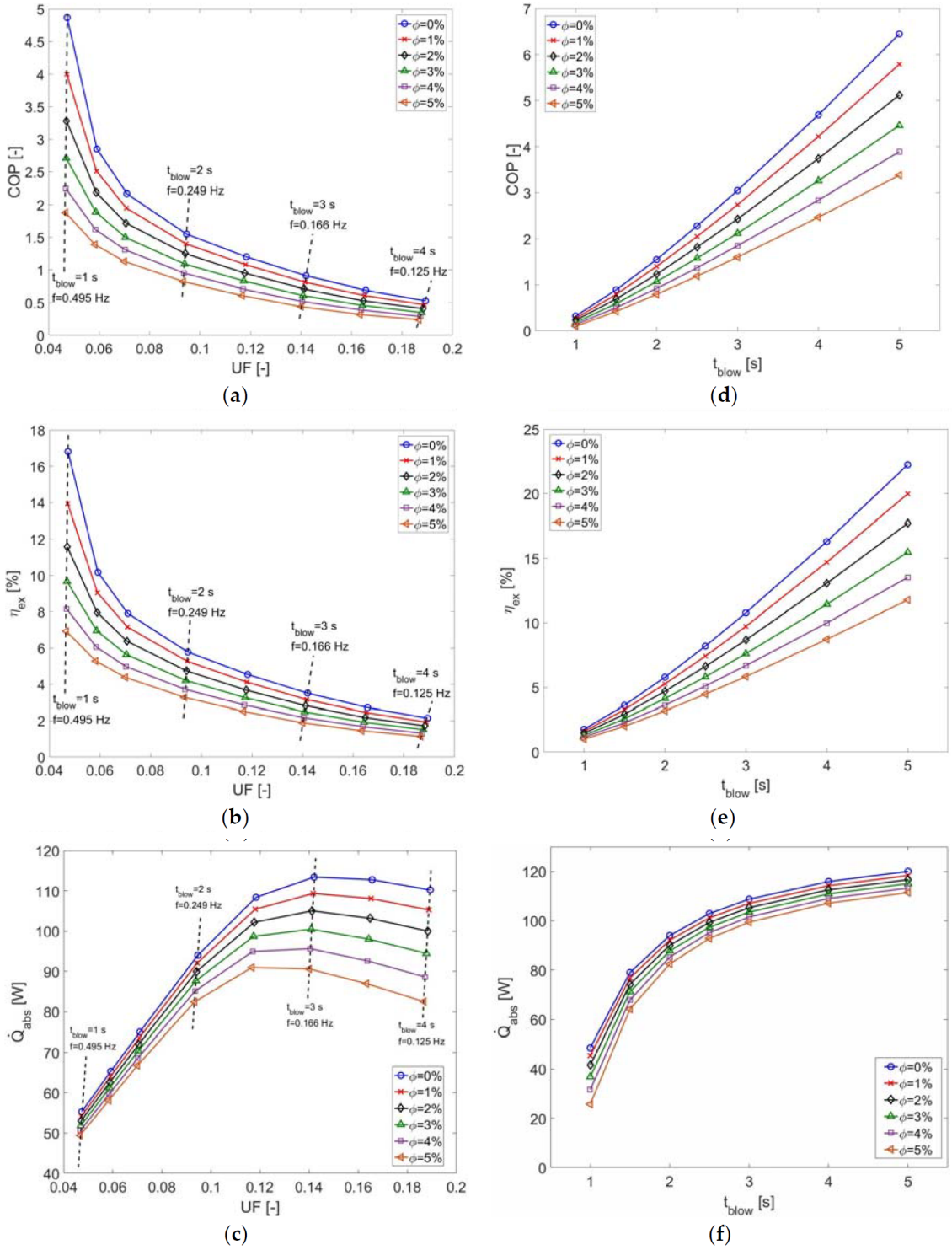

Figure A.4 Variations of the COP, exergy efficiency η_{ex} and absorbed power $\dot{Q}_{abs}$(a, b, c) as a function of the utilization factor UF (at constant flow rate $F = 10^{-6} m^3 s^{-1}$) and (d, e, f) as a function of the blowing time (at constant utilization factor $UF = 0.095$).

The present results confirm the former ones of Rowe [81] at $R = 1$ (small values of UF). For UF varying between 0.1 and 0.5, he also obtained an increase of the cooling power up to a maximum value before a decrease with increasing values of UF. It was attributed to the regenerative temperature change, which starts to limit the net temperature change through the cold heat exchanger. Li et al. [47] applied a simpler model based on the Willmott's model for the blowing processes to the case of a packed-bed regenerator with $300\mu m$ spheres of Gadolinium and pure water as the heat transfer fluid. They showed also that the total work increases with UF. At the same time, the cooling power increases also linearly with UF up to a critical value around $UF = 1$ before decreasing when increasing further UF.

Figure A.4 b,d,f present the variations of the COP, exergy efficiency and absorbed power as a function of the blowing time for a given utilization factor fixed to $UF = 0.095$. To the best of the author's knowledge, no work has been published regarding the influence of the blowing time or cycle frequency at constant utilization factor making comparisons difficult. In the present case, COP, hex and $\dot{Q}_{abs}$ exhibit the same profile and increase when the blowing time is increased. The rejected heat exhibits a non monotonous profile for all cases (not shown here), with a decrease (in magnitude) up to $t_{blow} = 1.5s$ and then it increases up to $t_{blow} = 5s$. Tagliafico et al. [85] obtained a decrease of the COP for increasing values of the cycle frequency for a gadolinium AMR ($m = 395g$, $B = 1.7T$) for an utilization factor that maximizes the refrigeration capacity. However, the amplitude of its decrease was lower for$f = [0.1\tilde{}0.6]Hz$ in their case. The results of Lei et al. [45] confirmed this trend whatever the geometry considered (packed bed spheres, parallel plates or pack screen bed). However, they showed also that COP could also increase with the cycle frequency for large aspect ratios depending on the geometry and hydraulic parameter.

To conclude, the operating parameters have been varied as: $t_{blow} = [1, 5]s$,$f = [0.1, 0.495]Hz$, $F = [0.4, 2.03] \cdot 10^{-6} m^3 s^{-1}$ and $UF = [0.0467, 0.189]$. These ranges do not correspond to any marketable AMR device but have been considered in the literature. The main result obtained here is that whatever the nanoparticle concentrations and the operating conditions, adding alumina nanoparticles to water lead to lower performance in terms of COP, exergy efficiency and cooling power compared to pure water.

A.2.4 Conclusions

This paper is focused on the thermodynamic performance of an active magnetic parallel-plate regenerator composed of gadolinium. An attested 1D numerical model coupled with Coolprop database has been used to qualify the influence of the nanoparticle volume fraction and the blowing time on the thermal performance of the system. Adding nanoparticles to the base fluid leads to a decrease of the COP, exergy efficiency and cooling power of the system whatever the operating conditions considered here. As expected, the increase of the thermal conductivity of the fluid due to the alumina nanoparticles is accompanied by a large increase of the pressure drop. At the same time, the generated entropy by conduction within the fluid increases faster than the one due to convection, which is detrimental to the temperature gradient within the machine. The influence of the blowing time on the thermodynamic performance of the system has also been qualified for variable or con-

stant utilization factor. At fixed flowrate, a blowing time equal to 1s enables to maximize both the COP and exergy efficiency. At the same time, larger blowing times would lead to a higher absorbed power for $t_{blow} = 3s$. At constant utilization factor, COP, exergy efficiency and cooling power are found to increase with the blowing time.

APPENDIX B
Magnetization of Gd

Fitted coefficients of equation (2.4) to the experiments of [44] (Temperature in [K]):

$$M_s(T) = \frac{-0.04583T^2 + 27.08T - 3954}{1 + 0.732^{0.4213(T-291)}} - 0.00245T^2 + 0.438 \tag{B.1}$$

$$a\,(T) = \frac{-1.613}{1 + 0.732^{0.4213(T-291)}} + 0.5643 \tag{B.2}$$

$$b\,(T) = \frac{0.7575}{1 + 0.732^{0.4213(T-291)}} - 0.3996 \tag{B.3}$$

$$c\,(T) = \frac{-0.1173}{1 + 0.732^{0.4213(T-291)}} + 0.06826 \tag{B.4}$$

$$d\,(T) = \frac{0.005889}{1 + 0.732^{0.4213(T-291)}} - 0.003573 \tag{B.5}$$

$$e\,(T) = \frac{0.07188T - 21.99}{1 + 0.732^{0.4213(T-291)}} + 0.03931T - 4.578 \tag{B.6}$$

	Gd	PET	HTF
$c[J \cdot kg^{-1} \cdot K^{-1}]$	See [76]	1425	3628
$\rho[kg \cdot m^{-3}]$	7900	920	1042
$\lambda[W \cdot m^{-1} \cdot K^{-1}]$	10.5	0.3	0.4534

Table B.1 Properties of the materials employed in the numerical model. HTF is a mixture of distilled water (67%) and ethylene-glycol (33%).

LIST OF REFERENCES

[1] A. Aharoni. Demagnetizing factors for rectangular ferromagnetic prisms. *Journal of Applied Physics*, 83(6):3432–3434, 1998.

[2] C. Aprea, G. Cardillo, A. Greco, A. Maiorino, and C. Masselli. A comparison between experimental and 2D numerical results of a packed-bed active magnetic regenerator. *Applied Thermal Engineering*, 90:376 – 383, 2015.

[3] C. Aprea, A. Greco, and A. Maiorino. Modelling an active magnetic refrigeration system: A comparison with different models of incompressible flow through a packed bed. *Applied Thermal Engineering*, 36:296 – 306, 2012.

[4] C. Aprea, A. Greco, and A. Maiorino. Geothermag: A geothermal magnetic refrigerator. *International Journal of Refrigeration*, 59:75 – 83, 2015.

[5] C. Aprea, A. Greco, and A. Maiorino. An application of the artificial neural network to optimise the energy performances of a magnetic refrigerator. *International Journal of Refrigeration*, 82:238 – 251, 2017.

[6] C.R.H. Bahl, T.F. Petersen, N. Pryds, and A. Smith. A versatile magnetic refrigeration test device. *Review of Scientific Instruments*, 79(9):093906, 2008.

[7] G.D. Bahnke and C.P. Howard. The effect of longitudinal heat conduction on periodic-flow heat exchanger performance. *Journal of Engineering for Power*, 86(2):105–117, 1964.

[8] M. Balli, C. Mahmed, P. Bonhote, and O. Sari. On the magnetic forces in magnetic cooling machines: Numerical calculations and experimental investigations. *IEEE Transactions on Magnetics*, 47(10):3383–3386, 2011.

[9] S.M. Benford and G.V. Brown. $T - S$ diagram for gadolinium near the Curie temperature. *Journal of Applied Physics*, 52(3):2110–2112, 1981.

[10] V. Bianco, O. Manca, S. Nardini, and K. Vafai. *Heat Transfer Enhancement with Nanofluids*. CRC Press, New York, USA, 2015.

[11] R. Bjørk and C.R.H. Bahl. Demagnetization factor for a powder of randomly packed spherical particles. *Applied Physics Letters*, 103(10):102403, 2013.

[12] G. Boccardo, F. Augier, Y. Haroun, D. Ferré, and D.L. Marchisio. Validation of a novel open-source work-flow for the simulation of packed-bed reactors. *Chemical Engineering Journal*, 279:809 – 820, 2015.

[13] J. Bouchard, H. Nesreddine, and N. Galanis. Model of a porous regenerator used for magnetic refrigeration at room temperature. *International Journal of Heat and Mass Transfer*, 52(5):1223 – 1229, 2009.

[14] H. Bouchekara. *Recherche sur les Systèmes de Réfrigération Magnétique: Modélisation Numérique, Conception et Optimisation.* Phd thesis, Institut National Polytechnique de Grenoble, 2008.

[15] W.F. Brown. Theory of the approach to magnetic saturation. *Phys. Rev.*, 58:736–743, 1940.

[16] T. Burdyny, D.S. Arnold, and A. Rowe. AMR thermodynamics: Semi-analytic modeling. *Cryogenics*, 62:177 – 184, 2014.

[17] F.C. Canesin, P.V. Trevizoli, J.A. Lozano, and J.R. Barbosa. Modeling of a parallel plate active magnetic gererator using an open source CFD program. In *Fifth IIF-IIR International Conference on Magnetic Refrigeration at Room Temperature (Thermag V)*, Grenoble, France, September 2012., 2012. International Institute of Refrigeration.

[18] D.V. Christensen, K.K. Nielsen, C.R.H. Bahl, and A. Smith. Demagnetizing effects in stacked rectangular prisms. *Journal of Physics D: Applied Physics*, 44(21):215004, 2011.

[19] T.V. Christiaanse, G.A.M. Burton, P. Govindappa, I. Niknia, R. Teyber, P. Trevizoli, and A. Rowe. *Measurement of adiabatic temperature change in a porous regenerator using fibre bragg grating*, volume 2, pages 315–318. Canadian Congress of Applied Mechanics, Victoria, British Columbia, Canada, May 29-June 1, 2017, 2017.

[20] D. Coulomb, J.L. Dupont, and A. Pichard. The role of refrigeration in the global economy. Technical report, International Institute of Refrigeration, 2015.

[21] J.C. Crittenden, R.R. Trussell, D.W. Hand, K.J. Howe, and G. Tchobanoglous. *MWH's Water Treatment: Principles and Design*. Wiley, Hoboken, New Jersey, 2012.

[22] S. Dall'Olio, T. Lei, K. Engelbrecht, and C.R.H. Bahl. The effect of tapering on a magnetocaloric regenerator bed. *International Journal of Refrigeration*, 84:300 – 308, 2017.

[23] S.Y. Dan'kov, A.M. Tishin, V.K. Pecharsky, and K.A. Gschneidner. Magnetic phase transitions and the magnetothermal properties of gadolinium. *Physical Review B*, 57:3478–3490, Feb 1998.

[24] S.K. Das and R.K. Sahoo. Second law analysis of a cyclic regenerator in presence of longitudinal heat conduction in matrix. *Heat and Mass Transfer*, 34(5):395–403, 1999.

[25] A.G. Dixon, M. Nijemeisland, and E.H. Stitt. Systematic mesh development for 3D CFD simulation of fixed beds: Contact points study. *Computers and Chemical Engineering*, 48:135 – 153, 2013.

[26] K. Engelbrecht, K.K. Nielsen, and N. Pryds. An experimental study of passive regenerator geometries. *International Journal of Refrigeration*, 34(8):1817 – 1822, 2011.

[27] K. Engelbrecht, J. Tusek, K.K. Nielsen, A. Kitanovski, C.R.H. Bahl, and A. Poredos. Improved modelling of a parallel plate active magnetic regenerator. *Journal of Physics D: Applied Physics*, 46(25):255002, 2013.

[28] D. Eriksen, K. Engelbrecht, C.R.H. Bahl, R. Bjørk, and K.K. Nielsen. Effects of flow balancing on active magnetic regenerator performance. *Applied Thermal Engineering*, 103:1 – 8, 2016.

[29] D. Eriksen, K. Engelbrecht, C.R.H. Bahl, R. Bjørk, K.K. Nielsen, A.R. Insinga, and N. Pryds. Design and experimental tests of a rotary active magnetic regenerator prototype. *International Journal of Refrigeration*, 58:14 – 21, 2015.

[30] L. Garby and P.S. Larsen. *Bioenergetics: Its Thermodynamic Foundations*. Cambridge University Press, Cambridge, UK, 1991.

[31] D.K. Gartling. A test problem for outflow boundary conditions—flow over a backward-facing step. *International Journal for Numerical Methods in Fluids*, 11(7):953–967, 1990.

[32] M. Giese, K. Rottschäfer, and D. Vortmeyer. Measured and modeled superficial flow profiles in packed beds with liquid flow. *AIChE Journal*, 44(2):484–490, 1998.

[33] W. Goetzler. "Energy savings potential and rd opportunities for non-vapor-compression HVAC technologies". Technical report, U.S. Department of Energy, 2014.

[34] K.A. Gschneidner and V.K. Pecharsky. Thirty years of near room temperature magnetic cooling: Where we are today and future prospects. *International Journal of Refrigeration*, 31(6):945 – 961, 2008.

[35] N. Hirano, S. Nagaya, M. Takahashi, T. Kuriyama, K. Ito, and S. Nomura. Development of magnetic refrigerator for room temperature application. *AIP Conference Proceedings*, 613(1):1027–1034, 2002.

[36] S. Jacobs, J. Auringer, A. Boeder, J. Chell, L. Komorowski, J. Leonard, S. Russek, and C. Zimm. The performance of a large-scale rotary magnetic refrigerator. *International Journal of Refrigeration*, 37:84 – 91, 2014.

[37] M.S. Kamran, J. Sun, Y.B. Tang, Y.G. Chen, J.H. Wu, and H.S. Wang. Numerical investigation of room temperature magnetic refrigerator using microchannel regenerators. *Applied Thermal Engineering*, 102:1126 – 1140, 2016.

[38] G. Karypis and V. Kumar. A fast and high quality multilevel scheme for partitioning irregular graphs. *SIAM Journal on Scientific Computing*, 20(1):359–392, 1998.

[39] A. Kitanovski and P.W. Egolf. Thermodynamics of magnetic refrigeration. *International Journal of Refrigeration*, 29(1):3 – 21, 2006.

[40] A. Kitanovski and P.W. Egolf. Application of magnetic refrigeration and its assessment. *Journal of Magnetism and Magnetic Materials*, 321(7):777 – 781, 2009.

[41] A. Kitanovski, J. Tušek, U. Tomc, U. Plaznik, M. Ozbolt, and A. Poredoš. *Magnetocaloric Energy Conversion*. Springer, Switzerland, 2015.

[42] M. Kondo, K. Ueno, K. Takeuchi, R. Nomura, and T. Kizaki. Effects of magnetocaloric wire on increase in magnetic refrigeration cycle. In *Proceedings of the 7th International Conference on Magnetic Refrigeration at Room Temperature (Thermag VII)*, Turin, Italy, September 11-14, 2016., 2016. International Institute of Refrigeration.

[43] T. Krenke, E. Duman, M. Acet, E. Wassermann, X. Moya, L. Manosa, and A. Planes. Inverse magnetocaloric effect in ferromagnetic $Ni\breve{}Mn\breve{}Sn$ alloys. *Nature Materials*, 4:450–454, 2005.

[44] J.S. Lee. Evaluation of the magnetocaloric effect from magnetization and heat capacity data. *Physica Status Solidi (b)*, 241(7):1765–1768, 2004.

[45] T. Lei, K. Engelbrecht, K.K. Nielsen, and C.T. Veje. Study of geometries of active magnetic regenerators for room temperature magnetocaloric refrigeration. *Applied Thermal Engineering*, 111:1232 – 1243, 2017.

[46] P. Li, M. Gong, and J. Wu. Geometric optimization of an active magnetic regenerative refrigerator via second-law analysis. *Journal of Applied Physics*, 104(10):103536, 2008.

[47] P. Li, M. Gong, G. Yao, and J. Wu. A practical model for analysis of active magnetic regenerative refrigerators for room temperature applications. *International Journal of Refrigeration*, 29(8):1259 – 1266, 2006. Magnetic Refrigeration at Room Temperature.

[48] D. Lide. *CRC Handbook of Chemistry and Physics*. CRC Press, Boca Raton, USA, 1998.

[49] S. Lionte, C. Vasile, and M. Siroux. Numerical analysis of a reciprocating active magnetic regenerator. *Applied Thermal Engineering*, 75:871 – 879, 2015.

[50] J.A. Lozano, M.S. Capovilla, P.V. Trevizoli, K. Engelbrecht, C.R.H. Bahl, and J.R. Barbosa. Development of a novel rotary magnetic refrigerator. *International Journal of Refrigeration*, 68:187 – 197, 2016.

[51] S.E.B Maiga, S.J. Palm, C.T. Nguyen, G. Roy, and N. Galanis. Heat transfer enhancement by using nanofluids in forced convection flows. *International Journal of Heat and Fluid Flow*, 26(4):530 – 546, 2005.

[52] J.M. Martínez-Huerta, J. De La Torre Medina, L. Piraux, and A. Encinas. Configuration dependent demagnetizing field in assemblies of interacting magnetic particles. *Journal of Physics: Condensed Matter*, 25(22):226003, 2013.

[53] H.A. Mintsa, G. Roy, C.T. Nguyen, and D. Doucet. New temperature dependent thermal conductivity data for water-based nanofluids. *International Journal of Thermal Sciences*, 48(2):363 – 371, 2009. Nano Micro Mini Channels and Computational Heat Transfer.

[54] A.H. Morrish. *The Physical Principles of Magnetism*. John Wiley & Sons, Inc., Massachusetts, USA, 2001.

[55] I. Mugica, S. Poncet, and J. Bouchard. Entropy generation in a parallel-plate active magnetic regenerator with insulator layers. *Journal of Applied Physics*, 121(7):074901, 2017.

[56] I. Mugica, S. Poncet, and J. Bouchard. An open source DNS solver for the simulation of active magnetocaloric regenerative cycles. *Applied Thermal Engineering*, 141:600 – 616, 2018.

[57] K. Nam and S. Jeong. Development of parallel wire regenerator for cryocoolers. *Cryogenics*, 46(4):278 – 287, 2006.

[58] K. Nielsen and K. Engelbrecht. The influence of the solid thermal conductivity on active magnetic regenerators. *Journal of Physics D: Applied Physics*, 45(14):145001, 2012.

[59] K.K. Nielsen, C.R.H. Bahl, A. Smith, K. Engelbrecht, U.L. Olsen, and N. Pryds. The influence of non-magnetocaloric properties on the performance in parallel-plate {AMRs}. *International Journal of Refrigeration*, 37:127 – 134, 2014. New Developments in Magnetic Refrigeration.

[60] K.K. Nielsen, C.R.H. Bahl, A. Smith, N. Pryds, and J. Hattel. A comprehensive parameter study of an active magnetic regenerator using a 2D numerical model. *International Journal of Refrigeration*, 33(4):753 – 764, 2010.

[61] K.K. Nielsen, A. Smith, C.R.H. Bahl, and U.L. Olsen. The influence of demagnetizing effects on the performance of active magnetic regenerators. *Journal of Applied Physics*, 112(9):094905, 2012.

[62] K.K. Nielsen, J. Tusek, K. Engelbrecht, S. Schopfer, A. Kitanovski, C.R.H. Bahl, A. Smith, N. Pryds, and A. Poredos. Review on numerical modeling of active magnetic regenerators for room temperature applications. *International Journal of Refrigeration*, 34(3):603 – 616, 2011.

[63] N. Nigro and S. Márquez Damián. Comparison of single phase laminar and large eddy simulation (LES) solvers using the OpenFOAM suite. *Asociación Argentina de Mecánica Computacional*, XXIX:15–18, 2010.

[64] P. Nikkola, C. Mahmed, M. Balli, and O. Sari. 1D model of an active magnetic regenerator. *International Journal of Refrigeration*, 37:43 – 50, 2014.

[65] I. Niknia, O. Campbell, T.V. Christiaanse, P. Govindappa, R. Teyber, P.V. Trevizoli, and A. Rowe. Impacts of configuration losses on active magnetic regenerator device performance. *Applied Thermal Engineering*, 106:601 – 612, 2016.

[66] P.A. Oliveira, P.V. Trevizoli, J.R. Barbosa, and A.T. Prata. A 2D hybrid model of the fluid flow and heat transfer in a reciprocating active magnetic regenerator. *International Journal of Refrigeration*, 35(1):98 – 114, 2012.

[67] L. Otero, A.D. Molina-Garcia, and P.D. Sanz. Some interrelated thermophysical properties of liquid water and ice I. a user-friendly modeling review for food high-pressure processing. *Critical Reviews in Food Science and Nutrition*, 42(4):339–352, 2002.

[68] V.K. Pecharsky, J. Cui, and D.D. Johnson. (magneto)caloric refrigeration: is there light at the end of the tunnel? *Philosophical Transactions of the Royal Society A: Mathematical, Physical and Engineering Sciences*, 374(2074):20150305, 2016.

[69] V.K. Pecharsky and K.A. Gschneidner. Giant magnetocaloric effect in $Gd_5(Si_2Ge_2)$. *Phys. Rev. Lett.*, 78:4494–4497, 1997.

[70] T.F. Petersen, N. Pryds, A. Smith, J. Hattel, H. Schmidt, and H.J. Høgaard Knudsen. Two-dimensional mathematical model of a reciprocating room-temperature active magnetic regenerator. *International Journal of Refrigeration*, 31(3):432 – 443, 2008.

[71] U. Plaznik, J. Tušek, A. Kitanovski, and A. Poredoš. Numerical and experimental analyses of different magnetic thermodynamic cycles with an active magnetic regenerator. *Applied Thermal Engineering*, 59(1–2):52 – 59, 2013.

[72] R. Prasher, D. Song, J. Wang, and P. Phelan. Measurements of nanofluid viscosity and its implications for thermal applications. *Applied Physics Letters*, 89(13):133108, 2006.

[73] R. Prozorov and V.G. Kogan. Effective Demagnetizing Factors of Diamagnetic Samples of Various Shapes. *Physical Review Applied*, 10:014030, 2018.

[74] P. Rajesh Kanna and M. Kumar Das. A short note on the reattachment length for BFS problem. *International Journal for Numerical Methods in Fluids*, 50(6):683–692, 2006.

[75] M. Ramšak. Conjugate heat transfer of backward-facing step flow: A benchmark problem revisited. *International Journal of Heat and Mass Transfer*, 84:791 – 799, 2015.

[76] M. Risser, C. Vasile, B. Keith, T. Engel, and C. Muller. Construction of consistent magnetocaloric materials data for modelling magnetic refrigerators. *International Journal of Refrigeration*, 35(2):459 – 467, 2012.

[77] M. Risser, C. Vasile, C. Muller, and A. Noume. Improvement and application of a numerical model for optimizing the design of magnetic refrigerators. *International Journal of Refrigeration*, 36(3):950 – 957, 2013.

[78] W.M. Rohsenow, J.P. Hartnett, and Y.I. Cho. *Handbook of heat transfer*. McGraw-Hill, New York, USA, 1998.

[79] J. Roudaut. *Modélisation et conception de systèmes de réfrigération magnétique autour de la température ambiante*. Phd thesis, Université de Grenoble, 2011.

[80] A. Rowe. Thermodynamics of active magnetic regenerators: Part I. *Cryogenics*, 52(2):111 – 118, 2012.

[81] A. Rowe. Thermodynamics of active magnetic regenerators: Part II. *Cryogenics*, 52(2):119 – 128, 2012.

[82] S. Roy, S. Poncet, and M. Sorin. Sensitivity analysis and multiobjective optimization of a parallel-plate active magnetic regenerator using a genetic algorithm. *International Journal of Refrigeration*, 75:276 – 285, 2017.

[83] G. Sekrani and S. Poncet. Further investigation on laminar forced convection of nanofluid flows in a uniformly heated pipe using direct numerical simulations. *Applied Sciences*, 6(11), 2016.

[84] J.S. Smart. *Effective field theories of magnetism*. Saunders, Philadelphia, 1966.

[85] G. Tagliafico, F. Scarpa, and F. Canepa. A dynamic 1-D model for a reciprocating active magnetic regenerator; influence of the main working parameters. *International Journal of Refrigeration*, 33(2):286 – 293, 2010.

[86] X. Tan, P. Chai, C.M. Thompson, and M. Shatruk. Magnetocaloric effect in $AlFe_2B_2$: Toward magnetic refrigerants from earth-abundant elements. *Journal of the American Chemical Society*, 135(25):9553–9557, 2013.

[87] R. Teyber, P.V. Trevizoli, T.V. Christiaanse, P. Govindappa, I. Niknia, and A. Rowe. Permanent magnet design for magnetic heat pumps using total cost minimization. *Journal of Magnetism and Magnetic Materials*, 442:87 – 96, 2017.

[88] P.V. Trevizoli and J.R. Barbosa. Entropy generation minimization analysis of oscillating-flow regenerators. *International Journal of Heat and Mass Transfer*, 87:347 – 358, 2015.

[89] P.V. Trevizoli, J.R. Barbosa, A. Tura, D. Arnold, and A. Rowe. Modeling of thermomagnetic phenomena in active magnetocaloric regenerators. *Journal of Thermal Science and Engineering Applications*, 6(3):1948–5085, 2014.

[90] P.V. Trevizoli, T.V. Christiaanse, P. Govindappa, I. Niknia, R. Teyber, J.R. Barbosa Jr., and A. Rowe. Magnetic heat pumps: An overview of design principles and challenges. *Science and Technology for the Built Environment*, 22(5):507–519, 2016.

[91] P.V. Trevizoli, A.T. Nakashima, and J.R. Barbosa. Performance evaluation of an active magnetic regenerator for cooling applications-Part II: Mathematical modeling and thermal losses. *International Journal of Refrigeration*, 72:206 – 217, 2016.

[92] P.V. Trevizoli, A.T. Nakashima, G.F. Peixer, and J.R. Barbosa. Performance assessment of different porous matrix geometries for active magnetic regenerators. *Applied Energy*, 187:847 – 861, 2017.

[93] A. Tura, K. Nielsen, N. Van Nong, N. Pryds, P. Trevizoli, T. Christiaanse, R. Teyber, and A. Rowe. *Experimental performance evaluation of sintered Gd spheres packed beds*, volume 126960, pages 240–243. International Institute of Refrigeration IIF/IIR, Turin, Italy, September 11-14, 2016., 2016.

[94] A. Tura, K.K. Nielsen, and A. Rowe. Experimental and modeling results of a parallel plate-based active magnetic regenerator. *International Journal of Refrigeration*, 35(6):1518 – 1527, 2012.

[95] J. Tušek, A. Kitanovski, and A. Poredoš. Geometrical optimization of packed-bed and parallel-plate active magnetic regenerators. *International Journal of Refrigeration*, 36(5):1456 – 1464, 2013.

[96] J. Tušek, A. Kitanovski, I. Prebil, and A. Poredoš. Dynamic operation of an active magnetic regenerator (AMR): Numerical optimization of a packed-bed AMR. *International Journal of Refrigeration*, 34(6):1507 – 1517, 2011.

[97] J. Tušek, A. Kitanovski, S. Zupan, I. Prebil, and A. Poredoš. A comprehensive experimental analysis of gadolinium active magnetic regenerators. *Applied Thermal Engineering*, 53(1):57 – 66, 2013.

[98] C. Vasile and C. Muller. Innovative design of a magnetocaloric system. *International Journal of Refrigeration*, 29(8):1318 – 1326, 2006.

[99] V. Čingoski and H. Yamashita. Modeling of permanent magnets in three-dimensional space using edge finite elements. *Journal of Applied Physics*, 81(8):4088–4090, 1997.

[100] H. Versteeg and W. Malalasekera. *An Introduction to Computational Fluid Dynamics: The Finite Volume Method*. Pearson Education, Harlow Essex, England, 2007.

[101] A. Šarlah, J. Tušek, and A. Poredoš. Comparison of thermo-hydraulic properties of heat regenerators applicable to active magnetic refrigerators. *Strojniški vestnik - Journal of Mechanical Engineering*, 58(1):16–22, 2012.

[102] D. Vuarnoz and T. Kawanami. Numerical analysis of a reciprocating active magnetic regenerator made of gadolinium wires. *Applied Thermal Engineering*, 37:388 – 395, 2012.

[103] D. Vuarnoz and T. Kawanami. Experimental validation of a coupled magneto-thermal model for a flat-parallel-plate active magnetic regenerator. *Applied Thermal Engineering*, 54(2):433 – 439, 2013.

[104] N. Wakao and S. Kaguei. *Heat and mass transfer in packed beds*. Gordon and Breach Science Publishers, 1983.

[105] P. Weiss and A. Piccard. Le phénomène magnétocalorique. *Journal of Physics*, 7(5):103–109, 1917.

[106] J. Wu, C. Liu, P. Hou, Y. Huang, G. Ouyang, and Y. Chen. (fluid choice and test standardization for magnetic regenerators operating at near room temperature. *International Journal of Refrigeration*, 37:135–146, 2014.

[107] B. Yu, M. Liu, P.W. Egolf, and A. Kitanovski. A review of magnetic refrigerator and heat pump prototypes built before the year 2010. *International Journal of Refrigeration*, 33(6):1029 – 1060, 2010.

[108] C. Zimm, A. Boeder, J. Chell, A. Sternberg, A. Fujita, S. Fujieda, and K. Fukamichi. Design and performance of a permanent-magnet rotary refrigerator. *International Journal of Refrigeration*, 29(8):1302 – 1306, 2006.

[109] C. Zimm, A. Jastrab, A. Sternberg, V.K. Pecharsky, K.A. Gschneider, M. Osborne, and I. Anderson. Description and performance of a near-room temperature magnetic refrigerator. *Advances in Cryogenic Engineering*, 43:1759–1766, 1998.